



Norwegian University of  
Science and Technology

# A Method for Controlled Oxide and Carbon Coating of Silicon Nanoparticles as Anode in Lithium-Ion Batteries

**Marte Orderud Skare**

Nanotechnology

Submission date: June 2017

Supervisor: Ann Mari Svensson, IMA

Co-supervisor: Trygve Mongstad, IFE  
Jan Petter Mæhlen, IFE  
Hanne Flåten Andersen, IFE

Norwegian University of Science and Technology  
Department of Materials Science and Engineering



# **A Method for Controlled Oxide and Carbon Coating of Silicon Nanoparticles as Anode in Lithium-Ion Batteries**

Candidate

Marte Orderud Skare

Supervisor

**Ann Mari Svensson**

NTNU

Co-supervisors

**Trygve Mongstad**

IFE

**Jan Petter Mæhlen**

IFE

**Hanne Flåten Andersen**

IFE



# Preface

---

This master's thesis marks the end of five years at NTNU in Trondheim, where I have studied towards a Master of Science in Nanotechnology and its use in materials, energy and for the environment.

The work has been carried out during the spring of 2017 at the departments for Solar Energy and Energy Systems at Institute for Energy Technology (IFE). It has been a part of the *Siproco Fobeliba* (Silicon Production Control For Better Lithium Ion Batteries) project at IFE, aimed at investigating how silicon nanoparticles can be tailored for use in lithium-ion batteries. The Research Council of Norway is acknowledged for funding of the project through the ENERGIX program. The experimental work began in the fall of 2016 for the author's project report, and some parts of this thesis will therefore be based on the submitted report [1]. All the work has been carried out independently by the author, except for TEM analysis of the coated silicon, which has either been conducted by Patricia Almeida Carvalho from Sintef or Asbjørn Ulvestad from UiO/IFE.

On the front page are two M&Ms that happened to land in my hand one evening this spring, and I found them quite descriptive of my thesis work. When coating single particles, a smooth coating is often seen. Dealing with agglomerated ones however, is another story. Luckily for me, they tasted the same.

Trondheim - June 11, 2017

Marte Orderud Skare



# Acknowledgements

---

First and foremost I would like to send a big thanks to the researchers at the Solar Energy department, for making my last year as a student such an amazing experience. I felt welcome from the start, and the hard working, but ever so social, environment has kept me motivated through long hours. I am thankful for the opportunity to work alongside dedicated researchers who truly believe in the work they do, and the great motto of IFE: "Research for a better future". A motto I will always keep with me.

My closest supervisor Trygve Mongstad has been of immense importance in keeping me (relatively) sane, and his spirit and motivation in all areas of work deserves a medal. Main supervisor Ann Mari Svensson has facilitated lab work when at NTNU, and has been of significant guidance throughout the thesis work. Hanne Flåten Andersen has been of invaluable support and guidance as I have ventured into the battery world, and her expertise both in the lab and when interpreting electrochemical data cannot be thanked enough. Jan Petter Mæhlen has provided illustrations and guidance when needed, and for this I am grateful. The Siproco Fobeliba group has provided a useful arena for feedback and discussions, and has always been supportive and helpful.

A big shout-out to Solveig and Ambjørn for allowing me to live with them these last few weeks for assembling this thesis. You have truly helped me stay motivated, as well as comfortable for focusing on the last stretch.

A special thanks to both my mother, Magnhild Skare and my other half, Remi André Kjør-laug for taking the time to proofread my entire thesis. Your feedback, encouragement and improvements are greatly appreciated.

Lastly, but most importantly, I'd like to thank my classmates and friends in Trondheim. I would not stand where I am today if it had not been for the great friendships I have made on the lacrosse field, in the study halls, and at nanokjellern. Keeping me motivated through tough times, and always giving me something to strive for.

Mamsen og papsen: I did it!

M.O.S.

(finally) Master of Science



# Abstract

---

Silicon has emerged as a promising alternative to graphite in lithium-ion batteries. Silicon can, theoretically, provide up to ten times higher capacity due to its high alloying capabilities with lithium. This improvement in initial capacity is however followed by capacity fade during the early cycles, which is undesirable for commercial applications. The low cycle life is in turn due to the high alloying with lithium, as this leads to a large volume expansion and subsequent contraction of the material.

In this work, a method for coating silicon has been investigated to eventually be able to buffer the volume change associated with cycling. Double core-shell particles were fabricated by wet chemical methods, and can serve as a base for creating yolk-shell particles in the future. Silicon nanoparticles from a Free Space Reactor with diameters between 50 nm and 1  $\mu\text{m}$  have successfully been coated with a 50-80 nm thick oxide layer by the use of tetraethyl orthosilicate, designed to be a sacrificial layer to be etched away at a later state. Following the oxide layer, a thin carbon coating has been applied by a resorcinol-formaldehyde resin and pyrolysis, which interconnects the oxide coated particles in a web-like morphology. The coating steps have been thoroughly characterized by electron microscopy, energy dispersive spectroscopy, x-ray diffraction, thermogravimetric analysis, dynamic light scattering and nitrogen adsorption. Problems related to the upscaling of this process were revealed during carbon coating, as it did not give sufficient control and reproducibility with coating thickness and morphology for the chosen starting material.

Li-ion battery half-cells were prepared with the reference silicon and electrochemically cycled, and one half-cell exhibited a superior lifetime (up to 1,000 cycles) when cycled at a reversible capacity of  $\sim 720 \text{ mAh/g}_{\text{Si}}$ , while others could retain  $1,200 \text{ mAh/g}_{\text{Si}}$  for only 150 cycles. The cycling of both amorphous and crystalline silicon was done, but the crystallinity did not seem to have an effect on the performance. Crystalline silicon anodes with a loading of  $\sim 0.4 \text{ mg}_{\text{Si}}/\text{cm}^2$  displayed an irreversible capacity loss (ICL) in the first cycle of 8-9%, and a reversible capacity of  $\sim 1,750 \text{ mAh/g}_{\text{Si}}$  for 120 cycles, while a higher loading of  $\sim 0.5 \text{ mg}_{\text{Si}}/\text{cm}^2$  displayed the same ICL but a capacity of  $\sim 2,500 \text{ mAh/g}_{\text{Si}}$  for only 50 cycles. Amorphous silicon anodes with a loading of  $\sim 0.5 \text{ mg}_{\text{Si}}/\text{cm}^2$  displayed a low ICL of 1%, and a reversible capacity of  $\sim 2,000 \text{ mAh/g}_{\text{Si}}$  for 70 cycles. The lifetimes are clearly more dependent upon loading and cell fabrication, than of initial crystallinity of the material.

---

In sum, this work has provided a starting point for the fabrication of yolk-shell particles by using Si nanoparticles from an FSR. A homogeneous coating of oxide has been applied, and a thin carbon coating was observed for a few samples. Electrochemical results from the cycling of pure silicon showed a high dependence on loading and cell fabrication, and it is therefore imperative to keep the electrode fabrication and cell assembly as similar as possible for comparison purposes.

# Sammendrag

---

Silisium har vist seg å være et lovende alternativ til grafitt i litiumionebatterier. Silisium kan, teoretisk sett, levere opp til ti ganger kapasiteten grunnet høy legeringsevne med litium. Uheldigvis er denne forbedringen i initiell kapasitet raskt etterfulgt av degradering tidlig i syklingen, noe som har forhindret kommersialisering av silisium som anode. Denne degradering er i hovedsak grunnet den høye legeringsevnen, som gjør at silisiumet ekspanderer under litiering, og krymper igjen under delitiering.

I dette arbeidet har en overflatebehandling av silisium blitt utforsket, for å etterhvert kunne bufre volumendringen assosiert med sykling. Dobbel kjerne-skallpartikler er fabrikkert ved hjelp av våtkjemiske metoder, og vil kunne etterhvert utvikles til plomme-skallpartikler ved videre arbeid. Silisiumnanopartikler fra en Fritt Rom Reaktor (Free Space Reactor) med diameter mellom 50 nm og 1  $\mu\text{m}$  har blitt dekket av et 50-80 nm tykt belegg av oksid ved hjelp av tetraetylortosilikat, som vil fungere som et offerlag, og skal ertes bort i videre arbeid. Dette har blitt etterfulgt av et tynt karbonlag fra resorcinol-formaldehyd og pyrolyse, som dekket silisiumaggrerater og dermed resulterte i et sammenhengende, web-liknende nettverk av dobbel-skallpartikler. Stegene i metoden har blitt karakterisert av elektronmikroskopi, energidispersivspektroskopi, røntgendiffraksjon, termogravimetrisk analyse, dynamisk lysspredning og nitrogen adsorbering. Problemer relatert til oppskaleringen av prosessen ble avduket ved deponeringen av karbonbelegget, da det ikke resulterte i en kontrollerbar prosedyre og reproduserbarhet for det valgte startmaterialet.

Litiumionebatterihalvceller ble laget av referansesilisium og elektrokjemisk syklet, og en halvcelle viste overlegen levetid (opp mot 1,000 sykler) ved  $\sim 720 \text{ mAh/g}_{\text{Si}}$ , mens andre halvceller syklet ved  $1,200 \text{ mAh/g}_{\text{Si}}$  kun nådde 150 sykler. Sykling av både amorf og krystallinsk silisium ble gjort, men krystallinitet hadde liten effekt på ytelse. Krystallinske silisiumanoder med en last på  $\sim 0.4 \text{ mg}_{\text{Si}}/\text{cm}^2$  viste et irreversibelt kapasitetstap (ICL) på 8-9%, og en reversibel kapasitet på  $1,750 \text{ mAh/g}_{\text{Si}}$  i 120 sykler, mens en høyere last på  $\sim 0.5 \text{ mg}_{\text{Si}}/\text{cm}^2$  viste samme ICL, men en kapasitet på  $\sim 2,500 \text{ mAh/g}_{\text{Si}}$  i bare 50 sykler. Amorfe silisiumanoder med en last på  $\sim 0.5 \text{ mg}_{\text{Si}}/\text{cm}^2$  viste en lav ICL på 1% og reversibel kapasitet på  $\sim 2,000 \text{ mAh/g}_{\text{Si}}$  i 70 sykler. Levetiden er mer avhengig av last og cellefabrikasjonen, enn av den initielle krystalliniteten til materialet.

I sum har dette arbeidet gitt et godt startpunkt for fabrikasjonen av plomme-skallpartikler ved å bruke Si nanopartikler fra en FSR. Et homogent belegg av oksid ble deponert, og

---

et karbonbelegg ble observert for noen få prøver. Elektrokjemiske resultater fra syklingen av ren silisium viste en høy avhengighet av last og cellefabrikasjon, og det er derfor imperativt å holde elektrode- og cellefabrikering så reproduserbart og likt som mulig for sammenligningsgrunnlag.

# Contents

---

<b>Preface</b>	<b>i</b>
<b>Acknowledgements</b>	<b>ii</b>
<b>Abstract</b>	<b>iv</b>
<b>Sammendrag</b>	<b>vii</b>
<b>Contents</b>	<b>ix</b>
<b>List of Abbreviations</b>	<b>x</b>
<b>List of Figures</b>	<b>xii</b>
<b>List of Tables</b>	<b>xv</b>
<b>1 Introduction</b>	<b>1</b>
1.1 Aim of this work . . . . .	3
<b>2 Theoretical Background</b>	<b>5</b>
2.1 Lithium-ion batteries . . . . .	5
2.1.1 Electrochemical principles . . . . .	6
2.1.2 Components of a lithium-ion battery . . . . .	8
2.2 Silicon as anode material . . . . .	12
2.2.1 Degradation mechanisms . . . . .	13
2.3 Overcoming challenges of alloying anodes . . . . .	17
2.3.1 Silicon nanoparticles from a Free Space Reactor . . . . .	17
2.3.2 Coating . . . . .	18
2.3.3 Yolk-shell particles . . . . .	22
2.3.4 Sol-gel coating . . . . .	24
2.4 Characterization techniques . . . . .	27
2.4.1 Structural characterization . . . . .	27
2.4.2 Electrochemical characterization . . . . .	31
<b>3 Experimental</b>	<b>37</b>
3.1 Preparation of active material . . . . .	37
3.1.1 Amorphous reference silicon . . . . .	37
3.1.2 Crystalline reference silicon . . . . .	38
3.1.3 Sol-gel coating of oxide layer . . . . .	38
3.1.4 Carbon coating of core-shell particles . . . . .	40
3.2 Characterization methods . . . . .	41
3.3 Slurry and electrode preparation . . . . .	43
3.4 Cell assembly . . . . .	44
3.5 Electrochemical testing . . . . .	45
3.5.1 Galvanostatic charge-discharge . . . . .	46

---

3.5.2	Electrochemical Impedance Spectroscopy . . . . .	47
<b>4</b>	<b>Results</b>	<b>49</b>
4.1	Pure silicon as reference . . . . .	49
4.1.1	Structural characterization . . . . .	49
4.1.2	Electrochemical results . . . . .	56
4.2	Oxide coating by TEOS . . . . .	64
4.2.1	Structural characterization . . . . .	64
4.2.2	Electrochemical results . . . . .	67
4.3	Carbon coating by RF . . . . .	73
4.3.1	Structural characterization . . . . .	74
4.4	Final characterization of multiple core-shell particles . . . . .	76
4.4.1	Material properties . . . . .	76
4.4.2	Crystallinity . . . . .	80
4.4.3	Carbon content . . . . .	81
<b>5</b>	<b>Discussion</b>	<b>83</b>
5.1	Pure silicon reference . . . . .	83
5.1.1	Material properties . . . . .	83
5.1.2	Electrochemical analysis . . . . .	85
5.1.3	Effect of heat treatment on electrochemical cycling . . . . .	89
5.2	Core-shell particles, Si@SiO <sub>2</sub> . . . . .	90
5.2.1	Material properties . . . . .	90
5.2.2	Partial control of oxide coating . . . . .	92
5.2.3	Electrochemical analysis . . . . .	92
5.3	Double core-shell particles, Si@SiO <sub>2</sub> @C . . . . .	94
5.3.1	Material properties . . . . .	95
5.3.2	Properties of carbon coating . . . . .	95
<b>6</b>	<b>Conclusion</b>	<b>101</b>
<b>7</b>	<b>Further work</b>	<b>103</b>
	<b>Bibliography</b>	<b>104</b>
<b>A</b>	<b>Oxide and carbon coating process</b>	<b>III</b>
<b>B</b>	<b>Slurry preparation and tape casting of electrode</b>	<b>V</b>
<b>C</b>	<b>Electrochemical cycling programs</b>	<b>VII</b>
C.1	Galvanostatic charge-discharge at unlimited capacity . . . . .	VII
C.2	Galvanostatic charge-discharge at limited capacity . . . . .	VII
C.3	Electrochemical Impedance Spectroscopy . . . . .	VIII

# List of Abbreviations

---

## Abbreviations & Terms

(H)EV	(Hybrid) electric vehicles
AC	Alternating current
CA	Conductive additives
CPE	Constant phase element
FSR	Free space reactor
ICL	Irreversible capacity loss
IFE	Institute for Energy Technology
LIB	Lithium-ion battery
NTNU	Norwegian University of Science and Technology
Pdi	Polydispersity index
PSD	Particle size distribution
Redox	Reduction-oxidation
RF	Resorcinol-formaldehyde
rpm	Rotations per minute
RT	Room temperature
SEI	Solid-electrolyte interface
SiNP	Silicon nanoparticle
SOC	State of Charge
Sol-gel	Solution-gelation
UiO	University of Oslo
WD	Working Distance

## Characterization methods

(G)EIS	(Galvanostatic) Electrochemical Impedance Spectroscopy
BET	Brunauer-Emmett-Teller
DLS	Dynamic Light Scattering
EDS	Energy Dispersive X-ray Spectroscopy
ELS	Electrophoretic Light Scattering
FE-SEM	Field-Emission Scanning Electron Microscope
HAADF	High Angle Annular Dark Field
STEM	Scanning Transmission Electron Microscopy
XRD	X-ray Diffraction

**Chemical elements**

Ar	Argon
C	Carbon
CTAB	Hexadecyltrimethylammonium bromide
Cu	Copper
DMC	Dimethyl carbonate
EC	Ethylene carbonate
FEC	Fluoroethylene carbonate
Li	Lithium
PC	Propylene carbonate
Si	Silicon
Silica	Silicon dioxide (SiO <sub>2</sub> )
TEOS	Tetraethyl orthosilicate
VC	Vinylene carbonate

**Letters and symbols**

°C	Degree of Celcius
$C_{dl}$	Double layer capacitance
$d_H$	Hydrodynamic particle diameter
$R_{\Omega}$	Electrolyte resistance
$R_{CT}$	Charge transfer resistance
$Z_W$	Warburg impedance

**Units**

Ah	Ampere-hours
at%	Atomic percent
kV	kilo-volts
kWh	kilowatt-hour
M	Molar
V	Volt
wt%	Weight percent

# List of Figures

---

1.1	Battery technology development 2008-2015 . . . . .	1
1.2	Aim of coating method . . . . .	3
2.1	Rechargeable battery systems . . . . .	5
2.2	Schematic of LIB during discharge . . . . .	7
2.3	Molecular structures of electrolyte carbonates . . . . .	9
2.4	Graphical representation of SEI-layer . . . . .	10
2.5	Silicon electrode failure mechanisms . . . . .	13
2.6	Lithiation mechanisms in Si reference . . . . .	15
2.7	Schematic of FSR process . . . . .	18
2.8	Growth mechanism of Si in FSR reactor . . . . .	18
2.9	Schematic of carbon point contact vs. coating . . . . .	19
2.10	TEM micrographs of carbon coating from starch and sucrose . . . . .	21
2.11	TEM micrograph of carbon coated Si by spray-pyrolysis . . . . .	22
2.12	SEM micrographs of yolk-shell particles . . . . .	23
2.13	Polymerization of resorcinol and formaldehyde . . . . .	27
2.14	t-plot method . . . . .	29
2.15	Illustration of non-spherical particle . . . . .	30
2.16	Illustration of how to obtain dQ/dV plot . . . . .	33
2.17	Randles equivalent circuit . . . . .	34
2.18	Analysis of Nyquist plot . . . . .	35
3.1	Experimental set-up for collection of Si@SiO <sub>2</sub> . . . . .	39
3.2	Carbonization of RF-precursor . . . . .	41
3.3	Coin cell and PAT-cell schematics . . . . .	45
4.1	SEM micrographs of amorphous silicon reference material . . . . .	50
4.2	Particle size distribution a-Si ref . . . . .	51
4.3	SEM micrographs of silicon agglomerates . . . . .	51
4.4	SEM micrographs of crystalline silicon reference material . . . . .	52
4.5	Particle size distribution c-Si ref . . . . .	52
4.6	SEM micrographs of silicon chunks . . . . .	53
4.7	BET surface area of Si reference . . . . .	53
4.8	Thermogravimetric mass loss curves for Si reference . . . . .	54
4.9	XRD diffractograms of reference silicon . . . . .	55

---

4.10 XRD diffractogram of a-Si ref . . . . .	56
4.11 Galvanostatic charge-discharge of Si ref to an unlimited capacity . . . . .	57
4.12 Galvanostatic charge-discharge of Si ref at a limited capacity . . . . .	58
4.13 Galvanostatic charge-discharge of a-Si ref (05) at a limited capacity . . . . .	59
4.14 Voltage curves for Si reference . . . . .	59
4.15 dQ/dV plots of Si reference . . . . .	60
4.16 Nyquist plots from EIS of Si reference . . . . .	62
4.17 Nyquist plots from EIS of Si reference at 50% and 100% SOC . . . . .	63
4.18 SEM micrographs of oxide coated silicon, Si@SiO <sub>2</sub> . . . . .	64
4.19 Particle size distribution Si@SiO <sub>2</sub> . . . . .	65
4.20 TEM micrograph of Si@SiO <sub>2</sub> with EDS map . . . . .	66
4.21 TEM micrograph of Si@SiO <sub>2</sub> with EDS map . . . . .	66
4.22 XRD diffractograms of Si@SiO <sub>2</sub> vs. a-Si ref . . . . .	67
4.23 Galvanostatic charge-discharge of Si@SiO <sub>2</sub> to an unlimited capacity . . . . .	68
4.24 Galvanostatic charge-discharge of Si@SiO <sub>2</sub> at a limited capacity . . . . .	68
4.25 Voltage curves for Si@SiO <sub>2</sub> . . . . .	69
4.26 dQ/dV plots of Si@SiO <sub>2</sub> . . . . .	70
4.27 dQ/dV plots of a-Si ref and Si@SiO <sub>2</sub> . . . . .	70
4.28 Nyquist plots from EIS of Si@SiO <sub>2</sub> . . . . .	71
4.29 Nyquist plots from EIS of Si@SiO <sub>2</sub> vs. a-Si ref at 50% and 100% SOC . . . . .	72
4.30 Zeta potential of a-Si ref with CTAB . . . . .	73
4.31 SEM micrographs of Si@SiO <sub>2</sub> @C . . . . .	74
4.32 STEM micrographs of Si@SiO <sub>2</sub> @C . . . . .	75
4.33 TEM micrographs of Si@SiO <sub>2</sub> @C . . . . .	75
4.34 SEM micrographs of Si, Si@SiO <sub>2</sub> and Si@SiO <sub>2</sub> @C . . . . .	77
4.35 DLS particle size distributions of a-Si ref and Si@SiO <sub>2</sub> . . . . .	78
4.36 BET surface area of a-Si ref, Si@SiO <sub>2</sub> and Si@SiO <sub>2</sub> @C . . . . .	79
4.37 XRD of all Si@SiO <sub>2</sub> @C batches . . . . .	80
4.38 TGA mass loss curves for successful Si@SiO <sub>2</sub> @C . . . . .	82
4.39 TGA mass loss curves for failed Si@SiO <sub>2</sub> @C . . . . .	82
5.1 Subset of voltage plot for Si reference . . . . .	86
5.2 First lithiation peak of Si reference . . . . .	87
5.3 Lithium complexes in electrolyte solution . . . . .	90
5.4 Silica found after oxide coating . . . . .	91
5.5 Effect of pH on silica growth . . . . .	92
5.6 First lithiation peak of Si@SiO <sub>2</sub> and a-Si ref . . . . .	93

5.7	SEM micrograph and schematic of secondary particles . . . . .	95
5.8	Schematic of carbon coating for microbeads/pomegranate structure . . . . .	97
5.9	Effect of pH on polymerization time for RF resin . . . . .	98
A.1	Flow chart of coating process . . . . .	III



# List of Tables

---

2.1	Comparison of electrochemical properties of various anode materials . . . .	12
2.2	Lithiation and de-lithiation mechanisms . . . . .	14
3.1	Synthesis parameters for oxide coating . . . . .	39
3.2	Synthesis parameters for carbon coating . . . . .	41
3.3	Active material masses and loading of Si electrodes . . . . .	44
3.4	Half-cells and electrochemical programs . . . . .	47
4.1	BET surface area of Si reference . . . . .	54
4.2	Summary of unlimited cycling of Si reference . . . . .	57
4.3	Reversible capacities and lifetime for Si reference . . . . .	57
4.4	Summary of unlimited cycling Si reference . . . . .	58
4.5	Impedance data of Si reference . . . . .	61
4.6	Summary of cycling of Si@SiO <sub>2</sub> . . . . .	69
4.7	Impedance data of Si@SiO <sub>2</sub> vs. a-Si ref . . . . .	71
4.8	Elemental composition of a-Si ref, Si@SiO <sub>2</sub> and Si@SiO <sub>2</sub> @C . . . . .	78
4.9	BET surface area measurements of a-Si ref, Si@SiO <sub>2</sub> and Si@SiO <sub>2</sub> @C . . . . .	79
4.10	TGA showing carbon content of RF-batches . . . . .	81
5.1	Areal loading of Si reference cells . . . . .	88
5.2	Synthesis of Si@SiO <sub>2</sub> for characterization . . . . .	92
B.1	Recipe for slurry . . . . .	V



# 1 Introduction

---

Today, batteries are all around us. We use a wide range of different types of batteries, and many of these are designed for specific purposes and with different limitations of its chemical and safety features. Lithium-ion batteries (LIBs) however, are mainly used in two (quite different) sectors, namely portable electronics and transportation. The reason for this is due to its high energy density, and the fact that LIBs are rechargeable [2]. Its high energy density makes the battery system easier to transport, ideal for cars and portable electronics.

The ability to design the Li-ion battery and its performance for a range of applications make its use popular in many fields. However, battery research is centered around achieving even higher energy densities to extend the driving range of electric (and hybrid electric) vehicles (EV and HEV). For improved batteries, it is imperative that performance is increased while decreasing cost and safety issues. Figures of merit for EV applications call for cutting the price per kilowatt-hour (kWh) in half, and doubling the present energy density [2]. In the Global EV Outlook 2016 from the International Energy Agency, cost (USD/kWh) was seen to have decreased since 2008, while energy density (Wh/L) increased in the same years. This development can be seen in Figure 1.1.

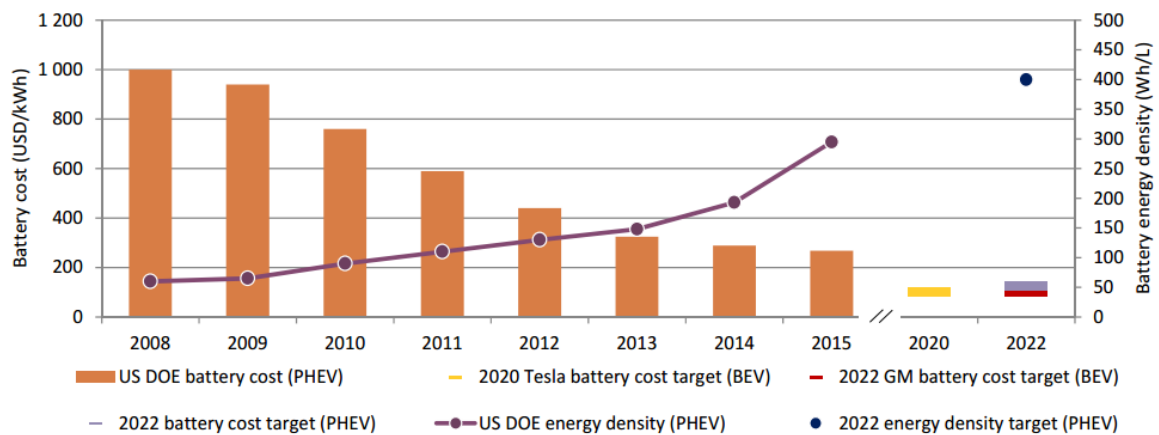


**Figure 1.1:** Battery technology development. Original illustration appears in [3].

These improvements would not only be beneficial for the transportation sector, but as the world consumes more and more energy, almost 159,000 TWh each day [4], improvements in the grid storage, especially in terms of cost per kWh would help make better use of renewable energy resources as well. To make best use of renewable energy resources such as solar, tidal and wind, we need efficient energy-storage systems to store excess

energy that can be used in periods of low production or high demand. Today, we only have the capacity to store 1% of the energy consumed world wide, and 98% of this is by pumped-storage hydroelectricity [5]. The worlds population is growing by 83 million people annually, with a projected increase of more than one billion within the next 15 years [6], demanding an increase in both energy supply and sustainable storage mechanisms without increasing CO<sub>2</sub> emissions. This task is not looked upon lightly by energy researchers, and there is an ongoing world wide effort to solve these issues.

Silicon has emerged as a promising new alternative to graphite, traditionally used in Li-ion batteries, due to its theoretical ability to store ten times the amount of lithium ions in its structure [7]. With this alloying ability comes a volume change of around 300%, and the particles tend to crack under repeated expansion and contraction leading to failure of the battery. In addition, another issue faced by silicon is its low electronic conductivity and therefore ineffective distribution and transportation of charge. These problems have been proposed solved by several different approaches: (i) Particle-based structures containing nanoparticles, core-shell particles [8] and yolk-shell particles/wires [9, 10], (ii) Porous silicon design [11], (iii) Nanowires and nanotubes [12, 13], (iv) Silicon based composites [14], and (v) more complex structures [15]. All of which have demonstrated superior performance to bulk Si.

## 1.1 Aim of this work

In order to apply silicon as an anode in Li-ion batteries and benefit from its high energy density, it is imperative to solve the issues regarding changes experienced during cycling. In this thesis, nanoparticles have been tailored to enable production a new type of particle, a yolk-shell particle, designed to withstand the large volume change as well as produce stable electrochemical results. To obtain yolk-shell particles, several steps are needed, and the initial two steps, producing double core-shell particles, have been investigated for this thesis. The work was divided into two parts, each aimed at understanding different aspects of the coating processes involved in fabricating a double core-shell structure using silicon nanoparticles produced in a Free Space Reactor.

1. The first part included characterization and electrochemical cycling of reference silicon material to obtain a base-line, a reference point for determining whether or not the new geometry provided more stable results. Here both amorphous and crystalline pure silicon nanoparticles were cycled and compared.
2. The second step was to understand how the coating layers were formed and behaved, as well as how to control these processes in order to produce the needed thicknesses in the coatings. A two-step coating procedure to produce double core-shell particles was investigated, first an oxide coating of 50-80 nm followed by a carbon coating of 5-10 nm, and is shown in Figure 1.2.



**Figure 1.2:** Producing a double core-shell particle by oxide and carbon coating.



## 2 Theoretical Background

### 2.1 Lithium-ion batteries

The lithium-ion battery (LIB) is the battery of choice in many of today's applications due to its high energy and power density, shown in Figure 2.1. Since its commercialization in 1991 by Sony it has gained a large portion of the energy storage market, and continues to be one of the most well known and used battery types, in addition to the lead-acid battery [16]. Being a secondary battery, it is an electrochemical device converting chemical energy into electrical energy, and vice versa, meaning it can be charged, used and recharged for further use. Secondary batteries are therefore often referred to as rechargeable, and these two names are both frequently used. Applications that require high energy density, like electric and hybrid electric vehicles (EV and HEV) and portable electronics are often powered by these rechargeable energy systems. For storage of energy in a sufficient and feasible manner, the battery must convert between these two energy forms safely and efficiently.

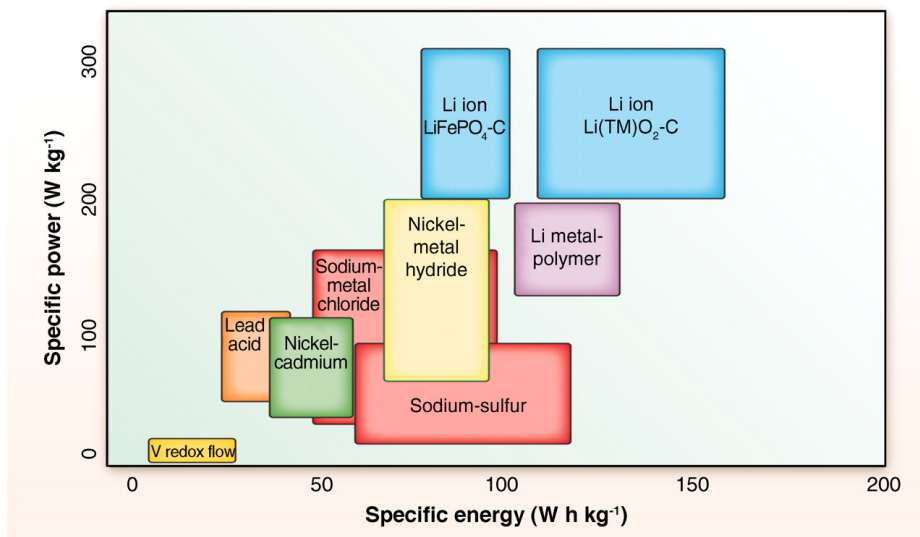


**Figure 2.1:** Comparing different rechargeable battery systems, highlighting the superiority of lithium-ion technologies with respect to specific power and energy. Original illustration appears in Dunn et al. [2].

A lithium (Li) based battery has many advantages, as Li is the most electropositive (reduction potential of  $-3.04$  V vs. a standard hydrogen electrode) and lightest ( $M=6.94$  g/mol) metal, thus facilitating the design of storage systems with a high energy den-

sity [17]. The electrical energy that can be stored in a LIB is either expressed by weight (Wh/kg) or volume (Wh/l), and is in turn dependent on the cell potential (V) and capacity (Q) by the following relation,  $E=Q \cdot V$ . For tailoring the battery to a specific use, several electrochemical cells can be connected in series or parallel to achieve the desired voltage and capacity.

### 2.1.1 Electrochemical principles

The working principle of a Li-ion battery system is similar to other rechargeable battery systems, and follows reduction-oxidation (redox) reactions on both electrodes. The electrodes are most often made of two lithium insertion materials, traditionally a graphite intercalation anode and a lithium metal oxide intercalation cathode (e.g.  $\text{LiCoO}_2$ ). By using a lithium conducting and electrically insulating electrolyte as a transportation medium, the ions can reversibly intercalate into the two electrodes due to a potential difference between them, while electrons are conducted in an outer circuit. In secondary batteries where reduction and oxidation reactions take place on both electrodes, anode and cathode will here be defined so that the reduction occurs on the cathode during discharge of the battery (de-lithiation of anode), as presented in Figure 2.2. As the cations are conducted through the electrolyte from the anode to the cathode, the electrons consumed at the cathode (and released at the anode) are conducted in the outer circuit to ensure charge balance. During charge (lithiation of anode), the reverse happens.

The main components of a secondary battery are:

1. A positive electrode (**cathode**) - Will accept electrons from the external circuit during discharge, and reduction reactions occur here during redox.
2. A negative electrode (**anode**) - Will supply electrons to the external circuit during discharge, and oxidation reactions occur here during redox.
3. The **electrolyte** - An ionic conductor used to transfer ions between the two electrodes. For LIBs it typically consists of a lithium salt dissolved in two or more carbonates. It must also be electrically insulating to prevent short circuit of the battery, and thereby enable the electrons to move through the outer circuit.

A porous separator is also needed when using a liquid electrolyte to physically isolate the two electrodes, whilst allowing the electrolyte and  $\text{Li}^+$  -ions to penetrate.

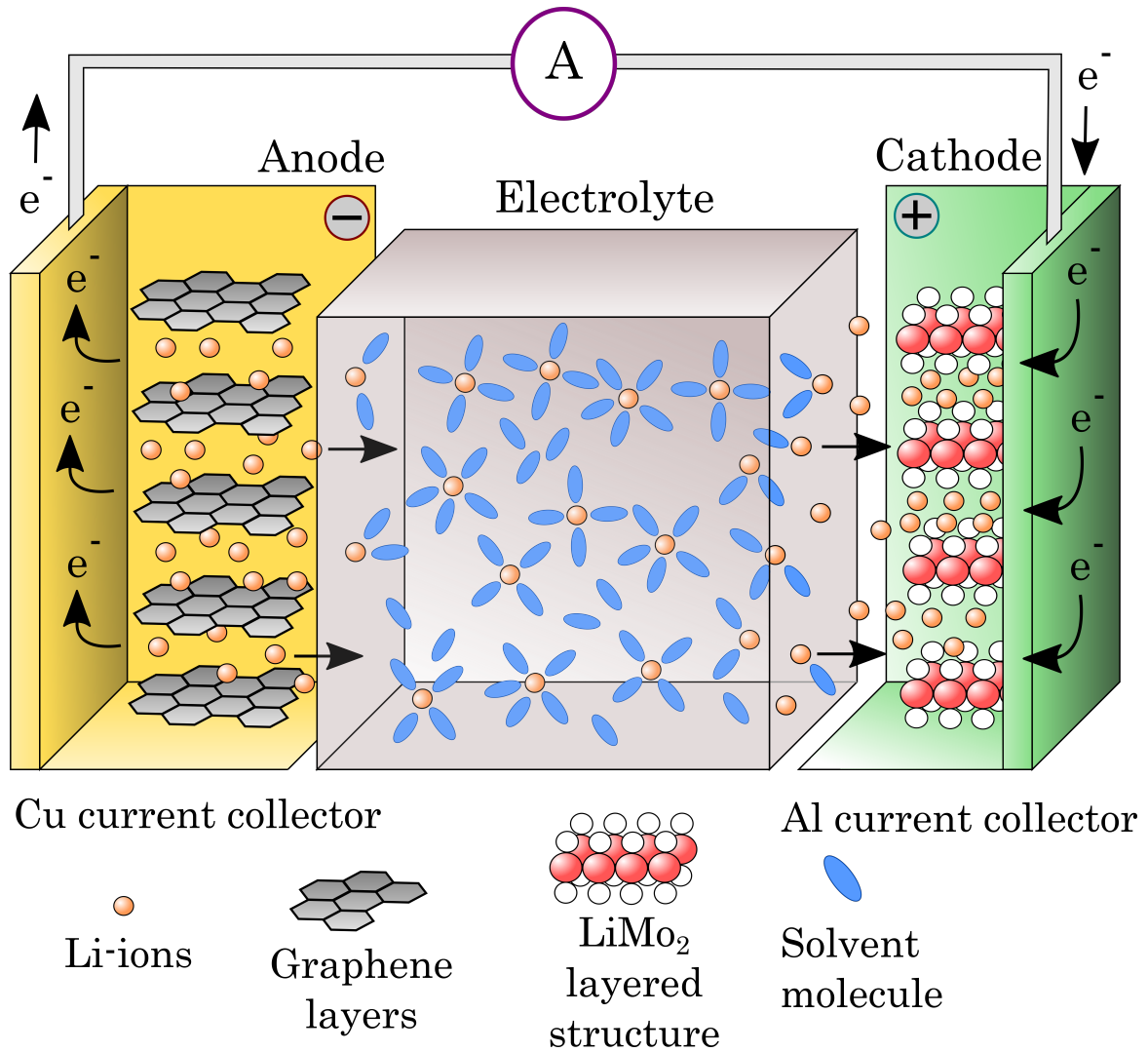
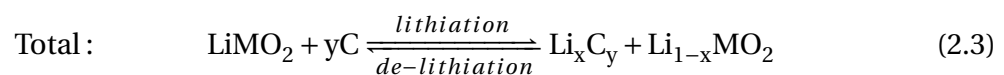
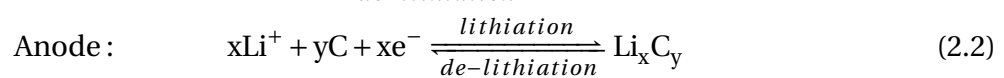
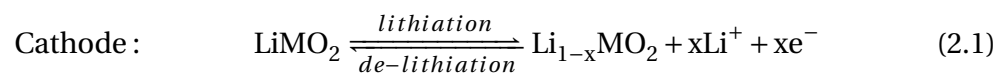


**Figure 2.2:** Schematic of a LIB during discharge. Illustration adapted from Dunn et al. [2].

LIBs are most commonly based on the intercalation of ions into a host structure (like graphite), and as the anode is lithiated the potential difference between the electrodes cause ions to move from the cathode to the anode. During de-lithiation, the ions move back into the cathode. This shuttle of  $\text{Li}^+$ -ions has given the name "rocking chair mechanism" to the system [17, 18]. When the cathode material is  $\text{LiMO}_2$ , and the anode is a carbonaceous material the redox reaction proceeds according to the following:



In the equations above, M is a transition metal, traditionally Co, Mn or Ni [17]. The maximum value of  $x$  in  $\text{Li}_{1-x}\text{MO}_2$  is dependent on the metal M due to structural restrictions, and is typically around 0.5 for  $\text{LiMO}_2$ , as it would otherwise collapse upon extensive lithiation. The largest possible value for  $y$  in  $\text{Li}_x\text{C}_y$  is 6, resulting in  $\text{LiC}_6$ , where  $\text{Li}^+$ -ions are located at the center of the hexagonal rings in the graphene layers.

### 2.1.2 Components of a lithium-ion battery

The theoretical capacity of a cell can be defined as the total quantity of electric charge involved in the chemical reaction, and is typically given in milliampere-hours per gram active material (mAh/g). It is determined by which active materials<sup>1</sup> are used in the anode and cathode, as well as the amount of that material in the cell. However, due to the need of other components (such as electrolyte, separator and casing) in the cell, the actual capacity is only a fraction of this. Some general remarks on the main components of a traditional LIB will be presented here, before silicon as an alternative anode material will be discussed. The theory in this section is based on Linden and Reddy [19] unless otherwise specified.

#### 2.1.2.1 Electrolytes

In general, electrolytes are designed for specific battery applications, and its contents can therefore vary accordingly. But the basic criteria that should be met are:

- The electrolyte should promote a high  $\text{Li}^+$ -ion conductivity for efficient transport between electrodes, as well as be electrically insulating to prevent electron exchange between electrodes, which would lead to short circuiting of the battery.
- The solution should have a wide electrochemical window, preferably outside the voltages of the redox reaction, or with the ability to form a stable and protective passivation film, even under large volume change.
- The solution should be able to operate in a wide temperature range, and have an appropriate viscosity.
- The solvents and solutes should have low toxicity and price.

Liquid electrolytes are most often used in LIBs, and are made by the dissolution of a lithium salt, the solute, (e.g. lithium hexafluorophosphate,  $\text{LiPF}_6$ ) in organic solvents,

---

<sup>1</sup>The material taking part in the lithiation/de-lithiation process. For traditional cells the active material in the anode is carbon, for this thesis it will be silicon or a silicon/oxide composite.

typically carbonates (e.g. ethylene carbonate/propylene carbonate/dimethyl carbonate, EC/PC/DMC).  $\text{LiPF}_6$  is currently most often utilized as the salt due to its high ionic conductivity ( $>10^{-3}$  S/cm), high solubility of  $\text{Li}^+$ -ions, and being acceptably safe [19]. The solvents in use today are composed of at least one cyclic carbonate, mostly EC, used to dissolve the  $\text{LiPF}_6$ -salt. EC is aprotic, polar and has a high dielectric constant, facilitating solvation at concentrations over 1 M. As cyclic carbonates are highly viscous, and EC has a melting point of  $36^\circ\text{C}$ , the addition of one or more linear carbonates, like DMC is necessary to obtain a more appropriate viscosity. Additives can also be used in the electrolyte to achieve certain benefits (e.g. vinylene carbonate, VC and fluoroethylene carbonate, FEC), and this will be further discussed in Section 2.1.2.1. The molecular structures of the used carbonates in this thesis can be seen in Figure 2.3.

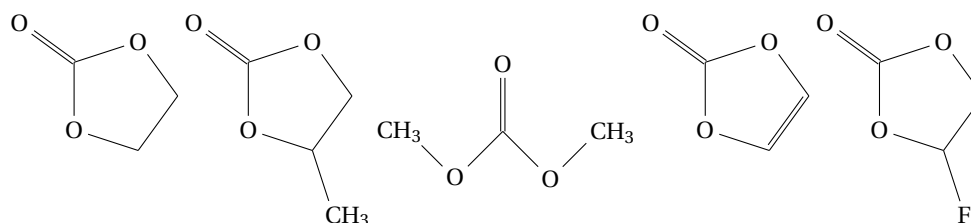


**Figure 2.3:** Molecular structures of EC, PC, DMC, VC and FEC.

### Solid-electrolyte interface layer

A large amount of research has been done on the decomposition of electrolyte species at the surface of anodes, as this decomposition leads to the formation of a solid-electrolyte interface (SEI) layer [20, 21]. For commercial LIBs (C/ $\text{LiCoO}_2$ ), the redox reaction of graphite will proceed in the range 0.2-0.05 V vs.  $\text{Li}/\text{Li}^+$  and that of the  $\text{LiCoO}_2$  at around 4 V. An electrolyte with  $\text{LiPF}_6$  in EC/DMC will only be stable from 0.8 V to 4.5 V, leading to decomposition of the electrolyte itself during the redox of graphite, and the conclusion that this cell would be thermodynamically unstable in these commercial electrolytes.

However, the initial decomposition of electrolyte will result in a passivating film, inhibiting further side reactions and the battery will operate under kinetic stability [22]. This initial decomposition is due to tunneling of electrons from the anode surface, and leads to an inner layer composed of mostly  $\text{LiF}$ ,  $\text{Li}_2\text{O}$  and  $\text{Li}_2\text{CO}_3$  and a more porous, organic outer layer (e.g. lithium ethylene dicarbonate,  $\text{Li}_2\text{EDC}$ ) [21]. The composition of the resulting SEI layer can be seen in Figure 2.4.

Although this passivation film is essential for stable cycling of the electrode, it leads to an irreversible capacity loss (ICL) in the first few cycles due to trapping of  $\text{Li}^+$ -ions. An

unnecessarily thick SEI layer could eventually block  $\text{Li}^+$  transport and lead to poor cell lifetimes, making the choice of electrolyte with regard to the electrode material crucial [17]. An effective SEI layer should be mechanically and chemically stable, be permeable to  $\text{Li}^+$ -ions and passivate the surface to reduce the amount of undesired electron transfer reactions. To achieve this it is important that both the salts and solvents are thermodynamically compatible with the electrodes over a broad range of potentials.

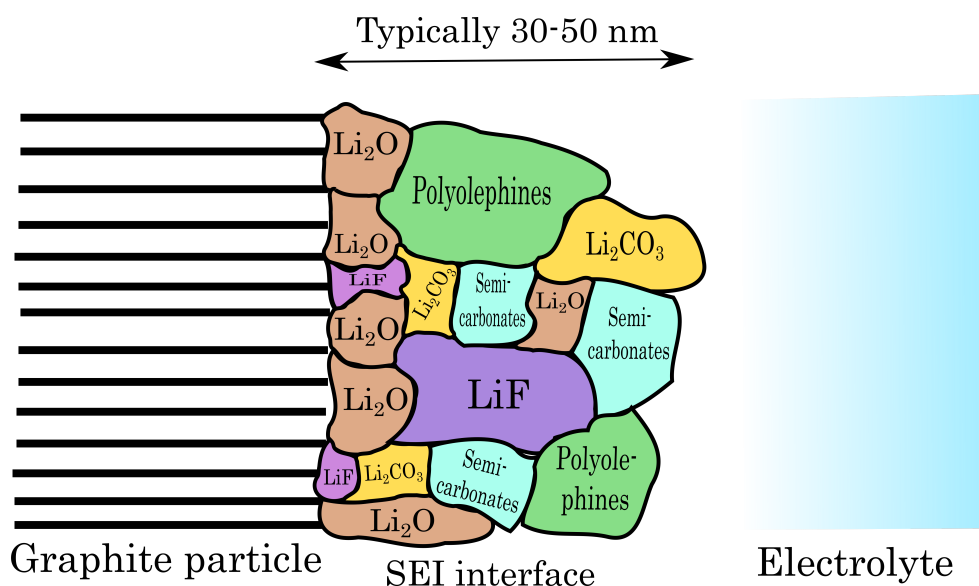


**Figure 2.4:** A graphical representation of the SEI-layer and its components. Illustration adapted from [23].

### Electrolyte additives

To influence the performance of LIBs and control some of the processes occurring dependent upon what materials are used, additives can be added to the electrolyte. An introduction to the vast number of publications on this topic was done in a review by Zhang [24], using graphite as anode material, and the most important topic for the chemicals used in this thesis is summarized here based on its intended function:

- **Improvement of SEI formation:** As mentioned, SEI is formed through a series of competing reactions, and additives promoting or inhibiting the more favorable or disadvantageous of these reactions, respectively, will control the formation of the SEI. This way a more stable SEI can be formed on the surface of the active particles. Vinylene carbonate (VC) is an example of a reactive additive (or reductive additive), reacting on both the anode and cathode side, and improves the anode cyclability by decreasing the irreversible capacity [25, 26]. Fluoroethylene carbonate (FEC), another reductive agent, can lose a HF molecule to form a VC molecule,

and in turn serve as a reactive additive while the HF improves the cyclability of metallic lithium [27]. FEC was the study of a recent review by Markevich et al. [28], and was found to enhance the cyclability of LIBs by improving the SEI formation.

### 2.1.2.2 Electrode materials

For the electrodes to work ideally, some general requirements for the materials used are presented by Linden and Reddy [19]:

- The material should be environmentally friendly and available at a low cost.
- The structure of the material should be able to accommodate as many lithium ions per host atom as possible to maximize capacity, as well as de-intercalate/-alloy these ions efficiently. The host atoms should also be lightweight.
- The materials should have high electronic and ionic conductivity for fast transport of  $\text{Li}^+$ -ions and electrons.
- Both electrodes should be insoluble in, and compatible with the electrolyte.

Anode materials should have the lowest possible redox potential with respect to  $\text{Li}/\text{Li}^+$  to achieve high energy density, and can be divided into three main groups based on their reaction mechanism with Li: Inter/de-intercalation materials (e.g. carbon based), alloy/de-alloy materials (e.g. silicon) and conversion materials (not discussed in this thesis). Most commercial LIBs today are based on intercalation compounds, like graphite, to promote fast diffusion of  $\text{Li}^+$ -ions into and out of the structure. They are usually layered, or composed of tunneling crystal structures (e.g. zeolites) and the  $\text{Li}^+$ -ions reside in interstitial sites within the layers. The intercalation should not cause high strains or irreversible structural changes in the material in order to obtain good capacity retention over many cycles.

Unfortunately, both the advantage and draw-back of graphite lies in its layered structure as it allows for stable intercalation, but limits  $\text{Li}^+$ -ion uptake to one Li per six C atoms in the lithium-rich phase,  $\text{LiC}_6$ , leading to a low theoretical capacity of 372 mAh/g [17]. As an alternative, alloy materials have been intensively studied the past ten years, and both silicon (Si) and tin (Sn) have emerged as promising alternatives to graphite. As silicon is the main topic of this thesis it will be further discussed in section 2.2, while alloying anodes in general will be presented here. Various anode materials were subject for discussion in a review by Zhang [29] from 2011, and some of the findings are summarized in Table 2.1.

**Table 2.1:** Comparison of electrochemical properties of various anode materials. Adapted from Zhang [29], and values may vary slightly from the values otherwise used in the text.

Materials	Intercalation		Alloy	
	Li	C	Si	Sn
Density [g/cm <sup>3</sup> ]	0.53	2.25	2.33	7.29
Lithiated phase	Li	LiC <sub>6</sub>	Li <sub>22</sub> Si <sub>5</sub>	Li <sub>22</sub> Sn <sub>5</sub>
Theoretical specific capacity [mAh/g]	3862	372	4200	994
Volume change [%]	100	12	420	260
Potential vs. Li [ $\approx$ V]	0	0.05	0.4	0.6

Alloying anode materials such as Si and Sn react with Li by a very different mechanism than the intercalation seen when using graphite. The alloying with Li involves the breaking of bonds between host atoms, which opens up for a much higher uptake of Li in the structure. As Li is also trapped during formation of the SEI, the alloying anodes often suffer from a very high first-cycle irreversible capacity loss. The volume change seen with high uptake of lithium will lead to major structural changes in the process, and constitutes the alloying anodes' main challenge as it often leads to pulverization of the electrode and further poor cycle stability, making it difficult to use for practical purposes [30–33]. Preventing the mechanical fracture during cycling is essential for being able to utilize their high capacity and thereby providing stable high energy density LIBs for the market.

## 2.2 Silicon as anode material

Silicon is considered the most promising alternative as an anode material due to its exceptionally high theoretical capacity (3,579 mAh/g vs. 372 mAh/g for graphite) when lithiated to Li<sub>15</sub>Si<sub>4</sub>, low working potential of 0.4 vs. Li/Li<sup>+</sup> and high abundance in the earths crust. The study of silicon began in 1976, when Lai [34] presented a solid lithium-silicon battery with the conclusion that silicon showed promise as an alternative anode material for high-energy-density batteries, and researchers have since studied the subject intensively [7, 31, 35, 36]. Its major advantage lies in the fact that each host atom can hold on average 3.75 Li-atoms (based on Li<sub>15</sub>Si<sub>4</sub>), giving a very high capacity compared to todays commercial materials [36].

However, many obstacles were unveiled when electrochemically tested, including the volume change of  $\sim$ 300% compared to graphites' 10%. This volume change is at the

heart of the research question, as it will lead to pulverization of the material, an unstable SEI layer and bad electrochemical performance.

### 2.2.1 Degradation mechanisms

The three most important material challenges related to the use of silicon as an anode include material pulverization, morphology and volume change of the electrode and an unstable SEI. A summary of these challenges was done by Wu and Cui [37], and can be seen in Figure 2.5.

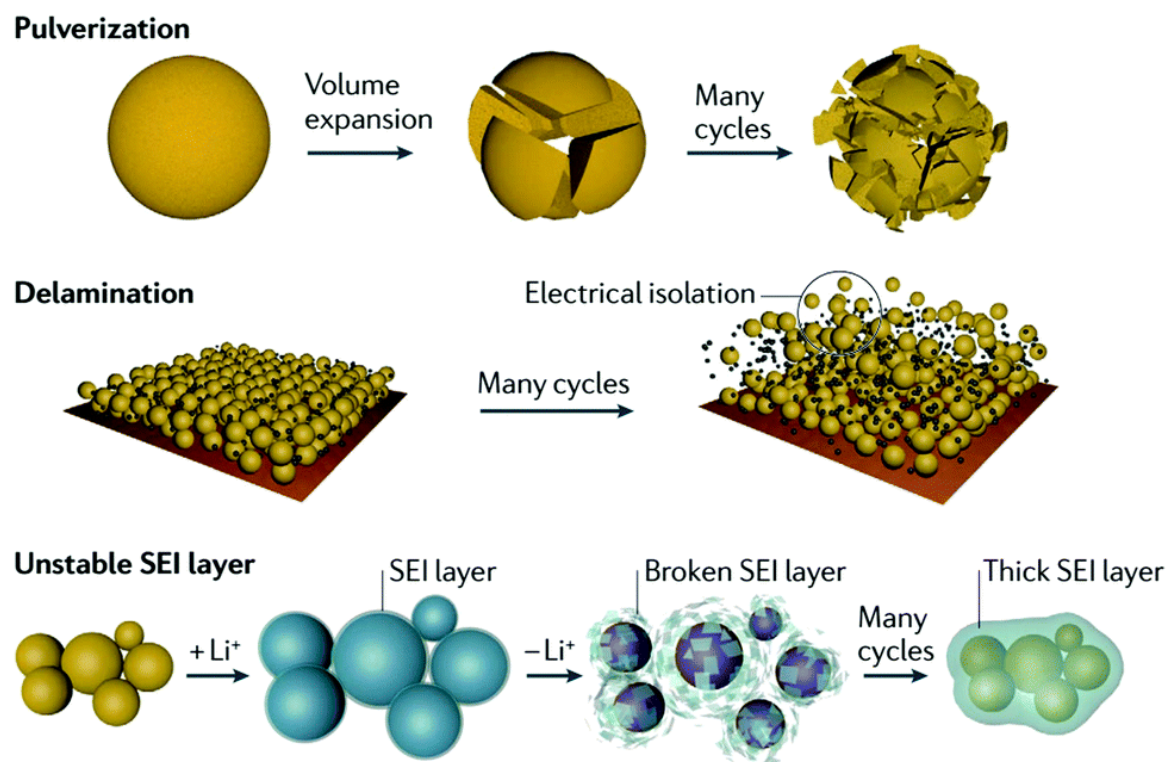
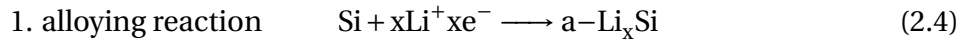


**Figure 2.5:** Si electrode failure mechanisms: (a) material pulverization, (b) morphology and volume change of the electrode and (c) unstable solid-electrolyte interphase. Original illustration appears in [38].

#### 2.2.1.1 Pulverization of material

Silicon is an alloy anode, and the alloying occurs in two stages [36, 39–41]. The initial lithiation of crystalline silicon forms an amorphous alloy phase consisting of Si and Li ( $a\text{-Li}_x\text{Si}$ ), and the capacity of this plateau was determined by an in-situ X-ray diffraction

(XRD) study to be 3,250 mAh/g [42]. At higher capacities the same study observed the formation of a  $\text{Li}_{15}\text{Si}_4$  phase, corresponding to a capacity of 3,579 mAh/g.



Further lithiation and de-lithiation mechanisms have been investigated by Ogata et al. [41], and a summary of the proposed reactions between 0.05-1 V is shown in Table 2.2.

**Table 2.2:** Lithiation and de-lithiation mechanisms proposed between 50 mV and 1 V [41].

Cycle	Reaction	Potential
1 <sup>st</sup> cycle lithiation	1 $\text{c-Si} \rightarrow \text{a-Li}_x\text{Si} \rightarrow \text{c-Li}_{3.75}\text{Si}$	0.10 V
1 <sup>st</sup> cycle de-lithiation	1 $\text{a-Li}_{\sim 3.5}\text{Si} \rightarrow \text{a-Li}_{\sim 2.0}\text{Si}$	0.27 V
	2 $\text{c-Li}_{3.5}\text{Si} \rightarrow \text{a-Li}_{1.1}\text{Si}$	0.43 V
$\geq 2^{\text{nd}}$ cycle lithiation	1 $\text{a-Si} \rightarrow \text{Li}_{\sim 2.0}\text{Si}$	0.30-0.25 V <sup>1</sup>
	2 $\text{Li}_{\sim 2.0}\text{Si} \rightarrow \text{a-Li}_{\sim 3.5}\text{Si}$	0.10 V
	3 $\text{a-Li}_{3.75} \rightarrow \text{c-Li}_{3.75}\text{Si}$	0.05 V
$\geq 2^{\text{nd}}$ cycle de-lithiation	1 $\text{a-Li}_{\sim 3.5}\text{Si} \rightarrow \text{a-Li}_{\sim 2.0}\text{Si}$	0.27 V
	2 $\text{a-Li}_{\sim 2.0}\text{Si} \rightarrow \text{a-Si}$	0.50 V

As the anode is lithiated and subsequently de-lithiated, the material expands and contracts to an extent where the result could be pulverization of the particles, loss of electrical contact with the conductive additive or even complete peeling off from the current collector. To illustrate the extent of this problem, the volume change mechanism will be explored. Assuming that the active material transforms from pure elemental silicon to a fully lithiated  $\text{Li}_{15}\text{Si}_4$ -phase during charging, and the number of silicon atoms is constant, the relative volume increase can be represented by the volume of one silicon atom in each end of the reaction (phase):

$$V_{\text{Si atom}} = \frac{V_c}{N_{\text{Si}}}$$

where  $V_c$  is the volume of one unit cell and  $N_{\text{Si}}$  is the number of silicon atoms per unit cell. The volume of one silicon atom in phase 1, pure crystalline silicon, can be found by

<sup>1</sup>Broad, and possibly two distinct processes.

assuming that it is in the cubic diamond crystal structure with a lattice parameter of 5.43 Ångström (Å), where each unit cell hold 8 Si atoms:

$$V_{\text{Si atom}} = \frac{(5.43\text{Å})^3}{8 \text{ Si atoms}} = 20.01 \frac{\text{Å}^3}{\text{Si atom}}$$

The volume of one Si atom in phase 2, pure  $\text{Li}_{15}\text{Si}_4$  is a bit more complex, but was found by Obrovac and Christensen [39] in a Rietvald refinement, and fit to a  $\text{Cu}_{15}\text{Si}_4$ -phase [43]. It was there shown to be a body centered cubic unit cell containing 4 formula units (space group  $I\bar{4}3d$ ). The lattice parameter for this unit cell was found to be 10.68 Å, so the volume of one silicon atom is:

$$V_{\text{Si atom}} = \frac{(10.68\text{Å})^3}{4 \times 4 \text{ Si atoms}} = 76.14 \frac{\text{Å}^3}{\text{Si atom}}$$

giving, in an idealized case, a volume increase of than 280% for an electrode going from its initial state to a fully lithiated state.

It was seen by McDowell et al. [44] that two different lithiation mechanisms were present for amorphous and crystalline Si material, and the two are illustrated in Figure 2.6. Both are characterized by a two-phase reaction, but important differences lie in the volume expansion. Amorphous silicon expands isotropically, leading to a lower concentration of Li in the lithiated phase. Crystalline silicon undergoes anisotropic expansion, leading to a faceted Si core and a nearly fully lithiated phase. Additionally it was observed that the lithiation of amorphous silicon occurs gradually, while the reaction front was significantly slower in crystalline Si and occurs in steps.

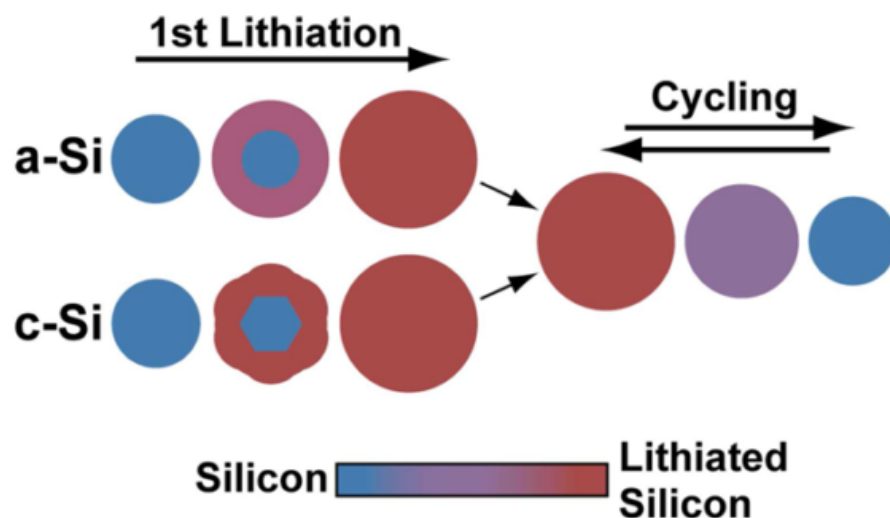


**Figure 2.6:** An illustration of the lithiation mechanism in amorphous and crystalline silicon, showing the first lithiation as a two-phase reaction. Illustration originally appears in [44].

### 2.2.1.2 Morphology change of electrode

This volume expansion is not constant throughout the electrode, causing an even higher degree of stress than the volume expansion itself. A concentration gradient will form from the current collector to the surface of the electrode due to a gradient of  $\text{Li}^+$ -ions in the electrolyte as well as restricted diffusion of  $\text{Li}^+$ -ions into the silicon anode, leading to higher lithiation of particles close to the electrolyte. As the concentration gradient is closely associated to the degree of expansion, this uneven lithiation throughout the electrode will lead to shear stress at the interface between the electrode and current collector, potentially causing delamination.

The de-lamination of active material from the current collector will cause these areas to lose electrical contact and eventually become de-activated. This breakdown of the conductive network has been confirmed by internal resistance measurements, where a sharp increase in resistance was seen at 0.4 V during de-lithiation [45]. The de-lithiation was not completed due to  $\text{Li}^+$ -ions entrapped in the silicon structure, leading to the irreversible capacity loss often seen during the first cycle. Another interesting observation by Ryu et al. [45] was done by closely examining the charge and preceding discharge capacity. As their capacities were found to be quite similar, the majority of capacity loss and Si degradation is assumed to occur during de-lithiation. This assumption was also confirmed by an atomic force microscopy (AFM) study done on the anode surface by Beaulieu et al. [32].

### 2.2.1.3 Unstable SEI

SEI formation in alloy anodes is a dynamic process, and the SEI is constantly breaking off and reformed. Continued volume change due to expansion and contraction will lead to both tensile and compressive stress in the Si particles, and cracking is more often observed due to the tensile stress of contraction during de-lithiation of the anode than of expansion. Cracking will lead to newly exposed silicon material, and re-formation of the SEI. This will in turn consume unnecessary amounts of electrolyte and  $\text{Li}^+$ -ions, increase the impedance, deactivate parts of the material and in turn contribute to capacity fade of the battery. Many studies have been done on the composition, morphology, formation and growth mechanisms of SEI films on silicon anodes, and the overall conclusion is that the SEI must be controlled so that it remains a stable passivation layer on the outer surface of the particles. A smooth particle surface is often a prerequisite for a stable SEI.

## 2.3 Overcoming challenges of alloying anodes

In order to make use of silicon and benefit from its high uptake of lithium, the battery research community has many hurdles to overcome. It is necessary to solve the issues regarding volume change, low conductivity and unstable SEI to ensure a long lifetime of the LIB, and for future commercialization. It has been seen that the surface structure of electrode materials plays a large role for their electrochemical performance, and poor lifetimes are mainly due to side-reactions occurring at the electrode-electrolyte interface. By manipulating the surface chemistry and possibly coating the particles with a protective layer before SEI is allowed to form, the activation energy of such decomposition reactions on the surface can be increased, and therefore the reactions limited [46].

As silicon works outside the stability range of most organic electrolytes, the solvents present in the electrolyte will also effect the decomposition and formation of the SEI-layer. Some specific carbonates have been found to improve the chemical properties of the SEI-layer formed on the silicon particles, and in 2015 Xu et al. [47] discovered that by introducing fluoroethylene carbonate (FEC) in the electrolyte, a thin and conformal SEI layer would form at a higher onset potential than for the remaining carbonates. This leads to a stable SEI, which protects the surface of the active material from oxidation, as well as restricting other side reactions depleting the electrolyte of  $\text{Li}^+$ -ions [47, 48].

### 2.3.1 Silicon nanoparticles from a Free Space Reactor

The upcoming section on silicon nanoparticles (SiNPs) produced at IFE is based on an article written by Andersen et al. [49], researchers at IFE. Very pure silicon nanoparticles (SiNPs) (>99.99%) were produced in the Free Space Reactor (FSR) by thermal decomposition of silane ( $\text{SiH}_4$ ) gas. As suggested by the name, the growth and nucleation happen homogeneously - thus in free space. Silane is fed into a heated tube, and the heat decomposes  $\text{SiH}_4$  into powder collected at the bottom of the reactor, as well as hydrogen ( $\text{H}_2$ ) which is filtered out. See Figure 2.7 for a schematic of the reactor. Silane decomposes through a route of several higher order silanes before turning into elemental Si, and different heating zones may be manipulated to favor a certain particle formation. The silane concentration and pressure determine the number of Si-Si collisions, and high temperatures promote the reaction speed as well as the probability of collision.

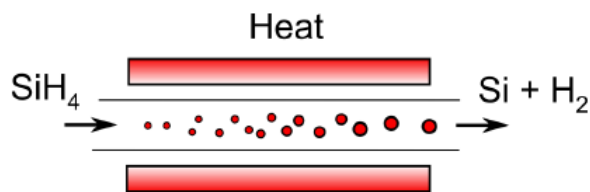


**Figure 2.7:** Schematic FSR process from Andersen et al. [49].

The nucleation and growth of SiNPs in the FSR is done by gradually removing hydrogen from the silane and by Si-Si bond formation, as can be seen in Figure 2.8. The distribution of hydrogen will be dependent on the rate of hydrogen removal compared to the rate of particle growth. If the growth rate exceeds the removal rate, hydrogen will be trapped in the lattice.

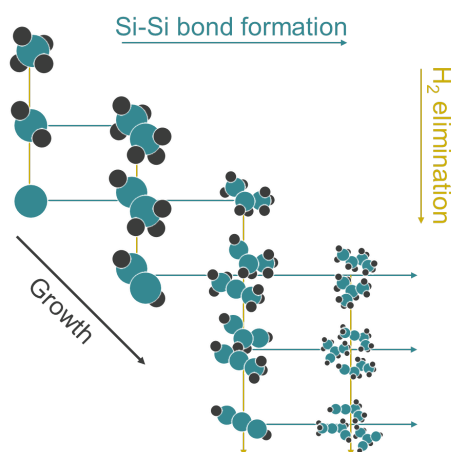


**Figure 2.8:** Growing silicon particles in the FSR reactor. Illustration by Thomas J. Preston.

### 2.3.2 Coating

Surface coating is a feasible way to take advantage of silicon, as it may protect the active material from direct contact with the electrolyte. The coating layer must be mechanically stable, electrically conductive, as well as provide a pathway for  $\text{Li}^+$ -ions to diffuse from the electrolyte into the active particles. A coating layer providing these features will lead to a large improvement in cycle life, rate capability, reversible capacity and irreversible capacity loss [7, 50–52].

#### Motivation for carbon coating

Carbon has been extensively studied as a coating material for anodes, due to its high electronic conductivity (1.25-2,000 S/m for amorphous carbon) and improvement of the

electrodes' surface compatibility with the electrolyte. The most important superiority of carbon lies in it being an excellent current collector, and will therefore decrease the internal resistance of the electrode [50]. A carbon coating may also effectively decrease sintering of Si particles during cycling. Note: As the anode material in this thesis comes in powder form, the practical electrode will be a composite containing the active material, conductive additives (CA, e.g. graphite and carbon black) and a polymer binder. The total resistance of the cell will be affected by all of these, but only the resistivity of the active material and its coatings will be discussed in the following section.

By looking at the power ability of a battery ( $P = U \times I$ , where  $U$  is the cell voltage and  $I$  is current density), it can be understood that the internal resistance should be minimized to achieve high power. Higher resistance will lead to a faster decline of the cell voltage at high current density due to the ohmic drop<sup>1</sup>, and an accelerated degradation of the battery life due to ohmic heating,  $Q = I \times R^2$ . The conductive additives added in the electrode will to some extent increase the conductivity, but as illustrated in Figure 2.9, these small conductive particles will only be "point-contacted" to the active material, and both ionic and electronic diffusion will be limited to these point contacts. Complete carbon-coating of SiNPs will create a pathway for electrons leading to a better rate performance.

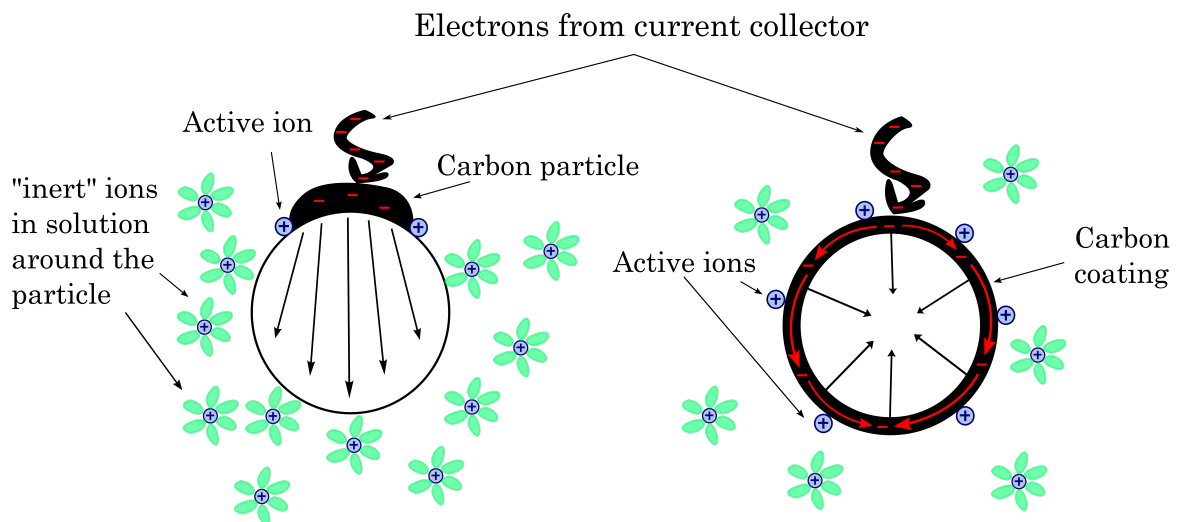


**Figure 2.9:** Schematic of the influence of (a) a carbon point contact versus (b) a homogeneous carbon coating. With a homogeneous coating, the electrons are easily transported over the entire surface of the particle and made available for the ions from the electrolyte. Illustration adapted from [50].

<sup>1</sup>The electrical potential difference between the two ends of a conducting phase during current flow.

### 2.3.2.1 Carbon coating techniques

Carbon coating may be done by several different techniques, which all have their drawbacks and advantages [50]. The simplest (and of lowest cost) method uses dry or wet mixing by ball milling or grinding, where the carbon precursor is distributed amongst the active material, and may not actually uniformly coat the surface. This technique may also involve a heating step to carbonize the precursor (thermal decomposition). A more energy consuming and expensive route is by chemical or thermal vapor decomposition involving inert gas flows and high temperatures, but in turn provides a uniform and homogeneous coating of high conductivity. A middle way is to add carbon precursors in a synthesis procedure, followed by a post-carbonization by pyrolysis. This provides higher flexibility in temperatures, core-materials and carbon sources, but the synthesis routes are normally complex, time-consuming and sensitive. The last method is used in this thesis, and is described in detail in Section 2.3.4.2.

#### Dry/wet mixing with carbon precursor

The dry or wet mixing with a carbon precursor is a quite simple method, and has been demonstrated for a variety of precursors and on many different types of structures. In Wagner et al. [53],  $\text{Li}_2\text{MnSiO}_4$  (LMS) cathode material was wet mixed in ethanol with 0 - 50 wt% of corn starch as carbon source, mortared till dryness and heat treated for 10 h at 700 °C in either Ar or 95% Ar and 5% H. Increased corn starch precursor gave a larger surface area due to a porous structure, and especially an increased microporous area at corn starch contents  $\geq 25$  wt%. A transmission electron microscopy (TEM) micrograph of the resultant coating can be seen in Figure 2.10(a). Best electrochemical results were seen for coin-cells with powder synthesized from 25 wt% corn-starch, giving 8 wt% residual carbon, where a capacity fade was seen over the first 15 cycles, from 100 mAh/g to 80 mAh/g at C/4 first five cycles, C/33 next five cycles and C/4 last five cycles. An irreversible capacity loss of 30% was also seen, expected to be from decomposition of the electrolyte, as well as partly irreversible extraction of  $\text{Li}^+$ -ions.

The use of sucrose has also been demonstrated as a carbon precursor, and the mixture of  $\text{LiNi}_{0.5}\text{Mn}_{0.5}\text{O}_2$  (another cathode material) and 5 wt% sucrose in an agate mortar for more than 2 h, with a subsequent heat treatment for 30 minutes at 600 °C in air, gave a carbon coating of 10-12 nm [54]. This coating can be also seen in a TEM, as shown in Figure 2.10(b). Electrochemical testing at a C/15 rate showed a capacity retention of 92% at the 50th cycle vs. 75% after the 30th cycle for uncoated material.

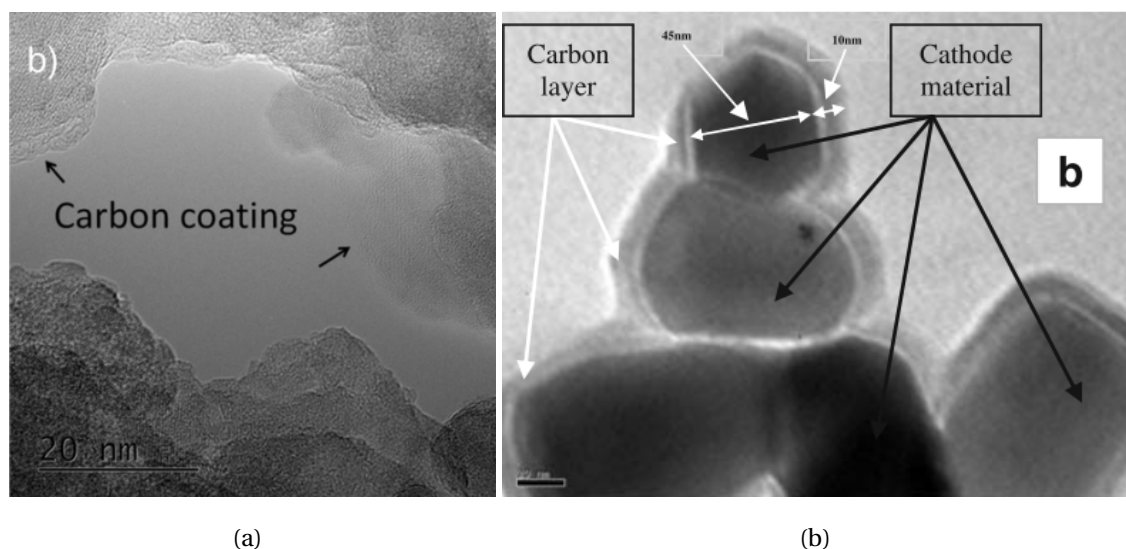


**Figure 2.10:** TEM micrographs of resultant carbon coatings from (a) wet mixing of  $\text{Li}_2\text{MnSiO}_4$  and starch from [53] and (b) dry mixing of  $\text{LiNi}_{0.5}\text{Mn}_{0.5}\text{O}_2$  and sucrose from [54].

### Thermal or chemical vapor decomposition

Thermal and chemical vapor decomposition (TVD/CVD) are the most widely used methods to carbon coat graphite material. The method promises a homogeneous deposition of carbon, and produces a core-shell structured composite. SEI formed on graphite normally contains a large amount of pores, where electrolyte decomposition of  $\text{LiC}_6$  takes place, resulting in a thicker SEI layer and higher ICL. The SEI layer formed on coated graphite was more compact and thin, resulting in better capacity retention [55].

Carbon coating micron-sized ( $\sim 10 \mu\text{m}$ ) Si by a TVD method was done by Yoshio et al. [56], and its electrochemical performance was investigated. The coating was done in a tube furnace, where Si microparticles were exposed to a  $\text{N}_2$  stream carried with benzene vapor at  $1,000^\circ\text{C}$ . The time of exposure is not reported, but the procedure was repeated several times before the powder was ground and electrochemically tested. Unfortunately, no images of the carbon coated particles were reported for comparison. A carbon content of  $\sim 10 \text{ wt}\%$  showed a high reversible capacity of  $800 \text{ mAh/g}$ , high coulombic efficiency, compatibility with both EC and PC-based electrolytes and better thermal stability than graphite. The coating was thought to suppress high decomposition of electrolyte on the surface of Si-based electrodes, but only maintained high capacities during the first 20 cycles [57] when cycled at  $0.3 \text{ mA/mg}$ . This method is highly energy consuming due to the repeated high temperature steps.

### Wet chemical synthesis procedure

Ng et al. [58] investigated a spray-pyrolysis procedure at low temperatures (300-500°C) to uniformly carbon coat Si particles (<100 nm). The Si was mixed in a citric acid/ethanol solution via ultrasonication, and was spray-pyrolized in air. Si with 56 wt%<sup>1</sup> carbon spray-pyrolized at 400°C showed the best electrochemical performance, retaining a specific capacity of 1,120 mAh/g beyond 100 cycles, with a capacity fading of 0.4% per cycle. A TEM micrograph of a carbon coated Si particle can be seen in Figure 2.11.

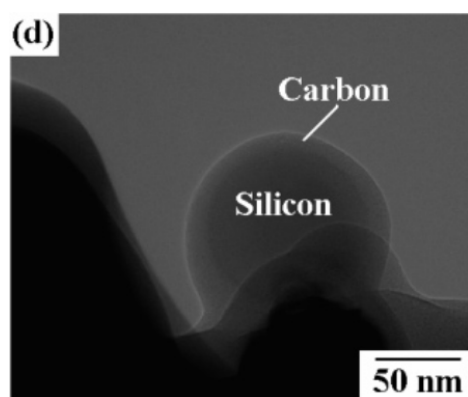


**Figure 2.11:** TEM micrograph of carbon coated Si by spray-pyrolysis in [58].

### 2.3.3 Yolk-shell particles

Research at Stanford University by the Yi Cui group has been of particular interest for the work done in this thesis, as they have studied the use of silicon particles as a base for designing multiple geometries and structures for use in LIBs [9, 15, 59–61]. Most recent and of high interest are their articles on "A yolk-shell design for stabilized and scalable Li-ion battery alloy anodes" [9] and "A pomegranate-inspired nanoscale design for large-volume-change lithium battery anodes" [15], and these two approaches have been combined and slightly simplified for the purpose of this thesis. As discussed earlier, pure silicon must be processed to be able to mechanically survive (de-)lithiation as well as produce a stable SEI. By fabricating a yolk-shell structure, the silicon would be able to expand freely within a thin carbon shell without breaking and reforming of the SEI. For this thesis, Si@SiO<sub>2</sub>@C double core-shell particles will be fabricated to serve as a starting point for fabrication of the final yolk-shell structure.

The yolk-shell structure in [9] can be seen in Figure 2.12(a), and showed a high capacity of 2,833 mAh/g<sub>Si/C</sub> at a rate of C/10 for 1,000 cycles, with a capacity retention of

<sup>1</sup>Wt% determined by mass loss between 150°C and 480°C.

74% (loading unknown), while the pomegranate microparticles in [15], seen in Figure 2.12(b), achieved a capacity retention of 97% from the 2nd to 1,000th cycle at a rate of  $C/2$  with a capacity of 1,160 mAh/g<sub>Si/C</sub> after 1,000 cycles (loading  $\sim 0.2$  mg/cm<sup>2</sup>). These long lifetimes are mainly attributed to the stable SEI layer formed on the surface of the carbon coatings, but also due to the void created for silicon expansion. Note: Core-shell particles are commonly denoted as core@shell (A@B), and yolk-shell particles as core@void@shell (A@void@B).

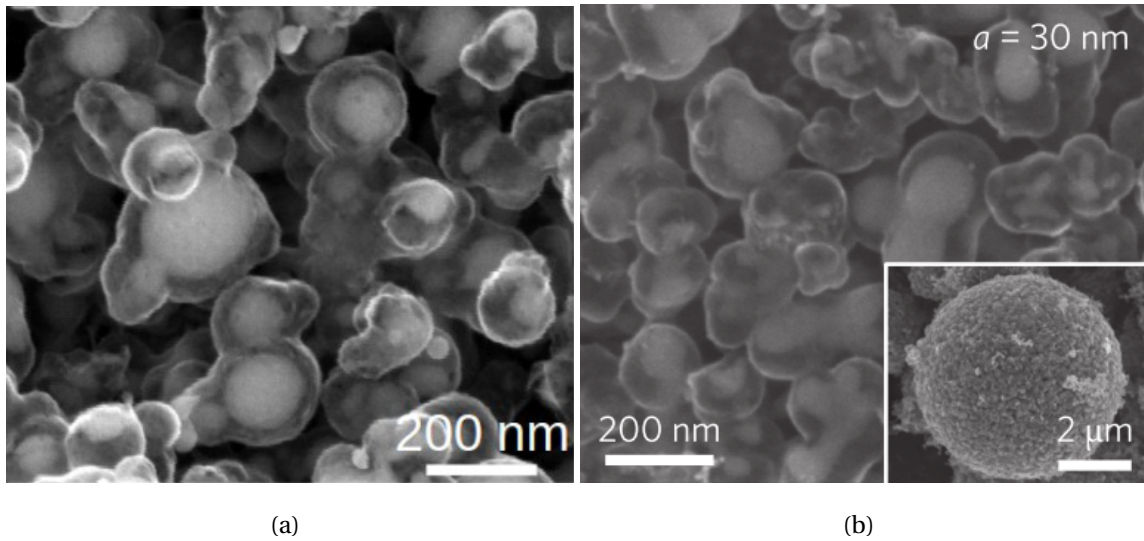


**Figure 2.12:** SEM micrographs of (a) yolk-shell structure from Liu et al. [9] and (b) pomegranate microbead yolk-shell structure from Liu et al. [15]. Void space in both was found to be  $a = 30$  nm.

To obtain Si@SiO<sub>2</sub>@C double core-shell particles from pure Si several steps are needed. First a sacrificial layer of silicon dioxide (oxide, silica, SiO<sub>2</sub>) is deposited on the surface of the particles. Even though the powders are stored in a glovebox containing an inert gas, (e.g. Nitrogen, N<sub>2</sub>), all particles have a native oxide layer from any contact with air, usually from transportation between the reactor and storing. This native oxide layer is normally very thin, around 5 nm, and for a sacrificial oxide layer this is not thick enough as it will not accommodate the volume change seen in silicon during lithiation. By calculating the radius of the particle distribution after a 300% volume increase, the ideal oxide layer thickness can be found. Assuming spherical particles with radius,  $r_1$  between 50 nm and 500 nm, the expansion will lead to particles with a radius,  $r_2$  between:

$$V_{\text{Si atom, } r_1} + V_{\text{Si atom, } r_1} \times 300\% = V_{\text{Si atom, } r_2}$$

$$\frac{4}{3}\pi r_1^3 \times 4 = \frac{4}{3}\pi r_2^3$$

$$r_2 = \sqrt[3]{4} \times r_1$$

$$79.4 \text{ nm} < r_2 < 793 \text{ nm}$$

giving an ideal oxide layer thickness,  $t$  of (for the two extremes of the size distribution):

$$29.4 \text{ nm} < t < 293 \text{ nm}$$

Clearly having such a large particle size distribution calls for a difficult coating process. This large span in oxide coating thickness is difficult to achieve when a homogeneous layer on all the particles is wanted. An oxide coating of a thickness between 50 and 100 nm is therefore chosen as a goal, to accommodate the volume change of the particles with a diameter between 180 nm and 360 nm, while still buffering some of the volume change for the rest of the particles.

After the oxide coating, a carbon containing precursor will be applied to coat the oxide surface. The most important factor to consider is the thickness of the carbon coating to ensure mechanical stability while not limiting the diffusion of lithium into the active material. A thickness of 5-10 nm was found to be sufficient to achieve the desired carbon shell [9]. When the carbon coating has been confirmed, an etching process will be needed to remove the sacrificial oxide layer. This step is not done in this thesis, but will require a low concentration HF acid, selectively etching  $\text{SiO}_2$  [62].

The superiority of the void layer created by etching of the oxide sacrificial coating with respect to simple carbon-coating was demonstrated in [63], where Si@C particles showed a more stable capacity decay than commercial  $\sim 100$  nm Si, but approached the un-coated capacity after only 50 cycles. The Si@void@C yolk-shell structure provided superior capacity retention at 800 mAh/g over the same cycles. This demonstrates the promise of the above discussed secondary structure, once carbon coating is found reproducible.

### 2.3.4 Sol-gel coating

As a common method for creating coatings on surfaces, a solution-gelation (sol-gel) synthesis can here be applied to coat the silicon nanoparticles. The sol will be formed directly on the surface of the particles that are to be coated. The sol-gel process can be divided into several general steps [64]:

1. Formation of a stable precursor solution (the sol).
2. Gelation by polycondensation reactions (the gel).
3. Aging of the sol, where the polycondensation reactions continue until the gel transforms into a solid mass. Contraction of the network and expulsion of the solvent is

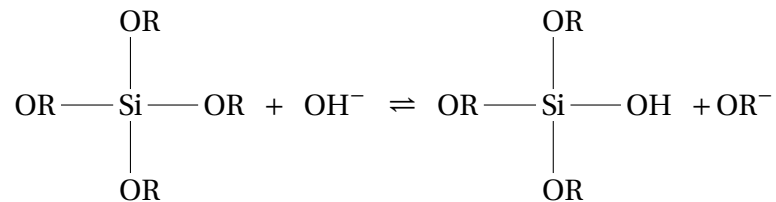
also seen.

4. Drying of the gel, where water and other volatile liquids are removed from the gel network.
5. Dehydration by calcination (can be omitted), where surface-bound M-OH groups are removed.
6. Densification of the gel at high temperatures (usually done for preparation of dense ceramics or glass).

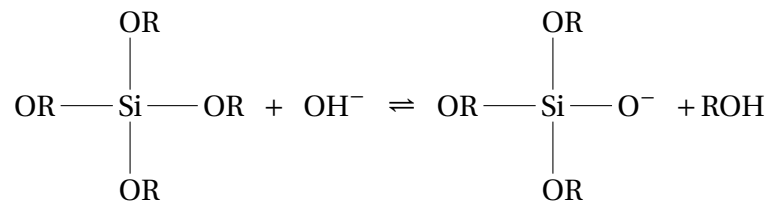
#### 2.3.4.1 Oxide coating by TEOS

Oxide coating can be applied by an extension of the Stöber method used to prepare monodisperse silica particles [65], and was presented by Liu et al. [9] for the preparation of yolk-shell particles for use in LIBs. Here the oxide is deposited as a sacrificial layer, and is to be etched away after a secondary coating by carbon.

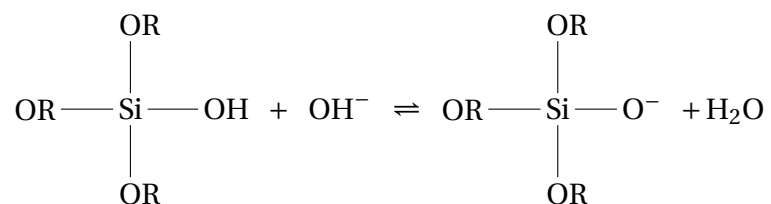
The formation of a sol starts with a precursor, here tetraethyl orthosilicate (TEOS), written  $\text{Si}(\text{OR})_4$ . The initial hydrolysis reaction occurs on the surface of the pre-fabricated SiNPs due to the presence of ammonium hydroxide ( $\text{NH}_4\text{OH}$ ) as a catalyst, and proceeds, in basic conditions, according to the following reaction:



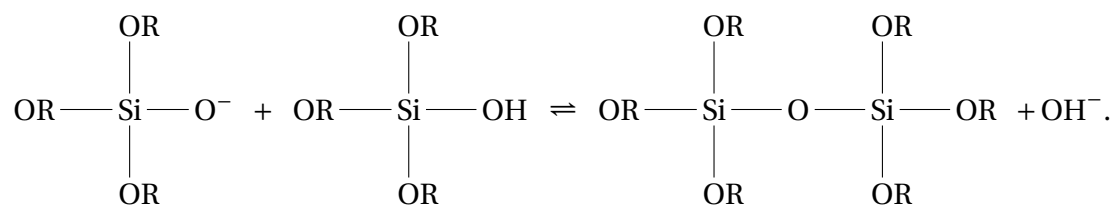
Following, and in parallel, condensation reactions occur. In basic conditions the condensation will begin with a base activating an original precursor; TEOS:



or as a reaction between a hydrolyzed molecule and the base:



both followed by a condensation reaction:



This polymerization is continued until the TEOS precursor is depleted, and the coating thickness is dependent upon added precursor as well as catalyst in the solution.

#### 2.3.4.2 Carbon coating by RF-resin

Carbon coating can be done based on a sol-gel process developed for particles, where resorcinol and formaldehyde form a crosslinked resin on the surface of oxide particles, as shown in Figure 2.13 [66]. This procedure is also an extension of the Stöber method [65], and was first presented for the formation of monodisperse resorcinol-formaldehyde (RF) polymer microspheres by Liu et al. [67]. RF resins have been found extremely interesting due to the low cost of fabrication, high surface areas and porosities, low electrical resistivity, remarkable electric conductivity, and outstanding thermal and mechanical properties [68, 69]. The phenolic resin coating grows on the surface of oxide particles by the polymerization of resorcinol and formaldehyde in a mixture of alcohol, de-ionized water (DI) and ammonium hydroxide. To successfully coat the surface, it is important to achieve good adhesion between the phenol groups and the dangling bonds at the surface of the core particle. When introducing ammonia, the reaction proceeds under basic conditions causing the oxide surface to carry a negative charge (As the isoelectric point of colloidal silica is 1.7-3.5 [70]). The phenol groups are also negatively charged under basic conditions, and an electrostatic repulsion force will inhibit the coating. By introducing a cationic surfactant, the surface will be less negatively charged and the polymerization process will be initiated. The resin is finally converted to carbon by high temperature carbonization in an inert atmosphere.

A great deal of research has been put into the study of phenolic resins, but despite the variety of micro-/mesoporous products reported, the processes have still been found difficult to control and with varying success.

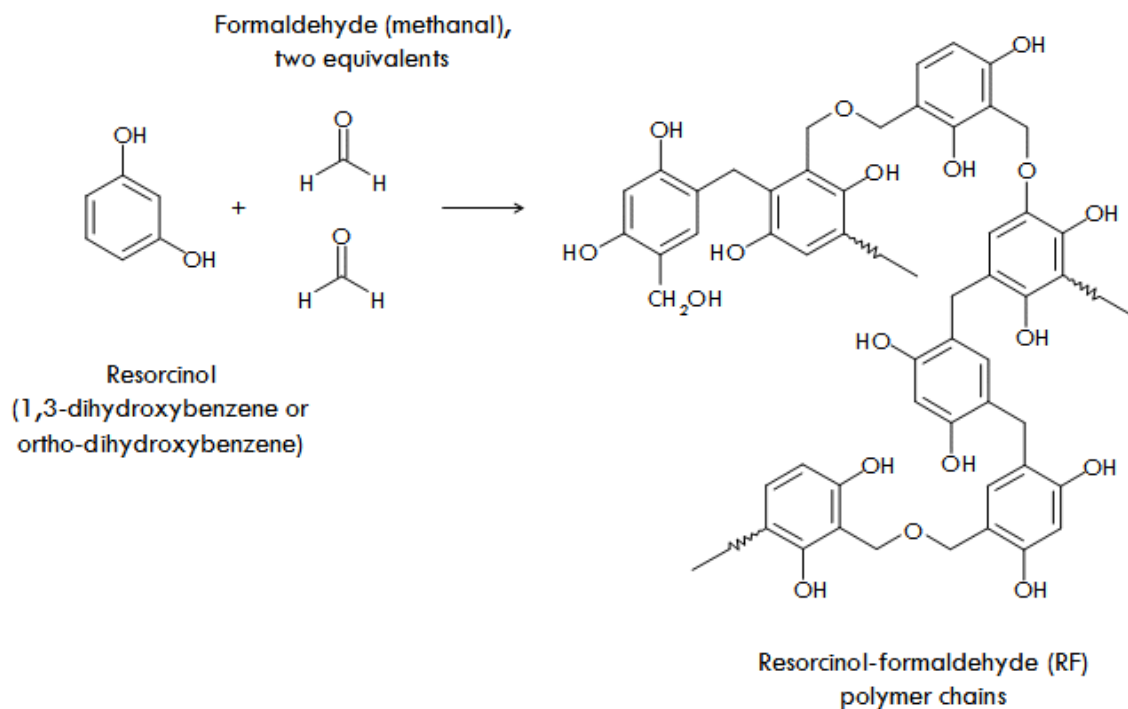


Figure 2.13: Polymerization of resorcinol and formaldehyde. Figure appears in [71].

## 2.4 Characterization techniques

This section does not give a complete overview of all the techniques used in this work, but will provide some background on techniques involving limitations and assumptions that may lead to uncertainties in the data collected, or to what extent it could be compared to other data.

### 2.4.1 Structural characterization

#### 2.4.1.1 Nitrogen adsorption

Surface area measurements are in theory quite simple. They involve the physisorption of an inert gas (e.g. nitrogen), and determines how many molecules are needed for a complete monolayer [72]. This can be done because we know that one  $N_2$  molecule occupies  $0.162 \text{ nm}^2$  at 77 K, and the total surface area can be derived from this. However, the process is complicated by factors such as multilayer adsorption, and condensation in small pores. The capillary pore condensation can give information on the type of pores and

their size distribution by the use of the Kelvin equation. By utilizing Brunauer-Emmett-Teller (BET) theory and t-plot theory, the calculated physisorption can estimate the surface area and types of pores present. Derivations behind the adsorption isotherms and Kelvin equation is beyond the scope of this work.

The use of the BET method is however limited by a few assumptions [72]:

- Rate of adsorption and desorption are equal in all layers.
- Adsorption sites are equal for all molecules in the first layer.
- The adsorption sites are constituted by the molecules adsorbed in the previous layer
- Interactions between adsorbates are ignored.
- Conditions for adsorption-desorption are the same for all layers, except the first.
- With the exception of the first layer, all adsorption energies are equal to the condensation energy.
- At saturation pressure  $P=P_0$  the multilayers may grow to infinite thickness.

T-plot theory, an extension of the BET theory, can determine the types of pores present in the material, and will distinguish between micropores ( $\leq 2$  nm), mesopores (2-50 nm) and macropores ( $\geq 50$  nm), where the two latter are often defined as the external area. This can be done by converting the amount of gas adsorbed into a statistical thickness  $t$  of adsorbed film, and comparing this to the isotherm of a porous body [73]. A t-plot can be found, and this will give the microporous (if any) surface area as the slope of the initial linear region seen below a relative pressure. Above this pressure micropores will already be filled, and only a small increase is needed for covering the remaining external surface area. An example of such a t-plot is shown in Figure 2.14, for both a uniform microporous material and when two sizes of micropores are seen.

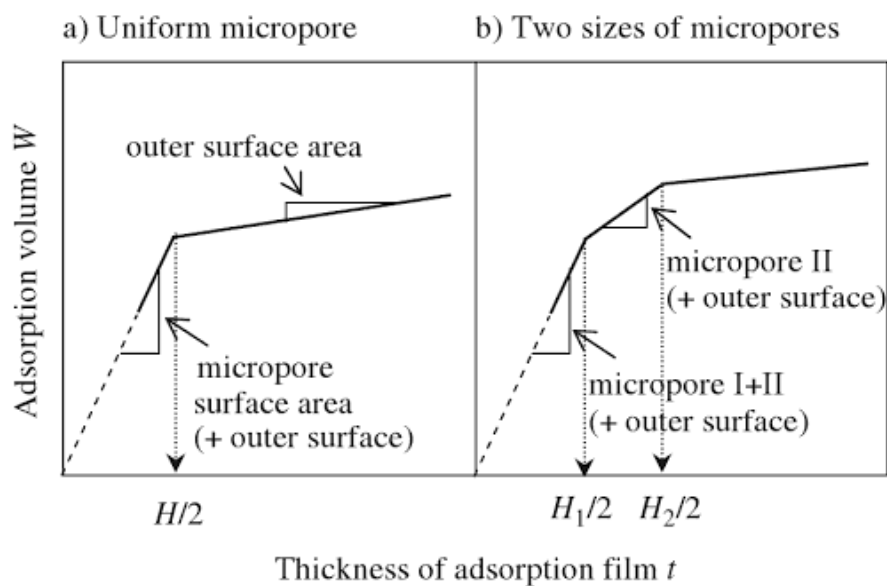


**Figure 2.14:** An illustration of how to interpret a  $t$ -plot to obtain porous surface area. Illustration originally appears in [73].

#### 2.4.1.2 Dynamic light scattering

Dynamic light scattering is often used to obtain particle size distributions (PSD), as well as observe particle aggregation and surface potential (zeta potential). Light scattering occurs by the interaction of light with the electric field surrounding a small particle, where an incident photon induces a small dipole in the electron cloud. As the particles move in solution due to Brownian motion, the dipole will change and the radiated energy is called "scattered light". This will be detected by a detector, and the particles hydrodynamic diameter can be determined by the speed of the particles. The particles speed is influenced by particle size, sample viscosity and temperature of the solution, and the measured diffusion constant can be converted into particle size using the Stokes-Einstein equation:

$$d_H = \frac{kT}{3\pi\eta D}, \quad (2.6)$$

where  $d_H$  is the hydrodynamic diameter,  $k$  is Boltzmann's constant,  $T$  is absolute temperature,  $\eta$  is the viscosity and  $D$  is the measured diffusion coefficient. The hydrodynamic diameter is defined as "the diameter of a hard sphere that diffuses at the same speed as the particle or molecule being measured" [74], and will be influenced by the surface structure of the particles as well as the type and concentration of ions in the solution.

The particles used in this work may be highly polydisperse, and of non-spherical nature.

This does pose problems when interpreting size distributions from DLS, as it will give the diameter of a sphere that has the same average translation diffusion coefficient as the particle being measured, which may vary relative to the direction of movement of the particle. An example of a non-spherical particle and its movement can be seen in Figure 2.15.

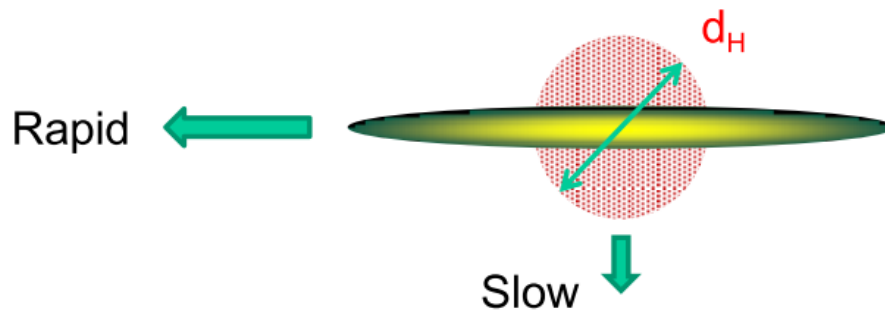


**Figure 2.15:** An illustration of a non-spherical particle subject to Brownian motion, and its corresponding DLS diameter. Illustration originally appears in [74].

By using a Zetasizer Nano from Malvern instruments, the analysis program will give a mean particle size and an estimate of the width of the distribution (polydispersity index, Pdi) based on the registered dispersant refractive index and viscosity. The value returned as the z-average diameter is intensity-weighted, and is very sensitive to the presence of aggregated or large contaminants as the intensity of light produced from the scattering is proportion to  $d^6$ , where  $d$  is the particle diameter. A polydispersity index close to 1 indicates that the distribution is so polydisperse that the sample may not be suitable for measurement by DLS.

Converting from the intensity size distribution to a number or volume distribution may further complicate the interpretation of the system, as this conversion requires a few assumptions from Mie theory [74]:

- All particles have a spherical shape
- All particles have a homogeneous and equivalent density
- Optical properties are known (refractive index and absorption)

The conversion of distributions will decrease the reliability of the peaks seen, and it is recommended to only use the volume or number PSDs for reporting relative amounts of particles found within each peak. However, as the particle sizes obtained in thesis will be compared to diameters measured by SEM analysis, the number distributions will be plotted against a histogram of particle sizes from SEM.

## 2.4.2 Electrochemical characterization

Electrochemical testing can involve a number of different techniques to evaluate the performance of new materials for battery systems. The most important electroanalytical methods used in this thesis will be described here, and the theory is based on Bard et al. [75], or Linden and Reddy [19] unless otherwise specified.

### 2.4.2.1 Important characteristics

- **Specific capacity** is the most common way to express the capacity of a cell, and is given in mAh/g. It defines the amount of electrical charge stored in an electrode per gram of active material, and 1 Ah is 3,600 coulombs. It is dependent upon all the components in the cell, and is commonly expressed as:

$$C_{cell} = \frac{1}{1/C_A + 1/C_C + 1/Q_M} \quad (2.7)$$

Where  $C_A$  is the anode capacity,  $C_C$  the cathode capacity and  $Q_M$  the rest of the cell components: electrolyte, separator, casing etc. The theoretical capacity of an active material is based on its molecular weight and the number of electrons transferred in the electrochemical process. Practical capacity however is the actual capacity measured, and is dependent on many factors such as the kinetics of the transfers, temperature, cut-off voltage and electrode designs.

- **Reversible capacity** will in this thesis (for unlimited cycling) be defined as the average capacity seen in cycles 20-50, as high capacity degradation is known to occur in the initial 10-20 cycles.

$$C_{rev} = \frac{\sum_{20}^{50} C_i}{30} \quad (2.8)$$

- **Charging rate** can be expressed in two different ways, by the specific charge current mA/g with the mass referring to the amount of active material (here Si or Si@SiO<sub>2</sub>), or be specific in terms of C-rate, which is defined as the rate at which the entire capacity of the electrode is charged or discharged in one hour. Charging/discharging during cycling is typically given as a fraction or multiple of the C-rate. For example a 1 g electrode with a specific capacity of 1000 mAh/g the C-rate is 1000 mA, and if cycled at a C-rate of C/5 the current would need to be 200 mA.
- **Irreversible capacity loss (ICL)** is the percentage capacity lost between the first

lithiation and de-lithiation. This loss is usually linked to the initial entrapment of lithium in the SEI [76, 77].

$$\text{ICL} = \left(1 - \frac{\text{De-lithiation capacity}_{1\text{st cycle}}}{\text{Lithiation capacity}_{1\text{st cycle}}}\right) \cdot 100\% \quad (2.9)$$

- **Battery lifetime** of a cell is by convention defined as the number of cycles a capacity above 80% of its initial reversible capacity is retained [78]. However, it may vary depending on what the data is to be used for and how it is compared to other cells. Lifetime is highly dependent upon cycling parameters, especially cycling rate and loading. Lifetime of cells cycled to an unlimited capacity will in this thesis be defined as the number of cycles 90% of the reversible capacity measured between cycle 20 and 50 was retained. Lifetime of cells cycled to a limited capacity will be defined as the number of cycles this capacity was retained.

### 2.4.2.2 Galvanostatic charge-discharge

Electrochemical characterization by galvanostatic charge-discharge is the most common method used to determine the performance of an electrode and the involved active material. It is a constant current method, where the potential (or charge passed through the working electrode) is measured as a function of time. The measure of charge can then be plotted against cycle number to determine lifetime, or against voltage to determine voltage profiles across cycles. This method can also determine the specific capacity and stability of load capabilities.

Usually the cycling is done at a constant current, here determined in C-rate, and during charge the voltage will decrease until a cut-off value is reached. The cut-off potential will be determined based on the potential range of the redox reactions and will limit the electrolyte decomposition, thereby also unnecessary growth of SEI. After the constant current step is done the voltage is held at the cut-off to give the  $\text{Li}^+$ -ions time to diffuse further into the active material. This constant voltage step is held until a set time is reached, or the current has met a certain fraction of its charging value.

The ratio between the charge achieved after the first lithiation-step and subsequent de-lithiation will determine the batteries irreversible capacity loss, showing how much of the  $\text{Li}^+$ -ions that are trapped in the silicon structure or in the SEI. A high capacity retention throughout the cycling shows good reversibility of the lithiation and de-lithiation processes.

Usually a low current is used for the first few cycles as part of a formation process, where the SEI layer is controllably formed. After this initial formation C-rates are normally increased and either limited capacity or unlimited capacity cycling is done. The performance of the electrode will typically decrease for higher C-rates, as the time needed for sufficient  $\text{Li}^+$ -ion diffusion is not available.

### 2.4.2.3 Differential capacity

A differential capacity ( $dQ/dV$ ) analysis can give information on things happening in the battery beyond what can be concluded from a capacity plot.  $dQ/dV$  describes the incremental capacity going into and out of a cell over a given voltage increment, and is obtained by differentiating the capacity-potential curve for each charge-discharge cycle, as is shown in Figure 2.16.

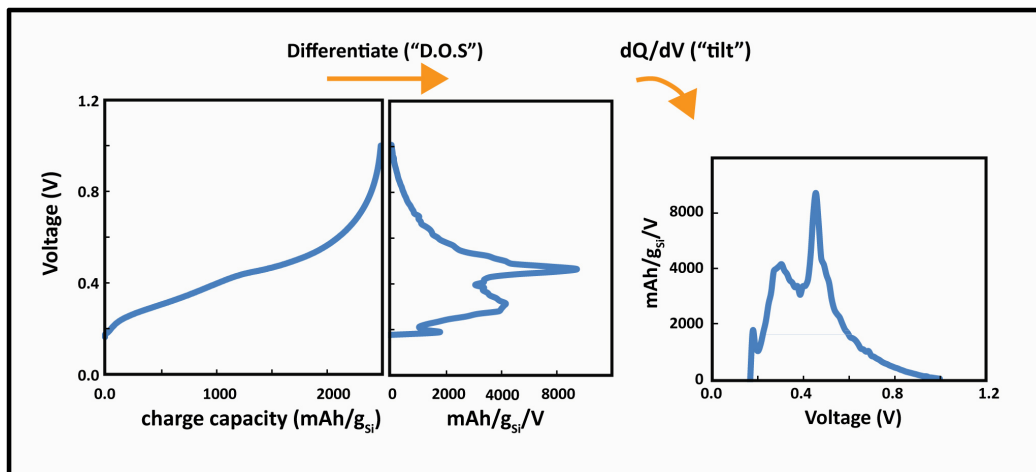


**Figure 2.16:** An illustration of how to obtain a  $dQ/dV$  plot from cycling data. Illustration by Jan Petter Mæhlen.

Plateaus in the capacity-potential curve correspond to different alloying stages between the  $\text{Li}^+$ -ions and the anode material, and changes in the slopes can be difficult to quantify by observation. The derivative of the curve however, will display these changes as peaks which are easier to understand. In intercalation materials, the peaks are typically sharp, while for Si (and other alloy materials) they are less sharp due to Si being amorphous in both its lithiated and de-lithiated state after the initial cycles. The analysis can track how the physical and chemical state of the battery changes over time, and as the battery ages, features in the curve can change in position, height and shape.

### 2.4.2.4 Electrochemical Impedance Spectroscopy

A useful tool to study the electrochemical behavior of electrode materials is electrochemical impedance spectroscopy (EIS). Here a small alternating modulation is applied to either the incoming current or voltage, and the voltage or current response is measured. The response is measured by sweeping the frequency over several orders of magnitude, can both be shifted in amplitude and phase, and a complex representation of the current and voltage is therefore convenient. The total impedance,  $Z$ , is then given as the ratio between the complex amplitude of the voltage and current modulations:  $Z = \frac{\Delta V}{\Delta I}$ .

Impedance is usually measured as a function of the frequency of the alternating current (AC) source applied. This allows for separation of the various processes contributing to the impedance, like ohmic resistances, charge transfer resistance, double layer charging and diffusion, provided that the time constants differ. An analysis of the resulting spectra is often done by the use of Nyquist plots, where the imaginary part of the impedance is plotted as a function of the real part over a wide range of frequencies. Equivalent circuits composed of elements such as resistance, capacitance, and inductance are used to qualitatively describe the material, and by fitting the Nyquist plot to this circuit numeric values can be found. An example of a Nyquist plot can be seen in Figure 2.18, with specifications to what parts correspond to the separate circuit elements.

An electrochemical cell with intercalation electrodes can often be represented by a Randles circuit, as shown in Figure 2.17, consisting of an electrolyte resistance  $R_{\Omega}$  in series with the parallel combination of a double-layer capacitance  $C_{dl}$ , and the charge transfer resistance  $R_{CT}$ , together with a diffusion element (so-called Warburg element  $Z_W$ ) [79]. The double-layer capacitance is often replaced by a constant phase element (CPE)<sup>1</sup> for interpretation of the spectrum.

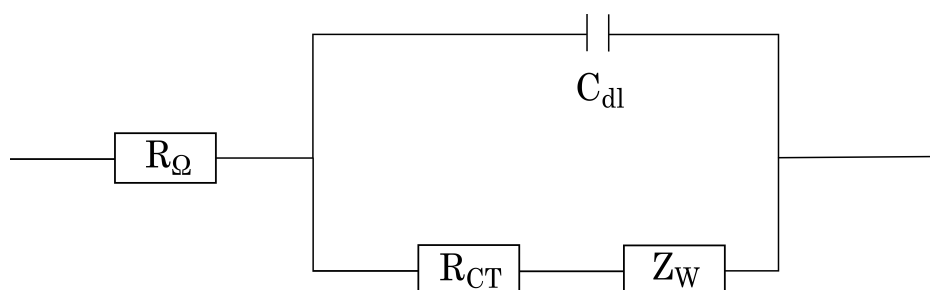


**Figure 2.17:** A Randles circuit, the simplified equivalent electrical circuit of an electrochemical cell for EIS.

<sup>1</sup>An equivalent electrical circuit component modeling the behavior of a double layer, which is an imperfect capacitor.

In the cell,  $R_{\Omega}$  is related to the resistance of the electrolyte solution. For an ionic solution with conductivity  $\kappa$ , the resistance is dependent upon the type and concentration of ions, temperature, and geometry of the area in which the current is carried. For a bound area with area,  $A$ , and length,  $l$ , carrying a uniform current, the resistance can be defined as:  $R_{\Omega} = l/(\kappa A)$ .

The double layer capacitance,  $C_{dl}$  between the electrode and its surrounding electrolyte is formed by ions in the solutions adsorbing to the surface and thereby charging it. The capacitance is then given as the ratio between the total surface charge and the applied voltage,  $C_{dl} = Q/V$ . The capacitance of this layer will be dependent on electrode potential, types and concentration of ions, oxide layers and roughness of electrode, etc.

$R_{CT}$  is the resistance to charge transfer reactions at the interphase between the electrode, SEI-layer and electrolyte. Some of the processes in the cell are time-limited, i.e. the Warburg impedance,  $Z_W$ , which is only noticeable at low frequencies due to diffusion into the bulk of the active material often being a slow process, and can be seen on a Nyquist plot as a diagonal line with a slope of 45 degrees.

For similar materials and electrolytes at the same electrode potential, we can assume that the capacitance per surface area of the material is the same, such that differences in  $C_{dl}$  may be contributed to differences in accessible surface area for the ions in the solution.

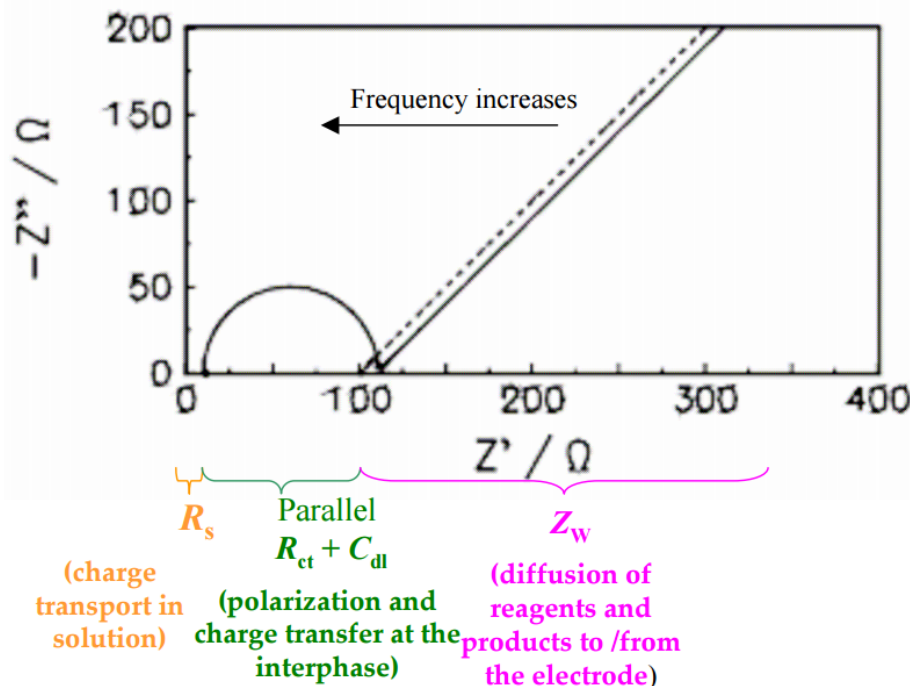


**Figure 2.18:** A model of a Nyquist plot with corresponding references to circuit elements.



# 3 Experimental

---

Double core-shell nanoparticles were prepared using pre-fabricated silicon powder from IFE. First an oxide coating was applied by a sol-gel process based on the well-known Stöber method, before a resorcinol-formaldehyde resin was applied and subsequently carbonized by pyrolysis in a tube oven and inert atmosphere. The wet chemical methods used to obtain this double core-shell structure will be presented in detail, and an overview of the experimental procedure is given in Appendix A. The powders were characterized throughout the process by several methods to assess morphology (SEM, STEM, TEM, DLS, BET), crystallinity (XRD) and chemistry (TGA). Finally the reference material was electrochemically tested to assess its behavior in half-cells. This chapter will be organized in the following order: preparation and characterization of the active material (Sections 3.1 and 3.2), slurry and electrode preparation (Section 3.3), cell assembly (Section 3.4) and electrochemical testing (Section 3.5). Fabrication of the SiNPs has been done by researchers in the Solar Department at IFE, and the remaining work has been performed by the author unless otherwise specified.

All batch processes will be referred to as the coating precursor with consecutive numbering, oxide coating by TEOS0X etc., and carbon coating by RFOX etc. Amorphous Si is preceded with an a, and crystalline with a c. Half-cells fabricated will be referred to as the nanoparticle type with consecutive numbering in parenthesis: a/c-Si ref (0X), or Si@SiO<sub>2</sub> (0X). This is to keep synthesis batches and half-cells separated when discussed.

## 3.1 Preparation of active material

### 3.1.1 Amorphous reference silicon

The FSR method has been found to create a large quantity of SiNPs, ranging from 100 nm - 5  $\mu$ m in diameter, and an amorphous batch (a-Si ref) from the FSR will here be used as the reference material and core material for double core-shell particles. The material is used as-fabricated, and stored in a glovebox containing nitrogen.

### 3.1.2 Crystalline reference silicon

Crystalline silicon (c-Si ref) was prepared in order to determine the effect of crystallinity on the initial electrochemical cycling of the silicon powder. The silicon core of the core-shell particles may crystallize during the pyrolysis-step of carbon coating, so the amorphous reference silicon was crystallized by mixing with ethanol and underwent the same heating program as used for carbonization of the carbon coating, see Figure 3.2(b) in Section 3.1.4 for more details on the heating procedure.

### 3.1.3 Sol-gel coating of oxide layer

The oxide coating was applied onto the surface of the amorphous reference silicon by a sol-gel process, using tetraethyl orthosilicate (TEOS) as precursor and ethanol as a solvent. Water was added as a reaction agent, and ammonium hydroxide solution was used to induce basic conditions and catalyze the coating process. The specific parameters for each batch can be found in Table 3.1, and the amount of TEOS precursor and ammonium hydroxide catalyst used in the oxide coating is based on values determined by Liu et al. [15]. The main difference between the silicon particles used by Liu et al. and the ones used in this thesis is their size and agglomeration, as Liu et al. used commercial ~80 nm silicon particles. An amount of TEOS giving an expected oxide coating thickness of 50-100 nm was used, where the final coating thickness will be determined by TEM micrographs.

400-800 mg of a-Si ref was dispersed in a 4:1 mixture of ethanol and de-ionized (DI) water in a 500 ml or 1,000 ml round bottom flask, and ultrasonicated in a bath from VWR (USC200T) for 25 minutes at 120 W to obtain a colloidal solution. The flask was placed on a magnetic stirring plate, where a sufficiently high rpm was chosen to ensure vigorous mixing of the solution. 1-6 ml of concentrated ammonium hydroxide (Sigma-Aldrich, >99.99% purity) and 0.8-3.2 ml TEOS (Sigma-Aldrich, 99.999% trace metals basis) was added dropwise.

The solution was left stirring overnight at room temperature (RT). After stirring for a minimum of 12 hours (to ensure sufficient polymerization and corresponding depletion of TEOS molecules in the solution), the mixture was transferred to centrifuge vials from VWR (polypropylene), and the core-shell NPs were collected by centripetal force at the bottom of the vials. Rotational speed and time was adjusted for each batch to ensure sufficient collection (4,000-6,000 rpm, 4-10 min). The clear solution of water and ethanol

was removed, and the particles were washed with DI water and a few ml of ethanol (for superior collection) three times by centrifugation.

The remaining viscous mixture (slurry) of Si@SiO<sub>2</sub> particles and DI water was poured onto a petri dish, and left on a heating plate (80-90°C) for evaporation of remaining H<sub>2</sub>O, before collection of the dried powder in a glass vial. The experimental set-up for collection of the coated NPs can be seen in Figure 3.1.

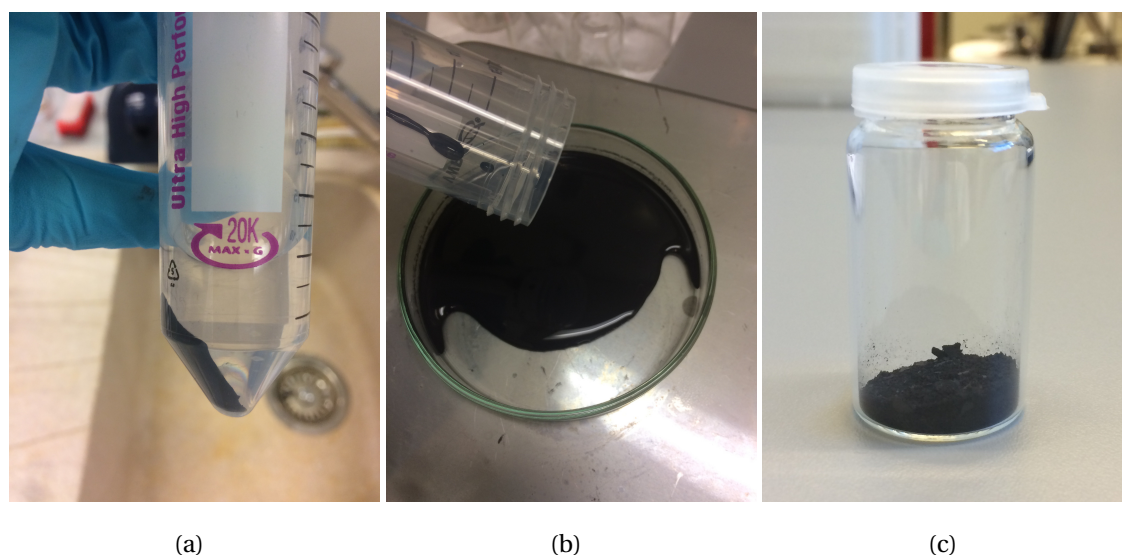


**Figure 3.1:** The experimental set-up for collection of Si@SiO<sub>2</sub>: (a) washed Si@SiO<sub>2</sub> in a centrifuge vial, (b) slurry of Si@SiO<sub>2</sub> in DI water on heating plate, and (c) dried powder in glass vial.

**Table 3.1:** Synthesis of Si@SiO<sub>2</sub> particles by addition of TEOS.

Batch	SiNP [mg]	Ethanol [ml]	H <sub>2</sub> O [ml]	NH <sub>4</sub> OH [ml]	TEOS [ml]	Yield [mg]
TEOS01	400	320	80	1	0.8	380
TEOS02	400	320	80	3	1.6	360
TEOS03	800	640	160	6	3.2	420 <sup>1</sup>
TEOS04	800	640	160	4	3.2	730
TEOS05	800	640	160	4	3.2	740
TEOS06	800	640	160	4	3.2	750
TEOS07	400	320	80	4	1.6	440
TEOS08	400	320	80	4	1.6	440 <sup>2</sup>
TEOS09	400	320	80	4	1.6	440 <sup>2</sup>

<sup>1</sup>Solution was spilled, therefore low yield.

<sup>2</sup>Used in characterization

### 3.1.4 Carbon coating of core-shell particles

The carbon coating method used is based on a resorcinol-formaldehyde resin as presented by Gan et al. [66]. Resorcinol and formaldehyde was used as precursors with DI water as the solvent. Ammonium hydroxide was added to induce basic conditions, and hexadecyltrimethylammonium bromide (CTAB) was added as a cationic surfactant in order to induce a positive surface charge. The specific parameters for each produced batch can be found in Table 3.2.

100-600 mg of the produced Si@SiO<sub>2</sub> particles was dispersed in 30 ml DI water by ultrasonication for 25 minutes at 120 W to obtain a colloidal solution. The solution was placed on a magnetic stirring plate, and 1-6 ml 10 mM CTAB (Sigma Aldrich >98%) and 0.1-0.6 ml concentrated ammonium hydroxide (Sigma-Aldrich, >99.99% purity) was added under vigorous stirring, and left for 20 minutes for complete coverage of CTAB on the surface of the particles.

Concentration of needed CTAB for complete coverage, and thereby a positive surface charge was found by electrophoretic light scattering (ELS), where zeta potential was recorded at different molarities of the added CTAB. 50 mg Si was dispersed in 15 ml DI water and ultrasonicated for 30 minutes in a glass vial. 500  $\mu$ l of CTAB with molarities between 0.1 and 40 mM was added to the vial and left under magnetic stirring for 20 minutes before measurement using a Zetasizer Nano (Malvern Instruments) to record zeta potential.

After complete coverage by CTAB, 40-360 mg resorcinol (Sigma Aldrich, ACS reagent, >99.0% ) and 56-336  $\mu$ l formaldehyde (Sigma Aldrich, ACS reagent, 37 wt.% in H<sub>2</sub>O, contains 10-15% methanol as stabilizer) was added, and the new solution was left stirring over night at RT to ensure complete polymerization of the RF-resin. The solution was then transferred to centrifugal vials, and the particles were washed three times with ethanol, where rotational speed and time was adjusted for each batch to ensure sufficient collection. The remaining mixture of RF-resin coated silicon and ethanol was placed in an alumina crucible and transferred to an oven (Brother XD-1600MT Vacuum Tube Furnace, see Figure 3.2(a) for carbonization of the RF-resin by pyrolysis. The slurry was heated at a rate of 5°C/min, and kept at 800°C for two hours under argon-flow (Ar). The heating program used for carbonization can be seen in Figure 3.2(b).

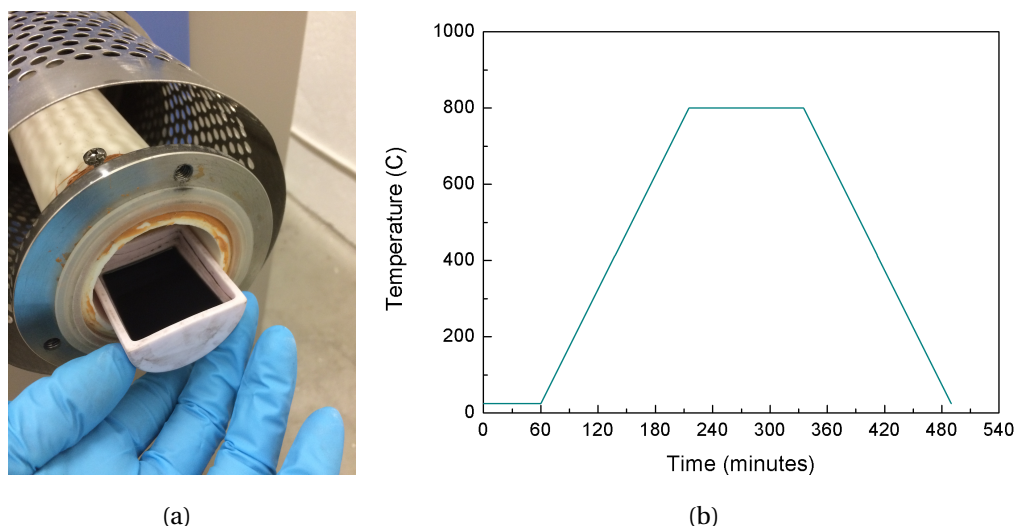


**Figure 3.2:** (a) Carbonization of slurry in alumina crucible and (b) the heating program used.

**Table 3.2:** Synthesis of Si@SiO<sub>2</sub>@C particles by RF-resin.

Batch	Si@SiO <sub>2</sub> [mg]	H <sub>2</sub> O [ml]	CTAB [ml]	NH <sub>4</sub> OH [ml]	Resorcinol [mg]	Formaldehyde [μl]	Yield [mg]
RF01	300	90	3	0.3	120	168	236
RF02	600	180	6	0.6	360	336	550
RF03	100	30	1	0.1	40	56	84
RF04	100	30	1	0.1	40	56	74
RF05	100	30	1	0.1	40	56	88

## 3.2 Characterization methods

Characterization of the reference and coated powders was done by several different methods to understand how the coatings affected their morphology, and to determine how this morphology has an effect on the electrochemical results. Dynamic Light Scattering (DLS) was done to determine the size distribution of the particles. It was done by dissolving a few milligrams of each powder in 20 ml ethanol, and ultrasonicing for 15 minutes at 120 W before a few drops was placed in a cuvette in a Zetasizer Nano (Malvern Instruments). The particle size distribution (PSD) is given in terms of intensity, but number and volume PSDs were also calculated by the software.

A field-emission scanning electron microscope (FE-SEM) was used to investigate the morphology and size distribution of the SiNPs before coating was applied, as well as

after the different coating steps. An accelerating voltage of 5-6 kilo-volts (kV), and working distances (WD) of 4-15 mm was used depending on whether or not energy dispersive x-ray spectroscopy (EDS) was done. EDS was used as an elemental analysis of the samples, but for the case of carbon coating this method is not representative due to the carbon tape used for particle adhesion onto the stub used for SEM-analysis. The carbon coating was therefore also investigated by Transmission Electron Microscopy in scanning mode ((S)TEM) and correspondingly higher resolution EDS by Asbjørn Ulvestad, PhD candidate at UiO. The TEM analysis was conducted at an acceleration voltage of 300 kV, and images were acquired using a high angle annular dark field (HAADF) detector. The FE-SEM was also used in transmission mode (S(T)EM) to investigate the coating layers. Samples were prepared for STEM by dispersing the particles in ethanol by ultrasonication for 5 minutes in order to reduce agglomeration. A drop of the dispersion was transferred to a lacey carbon TEM grid and allowed to dry in ambient atmosphere for 3 minutes. After this time, any excess dispersion was absorbed with a filter-paper before the sample was left to dry over night.

The crystallinity of the samples was determined by X-ray diffraction (XRD) analysis on a Bruker-AXS D8 Advance ( $20^{\circ}$ - $60^{\circ}$ ,  $1.33^{\circ}\text{min}^{-1}$ ,  $\text{CuK}\alpha$  source, LynxEye detector) by depositing powder onto a single crystal silicon flat plate and adding a few drops of ethanol for dispersion of the powder on the plate. The analysis was carried out from  $20^{\circ}$ - $60^{\circ}$ , and the peaks correspond to Bragg-reflections specific for different elements. XRD was in this report used to verify whether the powder at different steps was amorphous or crystalline. Sharp peaks indicate a crystalline material, while broader peaks and background signal indicate an amorphous material.

Investigations of the Brunauer-Emmett-Teller (BET) specific surface area and pore size distribution was done by nitrogen adsorption measurements (Tristar 3000 Surface Area and Porosity Analyzer at liquid nitrogen temperature,  $-195.85^{\circ}\text{C}$ ). Before the samples could be analyzed by BET, they were weighed in glass tubes, degassed overnight for eliminating any moisture, and weighed again. Nitrogen was then used as an adsorbant, and by determining the quantity adsorbed on the surface, the surface area can be calculated by t-plot theory in the software used.

Thermogravimetric Analysis (TGA) was done using a Netzsch Thermal Analysis System (STA449) to determine carbon content in the carbon coated samples, as well as to assess whether or not the ethanol used as a solvent in the crystallization process of c-Si ref had carbonized and therefore produced some carbon content in the silicon, which could be reflected in the electrochemical results. A few milligrams of powder is transferred to a

cleaned  $\text{Al}_2\text{O}_3$  crucible before the sample weight is measured, and the weight is tared. The sample is then heated up to  $1000^\circ\text{C}$  at a rate of  $10^\circ\text{C}/\text{min}$  in a gas flow of  $40\text{ ml}/\text{min}$  of synthetic air. Change in mass as a function of temperature is recorded and as the carbon will react with the air and become  $\text{CO}_2$ , its approximate wt% can be extracted.

### 3.3 Slurry and electrode preparation

In this study three types of slurries were made: (1) containing amorphous reference powder (a-Si ref) as-fabricated from the FSR, (2) crystallized reference powder (c-Si ref), and (3) oxide coated powder ( $\text{Si}@\text{SiO}_2$ ). The viscous slurries were made by mixing 15 wt% sodium carboxymethyl cellulose (Na-CMC) binder (Sigma Aldrich), potassium hydroxide (KOH) and citric acid buffer (solvent made at IFE, and added as four times the total weight of the dry components), 10 wt% graphite (Timcal, KS6L), 15 wt% carbon black (Timcal, C65) and 60 wt% silicon powder in a THINKY Planetary Centrifugal Mixer. Graphite and carbon black are added as conductive additives (CA) in the slurry. Each slurry was tape cast onto a dendritic copper (Cu) foil current collector using a doctor-blade method at both one half milli-inch and one milli-inch thickness, before being left to dry over night and subsequently treated in an Ar-oven for three hours at  $120^\circ\text{C}$  to remove remaining moisture. After heat treatment, electrode disks were cut using a Hohsen electrode punch and weighed, making sure that the loading ( $\text{mg}/\text{cm}^2$ ) of active material was as similar as possible for comparing purposes. The loading of the disks used in electrochemical cycling can be found in Table 3.3. These disks were placed in the vacuum loadlock of an Ar-filled glovebox, before they were used in the cell preparation. This procedure and the slurry recipes can be found in Appendix B.

**Table 3.3:** Masses and loading of silicon electrodes.

	Electrode	Active material [mg]	Loading [mg/cm <sup>2</sup> ]
Slurry 1	a-Si ref (01)	0.92	0.52
	a-Si ref (02)	0.93	0.53
	a-Si ref (03)	0.95	0.54
	a-Si ref (04)	0.91	0.52
	a-Si ref (05)	0.92	0.52
Slurry 2a	c-Si ref (01)	0.72	0.41
	c-Si ref (02)	0.71	0.40
	c-Si ref (03)	0.70	0.40
	c-Si ref (04)	0.71	0.40
Slurry 2b	c-Si ref (05)	0.90	0.51
	c-Si ref (06)	0.90	0.51
	c-Si ref (07)	0.91	0.51
	c-Si ref (08)	0.90	0.51
Slurry 3	Si@SiO <sub>2</sub> (01)	0.86	0.49
	Si@SiO <sub>2</sub> (02)	0.80	0.45
	Si@SiO <sub>2</sub> (03)	0.89	0.50
	Si@SiO <sub>2</sub> (04)	0.88	0.50

### 3.4 Cell assembly

Half-cells were used in this study, as only the working electrode is to be studied, and the counter reference electrode is therefore composed of metallic lithium. For the preparation of half-cells, stainless steel CR2032 cells from Hohsen Corp. were assembled in an Ar-filled glove box from MBraun with less than 0.1 ppm O<sub>2</sub> and H<sub>2</sub>O. The cell schematic can be seen in Figure 3.3(a). The electrode disks were placed with the Cu-foil down into the bottom case of a coin cell. 20  $\mu$ l electrolyte with 1 M LiPF<sub>6</sub> in 1:1:3 EC/PC/DMC, 1% VC and 5% FEC (G1 from BASF) was added, followed by an 18 mm Celgard separator (2045 polypropylene, 20  $\mu$ m thick), making sure the electrode was centered underneath. Another 15  $\mu$ l electrolyte was added to fully soak the separator and electrode, before the gasket was placed into the coin cell can. A Li-metal disk was carefully scraped free of oxides using a scalpel and placed into the can, before a stainless steel spacer and washer spring were placed on top, taking up any additional space inside the cell, and making sure that all parts are in good contact. The cap was closed over the case, and the cells

were sealed in a crimping machine after preparation.

Three-electrode cells for EIS were prepared in PAT-cells, and the cell schematic can be seen in Figure 3.3(b). Here the same electrodes are used (Si anode and Li counter electrode), but the separator is a 260  $\mu\text{m}$  thick glass fiber separator from EL-CELL containing a ring of lithium. This lithium serves as a reference electrode, and an excess amount of electrolyte was added to completely soak the separator, approximately 100  $\mu\text{l}$ .

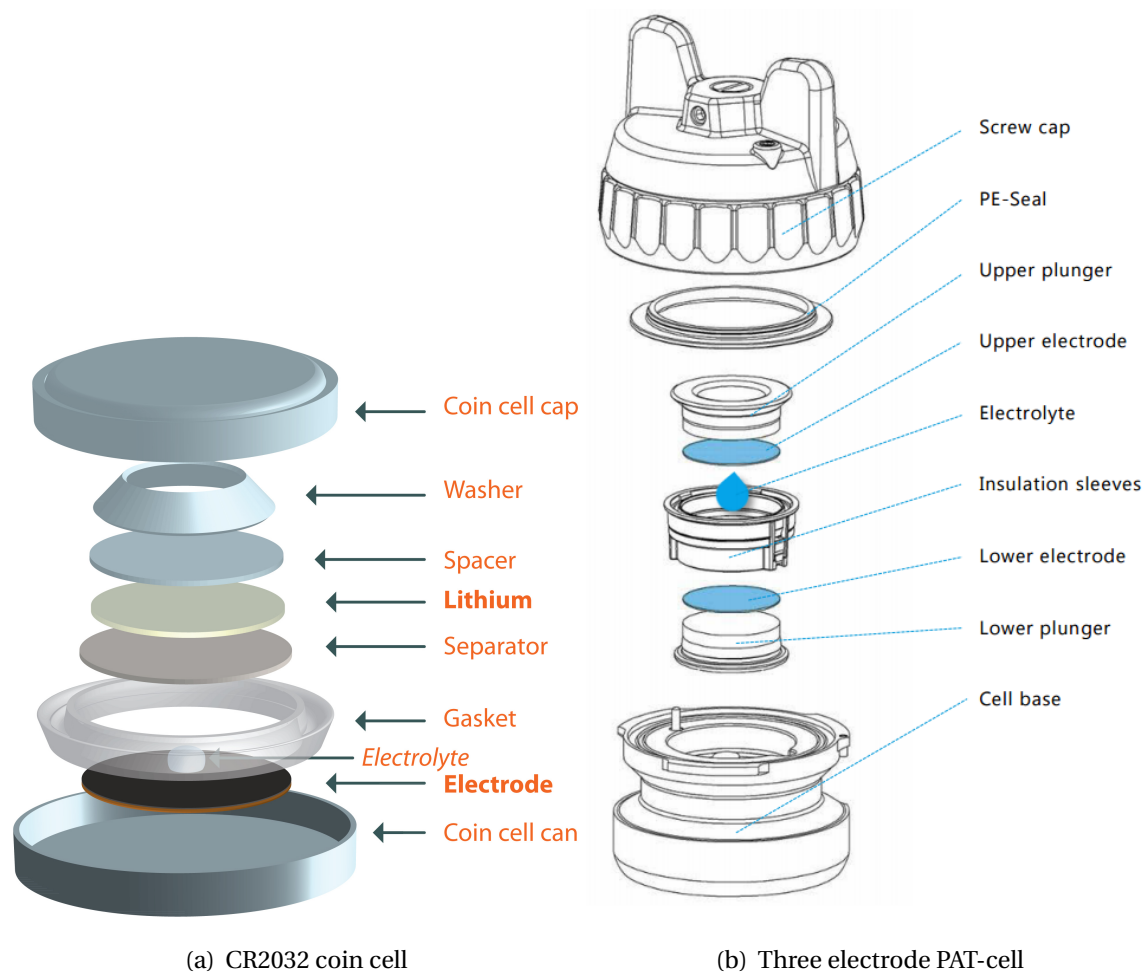


**Figure 3.3:** Schematics of CR2032 coin cell and PAT-cell for half-cell electrochemical testing and electrochemical impedance spectroscopy. Illustration (a) made by Jan Petter Mæhlen, and (b) from EL-CELL website.

### 3.5 Electrochemical testing

A computer-controlled multichannel battery tester (Arbin) was used for galvanostatic cycling of the cells, where  $dQ/dV$  and voltage plots were extracted from the cycling. A potentiostat from BioLogic was used to cycle and run EIS on three-electrode cells. Charge

and discharge rates are given as C-rates, all capacities plotted are after lithiation of silicon, and all capacities are given per gram of active material (either Si or Si@SiO<sub>2</sub>).

Note: The Arbin tester has been found to deliver unstable results in the current range used for most coin cells. These instabilities lead to coulombic efficiency values above 100%, which is not realistic as this would mean more lithium is taken out of the structure than was inserted during lithiation. Coulombic efficiency has for this reason not been plotted in this thesis, as the results would not contribute to a higher understanding of the systems tested. These instabilities will also affect the ICL reported for the first cycle, but the ICL values will still be discussed in spite of the insecurities from Arbin. A calibration of the tester was performed in March 2017 due to the unstable values, without large improvements in the reported values. The amorphous Si cells were cycled before the calibration found place, while the crystalline Si cells were cycled after the calibration. The comparisons will therefore be done with caution.

### 3.5.1 Galvanostatic charge-discharge

Galvanostatic charge and discharge cycling was performed to determine capacities and cycling stability of the batteries. Table 3.4 shows which half-cells were subject to what program, and at least two cells of each material are tested for reproducibility. The detailed programs used for galvanostatic cycling at both unlimited and limited capacities can be found in Appendix C.

Two cells of each material were cycled using the same programs for determining (i) how many cycles a limited capacity of 1,200 mAh/g could be retained at a C-rate of C/5 between 50 mV and 1 V, or (ii) cycled to an unlimited capacity at a C-rate of C/5 between 50 mV and 1 V. One cell (a-Si ref (05)) cycled in Skare [1] is also included in the table, and was cycled at a limited capacity of 720 mAh/g at C/10 between 50 mV and 1.2 V.

**Table 3.4:** Galvanostatic charge-discharge cycling, overview of half-cells and programs.

Cycling program	Cells
Unlimited capacity at C/5	a-Si ref (01) & (02)
	c-Si ref (01), (02), (05) & (06)
	Si@SiO <sub>2</sub> (01) & (02)
Limited capacity to 1,200 mAh/g at C/5	a-Si ref (03) & (04)
	c-Si ref (03), (04), (07) & (08)
	Si@SiO <sub>2</sub> (03) & (04)
Limited capacity to 720 mAh/g at C/10	a-Si ref (05)

Differential capacity curves,  $dQ/dV$  were derived by a Python script developed by researcher Jan Petter Mæhlen at IFE, and the obtained values were plotted against voltage, where one loop corresponds to one charge-discharge cycle. The internal resistance of each cell is measured after each charge by a current interrupt pulse, and plotted against cycle number.

### 3.5.2 Electrochemical Impedance Spectroscopy

Electrochemical Impedance was measured by cycling three-electrode cells using a Biologic Potentiostat. Two cells of each material were tested for reproducibility, and the detailed programs can be found in Appendix C.3. The cells were completely lithiated and de-lithiated twice for formation purposes, before a Galvanostatic EIS (GEIS) measurement was done with an AC frequency swept from 10 mHz to 100 kHz. GEIS was measured at 50% state of charge (SOC) and in a 100% lithiated state. The cell is expected to be at 50% SOC after lithiation at a C/5 rate for 2.5 h, and at 100% after lithiation for another 2.5 h. The results are plotted in Nyquist plots, and impedance values for the cell can be extracted by fitting an equivalent circuit to this plot.



## 4 Results

---

The results will be presented following the coating procedures, and will highlight problems along the way as well as confirming what led to successful coatings. Structural characterization by SEM/STEM/TEM micrographs, DLS, XRD analysis, nitrogen adsorption measurements (BET) and thermogravimetric analysis (TGA) will be presented where relevant, before the electrochemical performance of the powders will be shown by galvanostatic charge-discharge capacities, differential capacity plots (dQ/dV) and electrochemical impedance spectroscopy (EIS). The amount of carbon-coated material synthesized was insufficient for fabrication of electrodes, and the material was therefore not characterized electrochemically.

### 4.1 Pure silicon as reference

First the reference material produced in an FSR will be characterized by morphology and crystallinity, before electrochemical results will be presented. The reference material was initially found to be amorphous, but a crystallized version was also prepared and electrochemically tested.

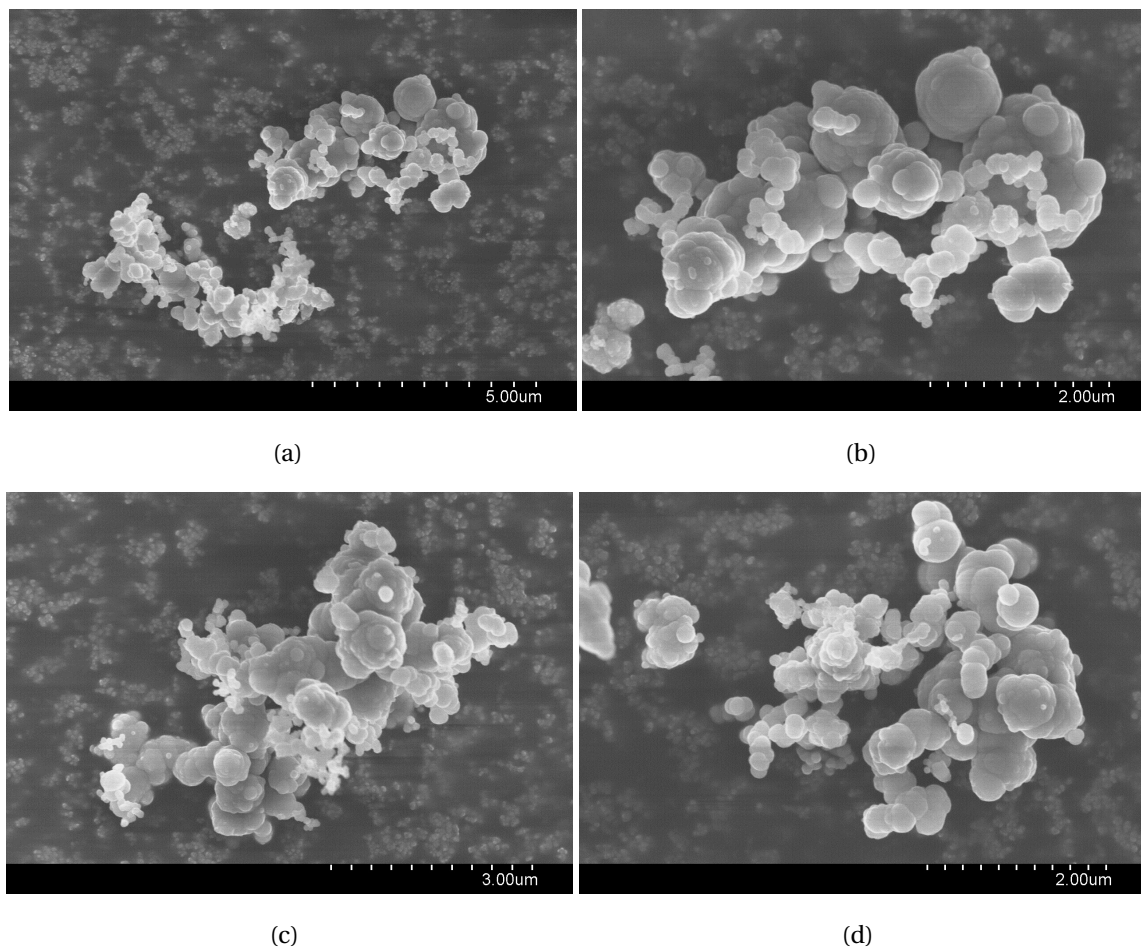
#### 4.1.1 Structural characterization

##### 4.1.1.1 Morphology

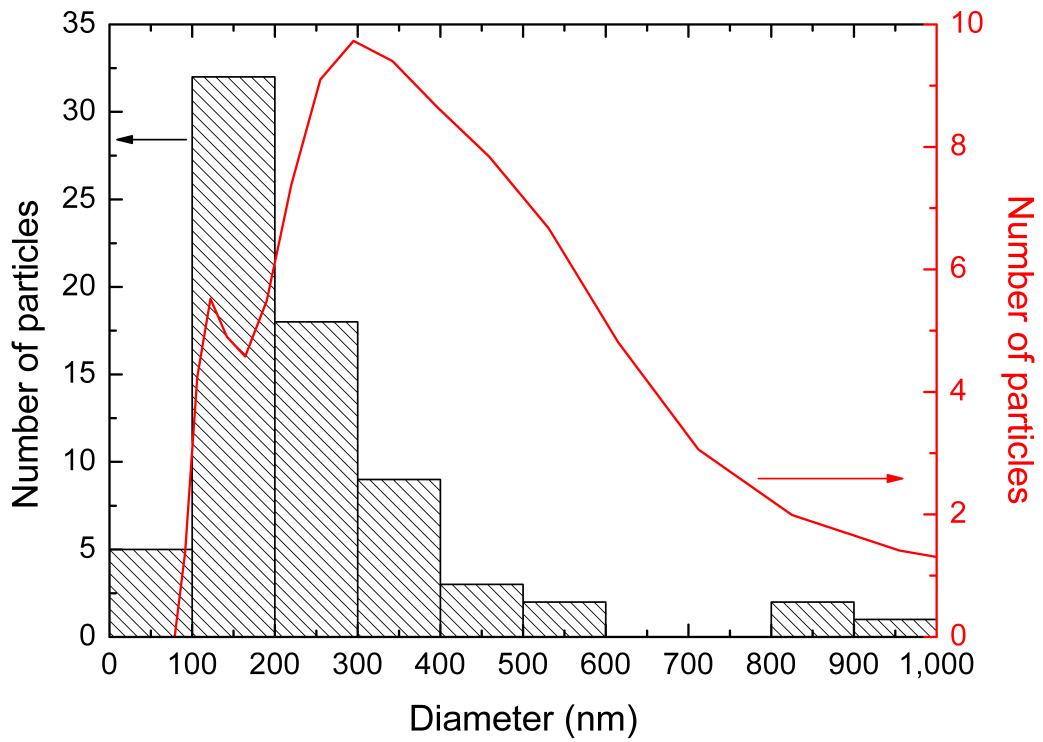
SEM micrographs of the amorphous reference silicon powder (a-Si ref) can be seen in Figures 4.1 and 4.3, and consists of quite polydisperse and agglomerated silicon nanoparticles of varying spherical shapes. The majority of the size distribution was calculated by ImageJ software to be between 50 nm and 1  $\mu\text{m}$ , where many of the particles are merged together to form larger secondary particles without a clear spherical shape. The particle size distribution from particle size analysis in ImageJ is shown in Figure 4.2, along with the size distribution by hydrodynamic diameter from DLS. The difference between the two distributions may be attributed to the hydrodynamic assumption in DLS, as well as agglomeration. Some larger chunks of silicon were also seen in the SEM, and some examples of these are shown in Figure 4.6.

After crystallization the particles did not change significantly, and the same polydisperse, agglomerated silicon was seen. SEM micrographs of the crystalline reference silicon powder (c-Si ref) is shown in Figure 4.4, while the particle size distribution from particle size analysis in ImageJ and hydrodynamic diameter from DLS is shown in Figure 4.5. C-Si ref shows a shift in the distribution to larger diameters.

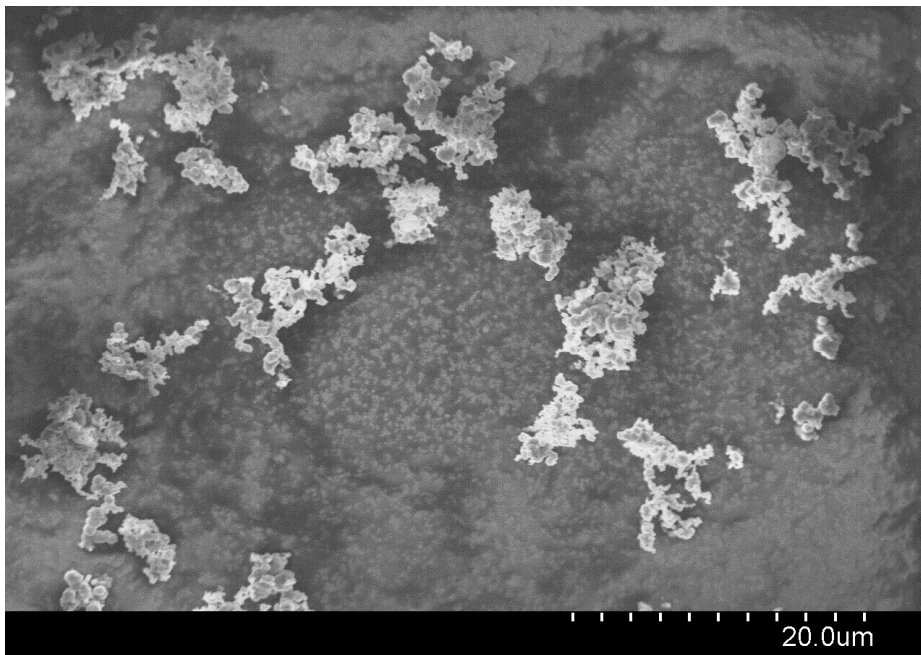
Surface area measurements from BET analysis are shown in Figure 4.7 and Table 4.1, and show only slight differences between the amorphous and crystalline silicon. The BET surface area was found to be  $3.10 \text{ m}^2/\text{g}$  and  $3.93 \text{ m}^2/\text{g}$ , respectively. A small micropore area (pores with diameters  $\leq 2 \text{ nm}$ ) of  $0.19 \text{ m}^2/\text{g}$  was seen in the crystalline silicon, while no micropore area was found in the amorphous powder.



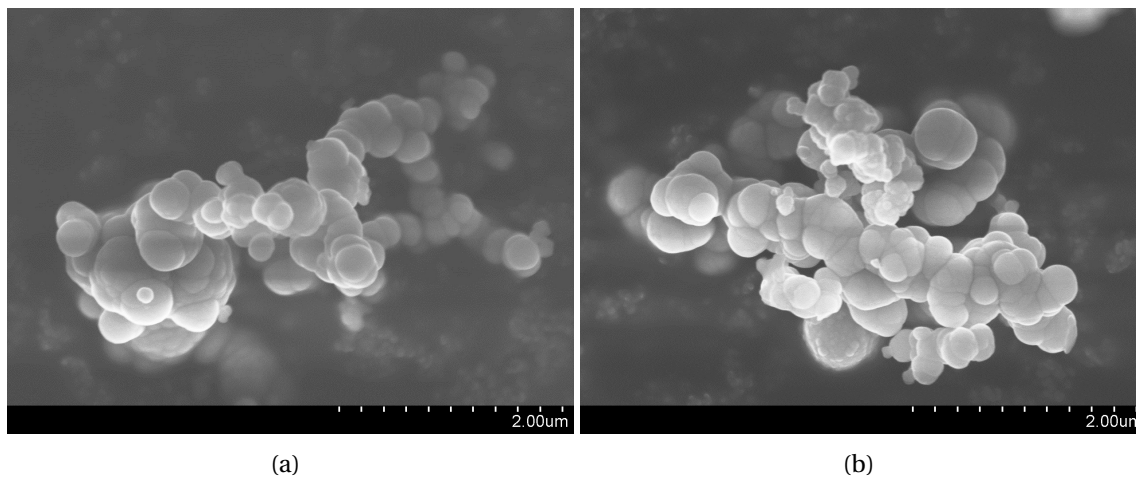
**Figure 4.1:** SEM micrographs of amorphous silicon agglomerates taken at different magnifications using a secondary electron detector. Agglomerate seen in the top right corner of (a) is also shown in (b). Acceleration voltage of 6 kV and WD of 4 mm was used.



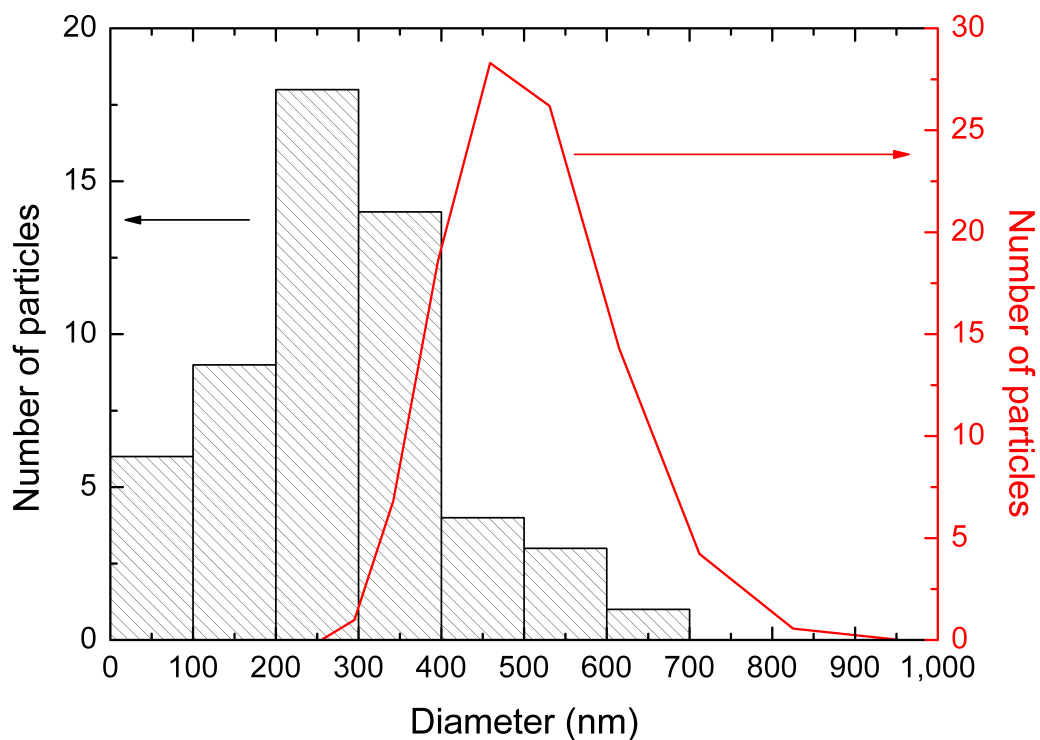
**Figure 4.2:** Particle size distribution of a-Si ref agglomerate from 4.1(b) analyzed in ImageJ (in black) and hydrodynamic particle size distribution from DLS (in red).



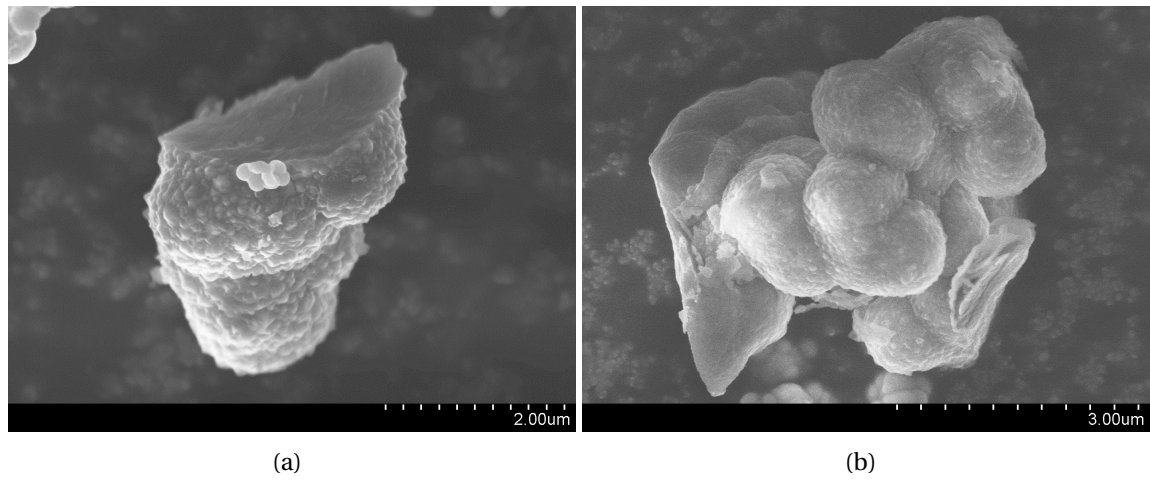
**Figure 4.3:** Overview of agglomerated silicon nanoparticles. Acceleration voltage of 6 kV and WD of 8 mm was used.



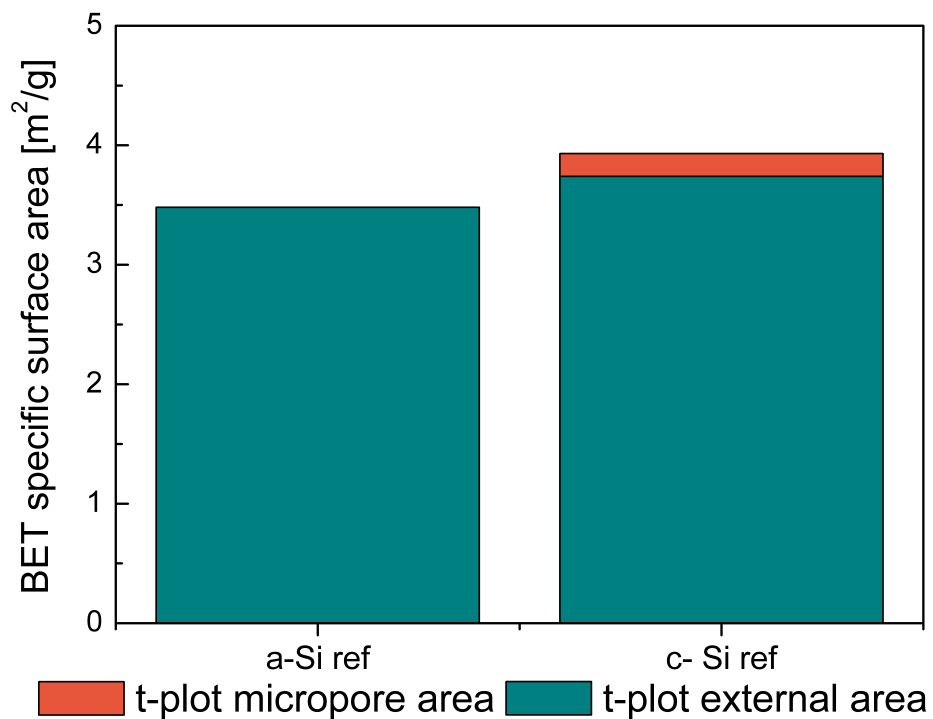
**Figure 4.4:** SEM micrographs of crystalline silicon agglomerates using a secondary electron detector. Acceleration voltage of 6 kV and WD of 4 mm was used.



**Figure 4.5:** Particle size distribution of c-Si ref agglomerate from 4.4(b) analyzed in ImageJ (in black) and hydrodynamic particle size distribution from DLS (in red).



**Figure 4.6:** SEM micrographs of silicon chunks found within the nanoparticles. Acceleration voltage of 6 kV and WD of 4 mm was used.

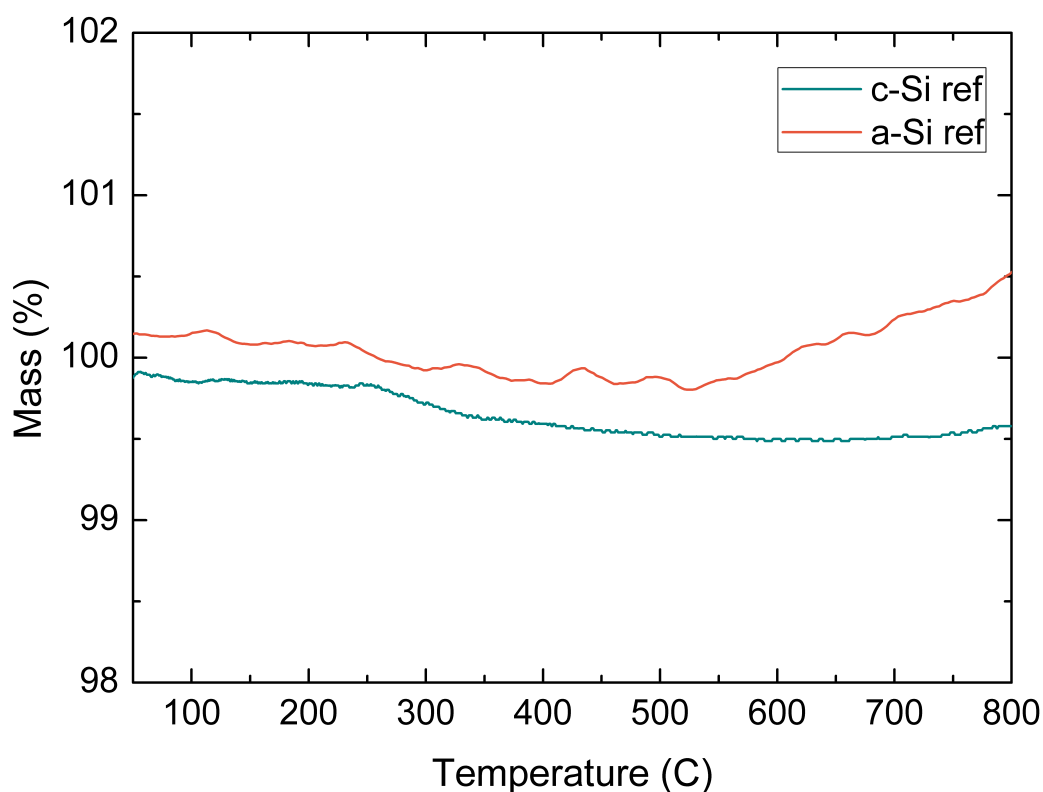


**Figure 4.7:** BET surface area with micropore and external area specification.

**Table 4.1:** BET surface area, t-plot micropore and external area for a-Si ref and c-Si ref. Measured values are rounded to the nearest hundredth.

Area [m <sup>2</sup> /g]	a-Si ref	c-Si ref
BET surface	3.10	3.93
t-plot micropore	-	0.19
t-plot external	3.48	3.74

The resulting mass loss curves from TGA of a-Si ref and c-Si ref can be seen in Figure 4.8, and a small mass loss of 0.3 wt% is in fact seen for c-Si ref between 250 and 600°C. There are larger variations in the mass loss curve of a-Si ref, but no clear drop in mass between 250 and 600°C was observed.

**Figure 4.8:** Thermogravimetric mass loss curves for a-Si ref and c-Si ref.

#### 4.1.1.2 Crystallinity

X-ray diffractograms of the silicon reference powders before and after heat treatment can be seen in Figure 4.9. It is clear that the heat treatment at 800°C lead to a crystallization of the material. The peaks can be seen around  $2\theta = 28^\circ$ ,  $47^\circ$  and  $56^\circ$ , and correspond to different crystal planes in the silicon lattice [80]. These peaks are barely noticeable in a-Si ref, but after heat treatment the peaks have increased in intensity, clearly showing crystallization. Small shoulder peaks were seen at  $26.6^\circ$  and  $57.4^\circ$ , and can most likely be attributed to a native oxide layer on the particles, as they correspond to the (101) and (210) planes in  $\text{SiO}_2$ . Figure 4.10 shows an up-scaled XRD diffractogram of a-Si, with small peaks at  $28^\circ$ ,  $47^\circ$  and  $56^\circ$ .

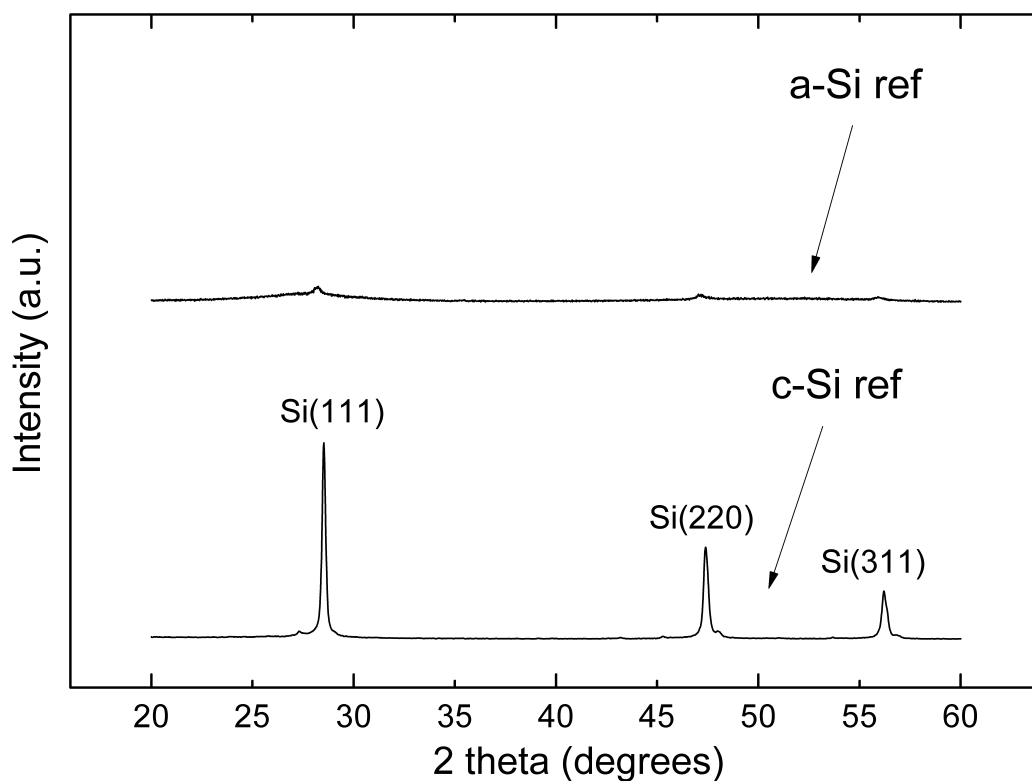


**Figure 4.9:** XRD diffractograms of a-Si ref and c-Si ref before and after heat treatment, respectively. Intensities have been normalized.

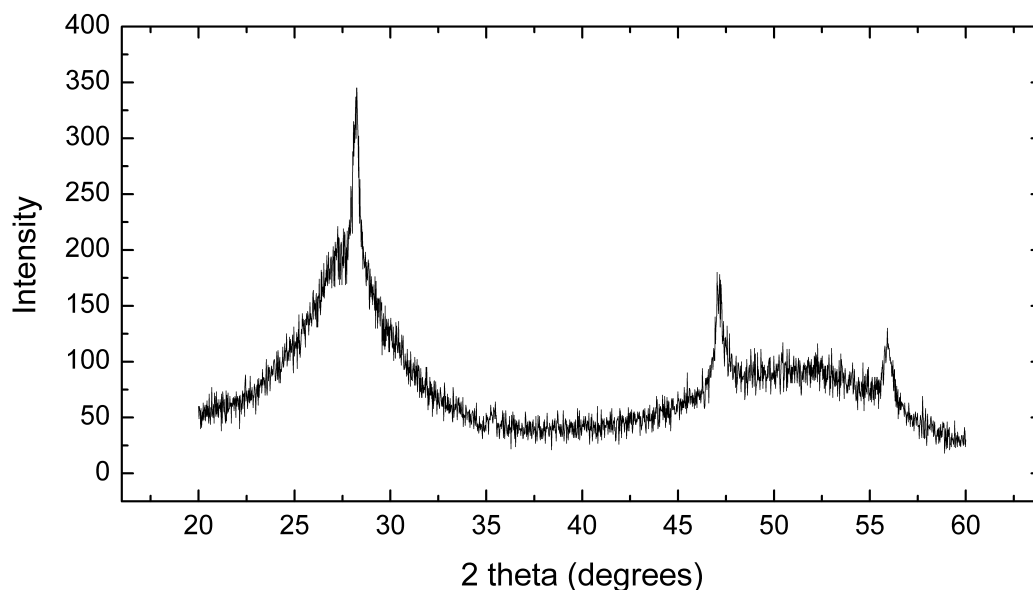


**Figure 4.10:** XRD diffractogram of a-Si ref.

## 4.1.2 Electrochemical results

### 4.1.2.1 Galvanostatic charge-discharge

Galvanostatic cycling of a-Si ref and c-Si ref can be seen in Figure 4.11, where the cells have been cycled to an unlimited capacity at a C-rate of C/5. Capacities are based on total weight of a-Si ref or c-Si ref in the electrode. Summaries of their performance can be seen in Tables 4.2 and 4.3, where initial capacities, ICL, capacity retention after 10 cycles, reversible capacities and lifetimes are listed. The amorphous silicon with a loading of  $\sim 0.5 \text{ mg/cm}^2$  has the highest initial capacity of  $\sim 3,600 \text{ mAh/g}$ , and a low ICL of 1% in the first cycle, while all four cells with crystalline silicon exhibits 8 or 9% ICL in the first cycle. The behavior is quite similar for all six cells during the first 10 cycles, and drops to  $\sim 2,000 \text{ mAh/g}$  for the four cells with higher loadings of  $\sim 0.5 \text{ mg/cm}^2$ , and  $\sim 1,800 \text{ mAh/g}$  for the lower loadings of  $\sim 0.4 \text{ mg/cm}^2$ , respectively giving capacity retentions of 58 and 66%.

The amorphous silicon retains 90% of its reversible capacity for almost 70 cycles, with a corresponding increase in IR when the cell begins to fail. The four cells with crystalline silicon however, show very different results, where the higher loading (c-Si ref (05)&(06)) leads to an increase in capacity before an early death after  $\sim 50$  cycles, and the lower loading (c-Si ref (01)&(02)) leads to a stable reversible capacity of  $\sim 1,800 \text{ mAh/g}$  for 120-140 cycles, and only display a slight increase in IR over the course of their lifetimes.

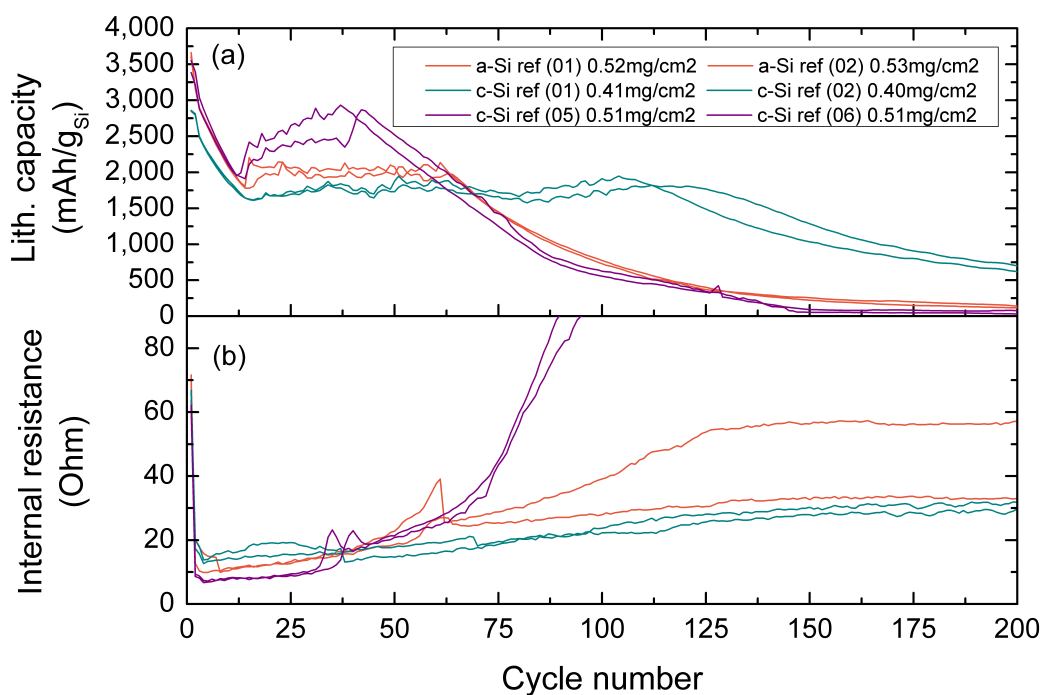


**Figure 4.11:** Galvanostatic-charge discharge to an unlimited capacity. Values plotted are (a) lithiation capacity and (b) internal resistance.

**Table 4.2:** Summary of galvanostatic unlimited cycling of a-Si ref and c-Si ref.

Cell	Lith. capacity	Delith. capacity	ICL	Capacity retention	
Cycle	1.	1.	10.	1.	after 10 cycles
	[mAh/g]	[mAh/g]	[mAh/g]	[%]	[%]
a-Si ref (01)	3,602	3,563	2,071	1	58
a-Si ref (02)	3,663	3,640	2,110	1	58
c-Si ref (01)	2,859	2,615	1,850	9	65
c-Si ref (02)	2,849	2,623	1,887	8	66
c-Si ref (05)	3,385	3,082	2,098	9	58
c-Si ref (06)	3,549	3,240	2,137	9	60

**Table 4.3:** Unlimited cycling: reversible capacities and lifetimes for Si reference.

Cell	Reversible capacity [mAh/g]	Lifetime [Cycles]
a-Si ref (01)	1,970	68
a-Si ref (02)	2,057	66
c-Si ref (01)	1,767	121
c-Si ref (02)	1,723	137
c-Si ref (05)	2,507	56
c-Si ref (06)	2,658	48

Half-cells with amorphous and crystalline Si were also cycled to a limited capacity of 1,200 mAh/g at a C-rate of C/5. The results from galvanostatic cycling of these cells can be seen in Figure 4.12, with a summary of their performance in Table 4.4. A clear difference between the amorphous and crystalline silicon is the bump in capacity seen for c-Si ref within the first 30 cycles, which was not seen for a-Si ref. Voltage curves for the first cycle of two amorphous and two crystalline cells (a-Si ref (03) & (04) and c-Si ref (03) & (04)) are shown in Figure 4.14. One half-cell of a-Si ref was also cycled to a lower capacity of 720 mAh/g at a slower C-rate of C/10 in previous work [1], and can be seen in Figure 4.13. This cell displayed superior capacity retention for 996 cycles before failing.

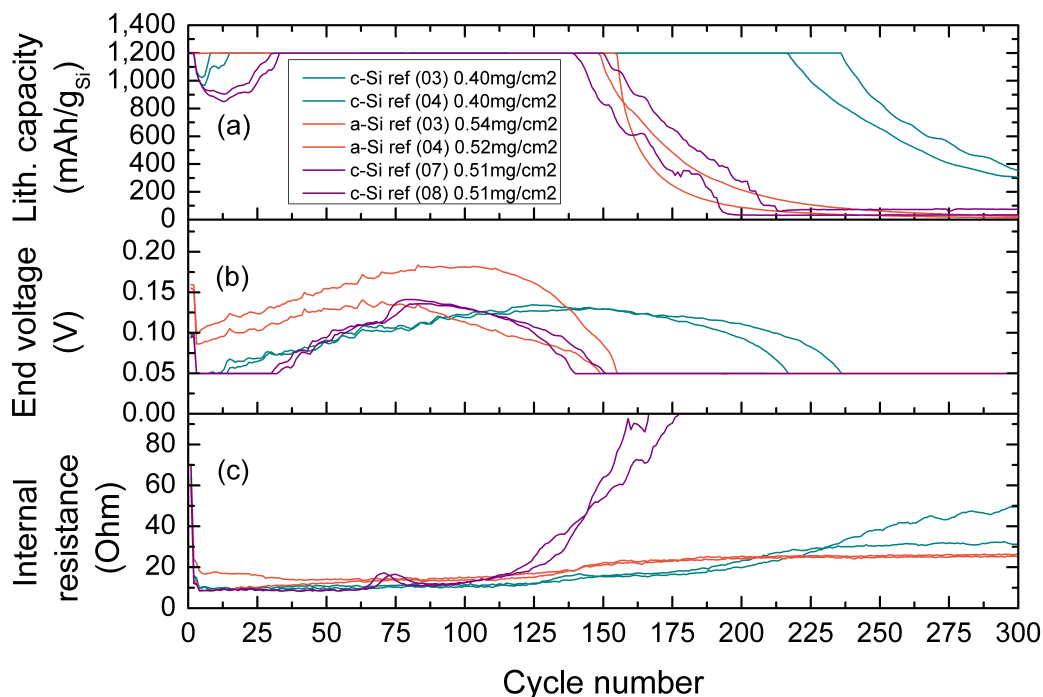


**Figure 4.12:** Galvanostatic charge-discharge of Si ref at a limited capacity of 1,200 mAh/g. Values plotted are (a) lithiation capacity, (b) end voltage, and (c) internal resistance.

**Table 4.4:** Summary of galvanostatic limited cycling of a-Si ref and c-Si ref.

Cell	1. cycle lith. capacity [mAh/g]	1. cycle de-lith. capacity [mAh/g]	ICL [%]	Lifetime Cycles
a-Si ref (03)	1195	1053	12	148
a-Si ref (04)	1196	1050	12	154
c-Si ref (03)	1197	1016	15	236
c-Si ref (04)	1196	1021	15	216
c-Si ref (07)	1195	1011	15	150
c-Si ref (08)	1203	1038	14	139

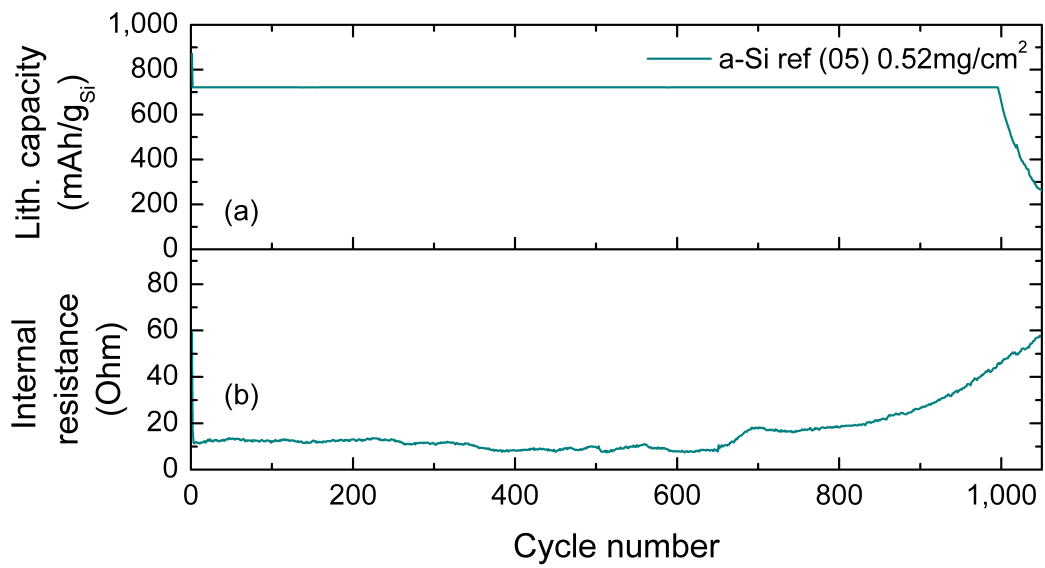


**Figure 4.13:** Galvanostatic charge-discharge of a-Si ref (05) at a limited capacity of 720 mAh/g. Values plotted are (a) lithiation capacity and (b) internal resistance.

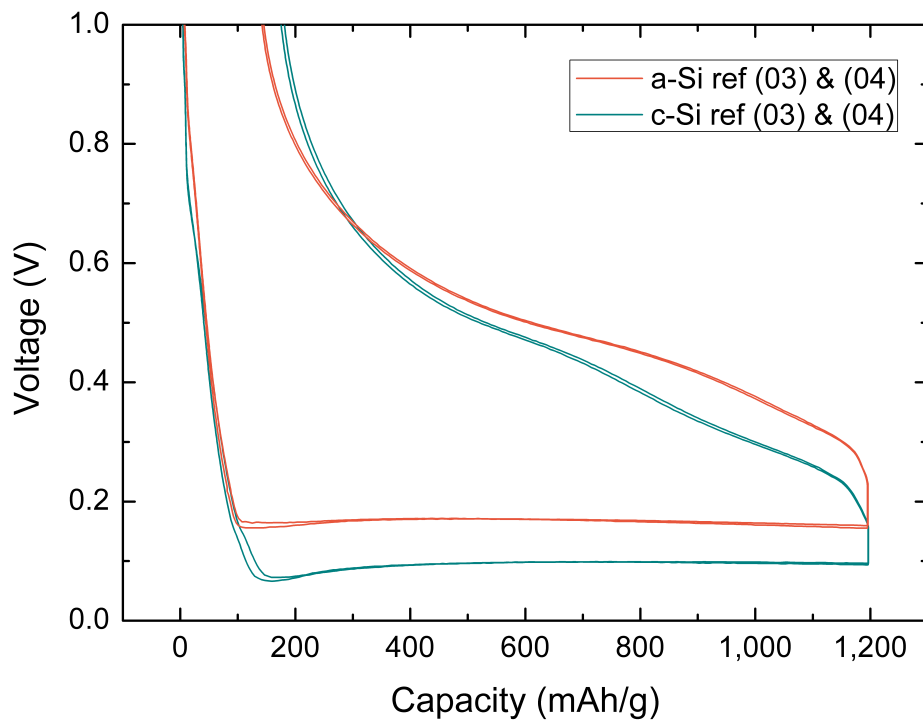


**Figure 4.14:** Voltage curves for the first cycle of four Si reference cells cycled to a limited capacity of 1,200 mAh/g.

The  $dQ/dV$  plots for both amorphous and crystalline silicon cycled to a unlimited capacity can be seen in Figure 4.15, and it is clear that the initial lithiation is dependent upon the crystallinity of the starting active material. The initial lithiation of c-Si ref is at  $\sim 0.1$  V, where the initial lithiation of a-Si ref is much higher, at  $\sim 0.18$  V. The first cycle de-lithiation peak is also characteristically seen at  $\sim 0.43$  V for both materials. In the following cycles the materials are much more similar, and a broad lithiation peak is observed at  $\sim 0.30$ - $0.25$  V, with a second lithiation peak at  $\sim 0.11$  V. Signs of a third lithiation peak close to  $0.05$  V is also seen for both, but as the cut-off potential is  $0.05$  V this peak is faint and uncertain. De-lithiation in cycles 2 and 3 are also quite similar for both materials, with peaks at  $\sim 0.27$  V and  $\sim 0.48$  V.

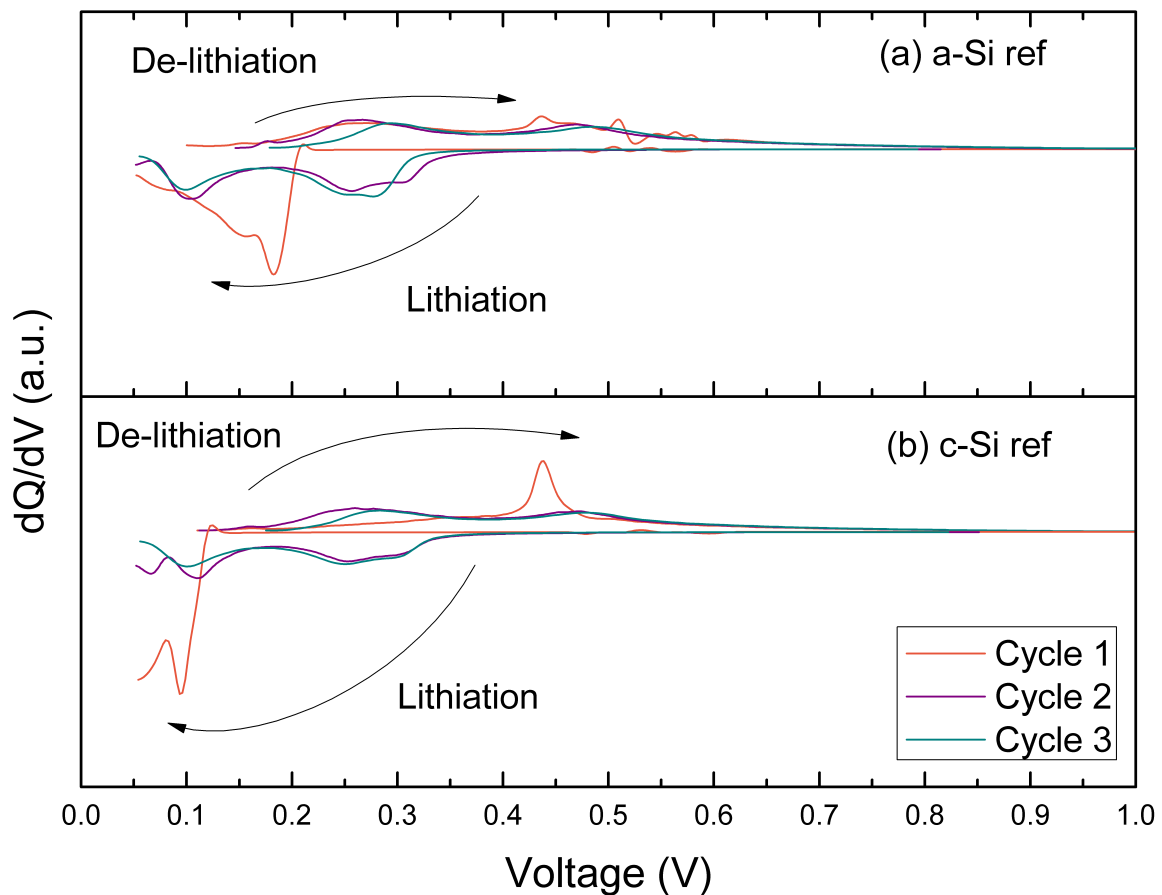


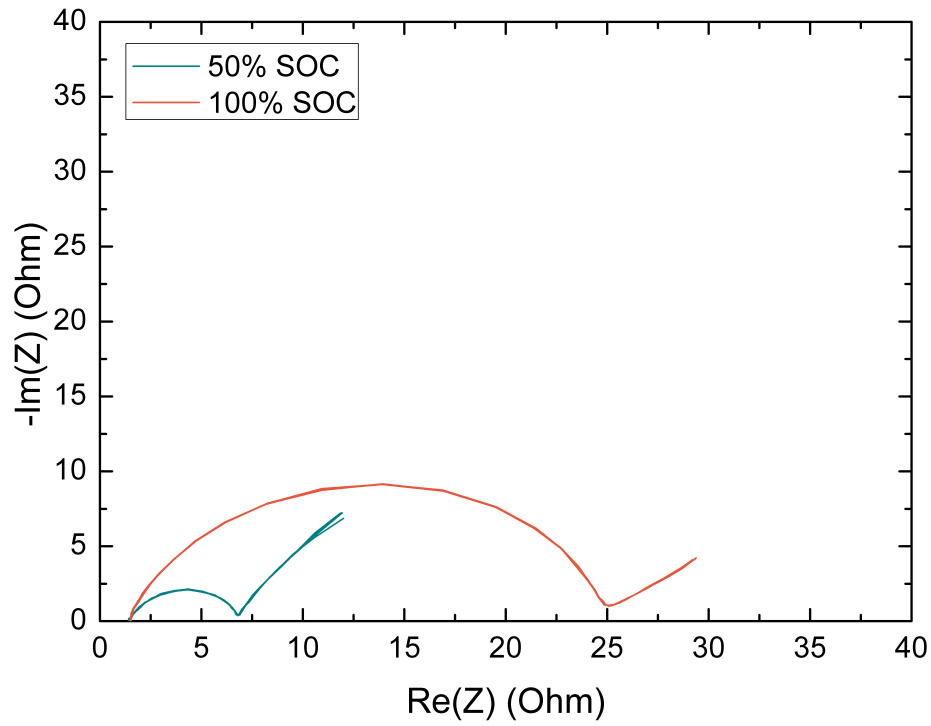
**Figure 4.15:**  $dQ/dV$  plots of a-Si ref and c-Si ref.

#### 4.1.2.2 Electrochemical Impedance Spectroscopy

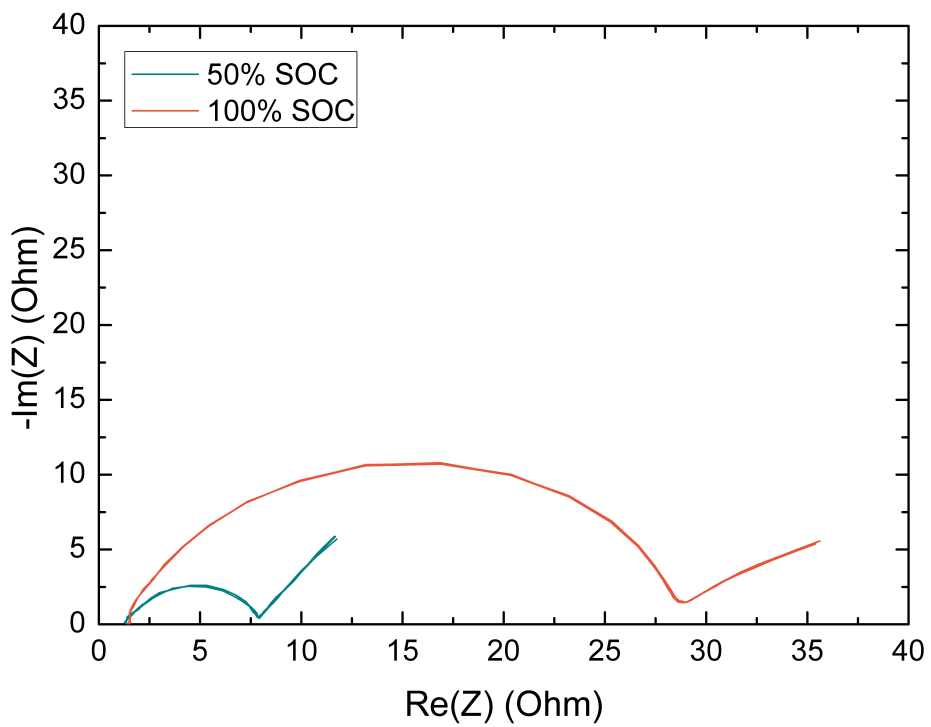
In Figure 4.16 the Nyquist plots obtained from GEIS of a-Si ref and c-Si ref are shown. A-Si ref and c-Si ref are compared by SOC in Figure 4.17. By fitting this data to a Randles equivalent circuit (shown in Figure 2.17, Section 2.4.2.4), the approximated resistances and capacitances for the cell can be found, and are summarized in Table 4.5. Nyquist plots from both anodes at 50% SOC and 100% SOC lithiated state, showed a slightly larger impedance for c-Si ref in both cases. The solution resistance is similar, as expected, as the same electrolyte was used for all cells.

**Table 4.5:** A summary of impedance results for a-Si ref and c-Si ref fitted to a Randles equivalent circuit.

Cell	SOC [%]	$R_{\Omega}$ [Ohm]	$C_{dl}$ [F]	$R_{CT}$ [Ohm]	$Z_W$ [ohm/ $\sqrt{s}$ ]
a-Si ref	50	1.5	$55e-6 \pm 26e-6$	4.7	4.0
	100	1.5	$12e-6 \pm 1e-6$	23.2	3.3
c-Si ref	50	1.4	$54e-6 \pm 21e-6$	5.6	3.5
	100	1.4	$13e-6 \pm 1e-6$	25.0	6.0

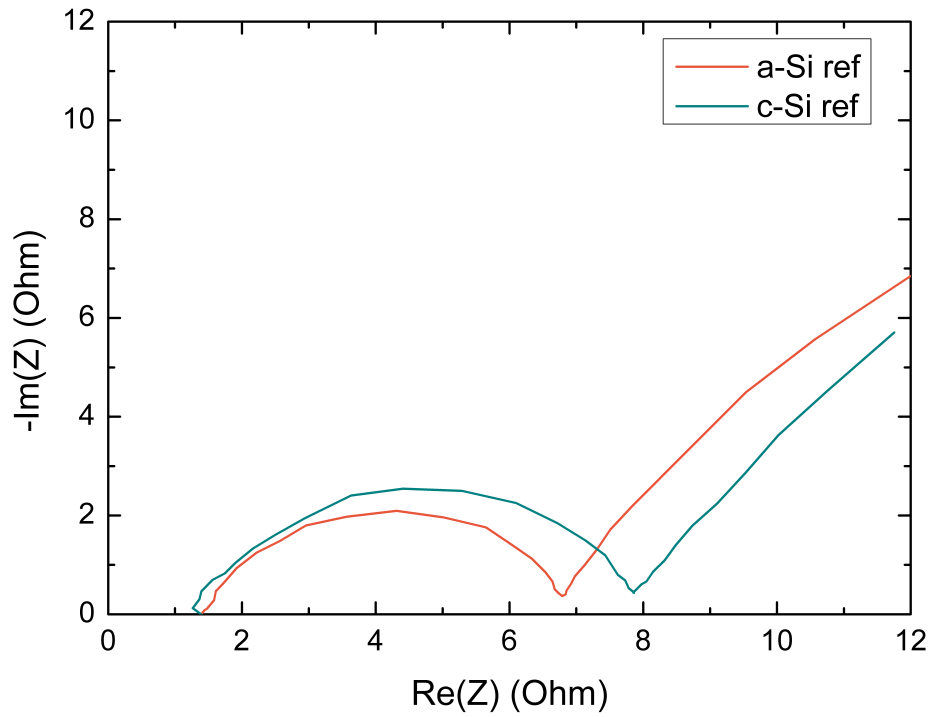


(a)

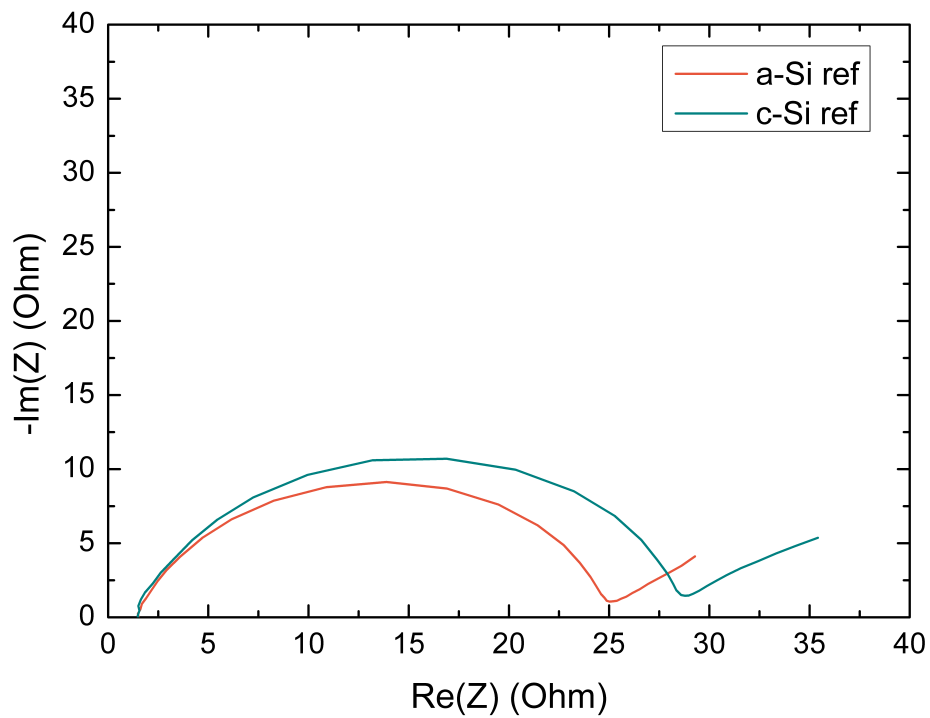


(b)

**Figure 4.16:** Nyquist plots of (a) a-Si ref and (b) c-Si ref.



(a)



(b)

**Figure 4.17:** Nyquist plots of a-Si ref and c-Si ref at (a) 50% SOC and (b) 100% SOC. Mark the large difference in the x-axis to emphasize differences between a-Si ref and c-Si ref at both SOC.

## 4.2 Oxide coating by TEOS

### 4.2.1 Structural characterization

SEM and TEM micrographs of oxide coated silicon,  $\text{Si@SiO}_2$ , can be seen in Figure 4.18 and 4.20. It is clear that the morphology of the particles did not change significantly after the silica coating, all though it may look like the oxide coating interconnects two or more silicon agglomerates, making secondary agglomerates. Shown in Figure 4.19, a wide size distribution of particles ranging from 50 nm to almost 2  $\mu\text{m}$  in diameter was found by particle size analysis in ImageJ and by DLS. Unless otherwise specified, the batches TEOS08 and TEOS09 were used in the characterizations, and these powders are synthesized under the same conditions.

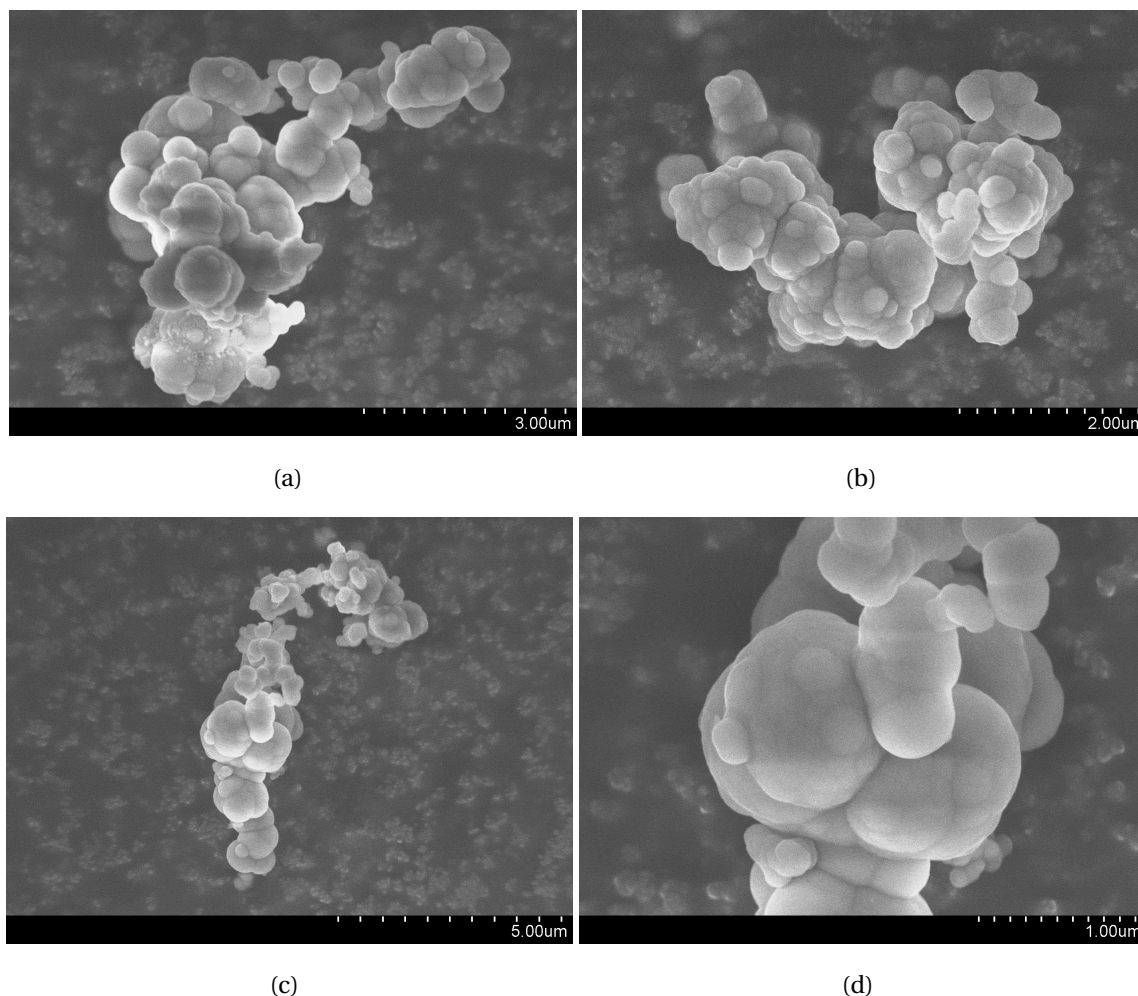


**Figure 4.18:** SEM micrographs of oxide coated silicon,  $\text{Si@SiO}_2$ . The SEM was operating at 6 kV with a WD of 4 mm.

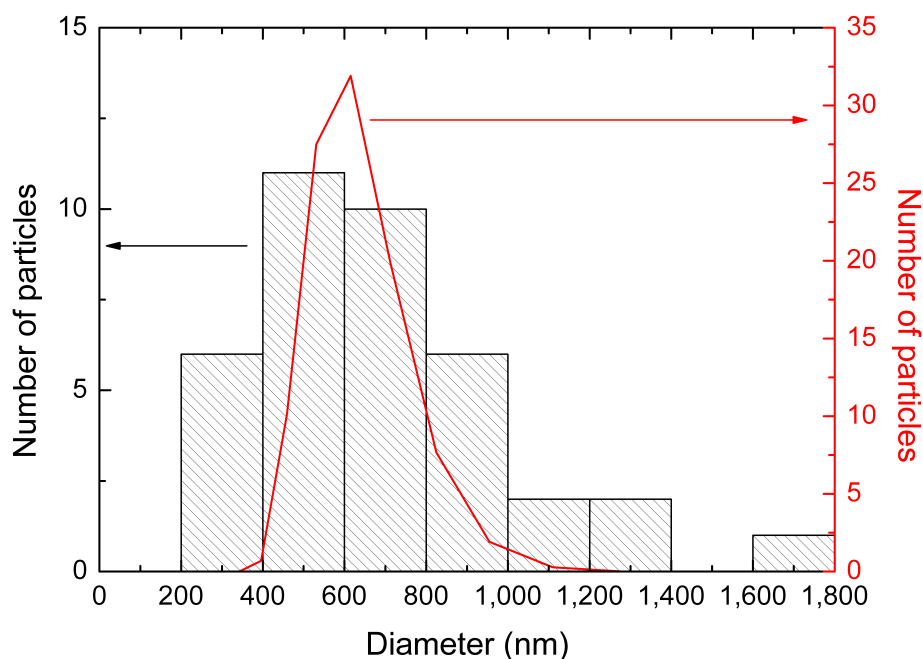


**Figure 4.19:** Particle size distribution of agglomerate from 4.18(a) analyzed in ImageJ (in black) and hydrodynamic particle size distribution from DLS (in red).

The TEM micrograph in Figure 4.20 clearly shows an oxide coating on the Si particle, and not a native oxide layer, as the boundary between silicon and oxide is distinct due to contrast intensity in the image. The thickness of this coating is 24 nm and quite homogeneous. In Figure 4.21 another TEM micrograph of an aggregate of particles can be seen, with the oxide coating thickness varying between 50 nm and 80 nm throughout the sample. This coating is quite homogeneous on each individual particle.

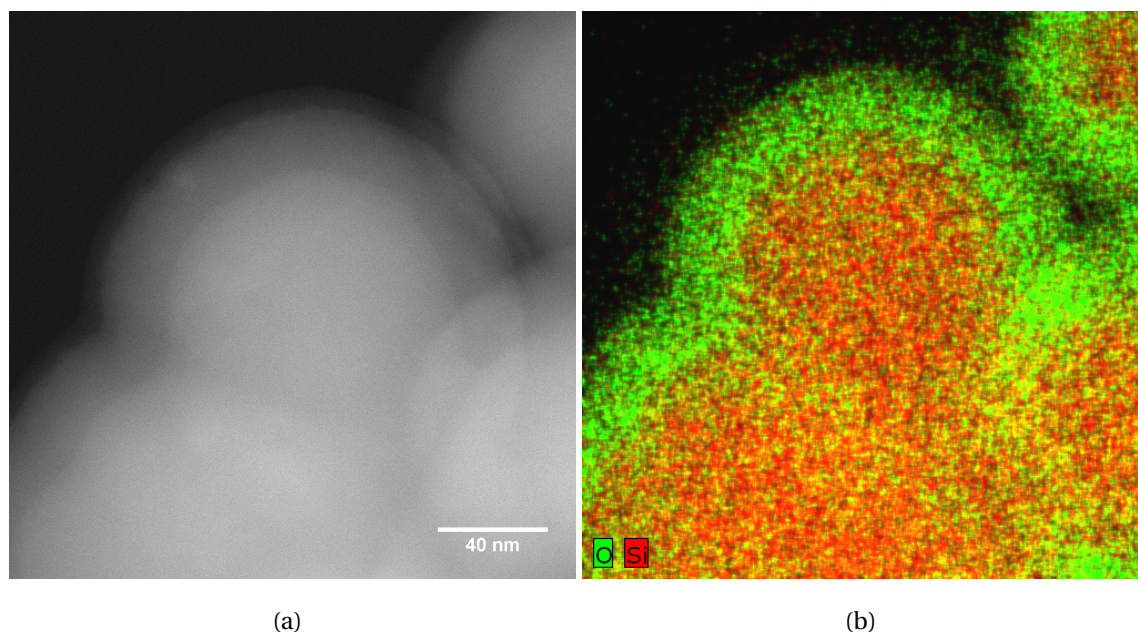


**Figure 4.20:** (a) TEM micrograph a particle found in a mixture of TEOS04 and TEOS05. A single particle with diameter of 130 nm and (b) EDS mapping of same particle. TEM performed by Asbjørn Ulvestad at UiO with an accelerating voltage of 300 kV.

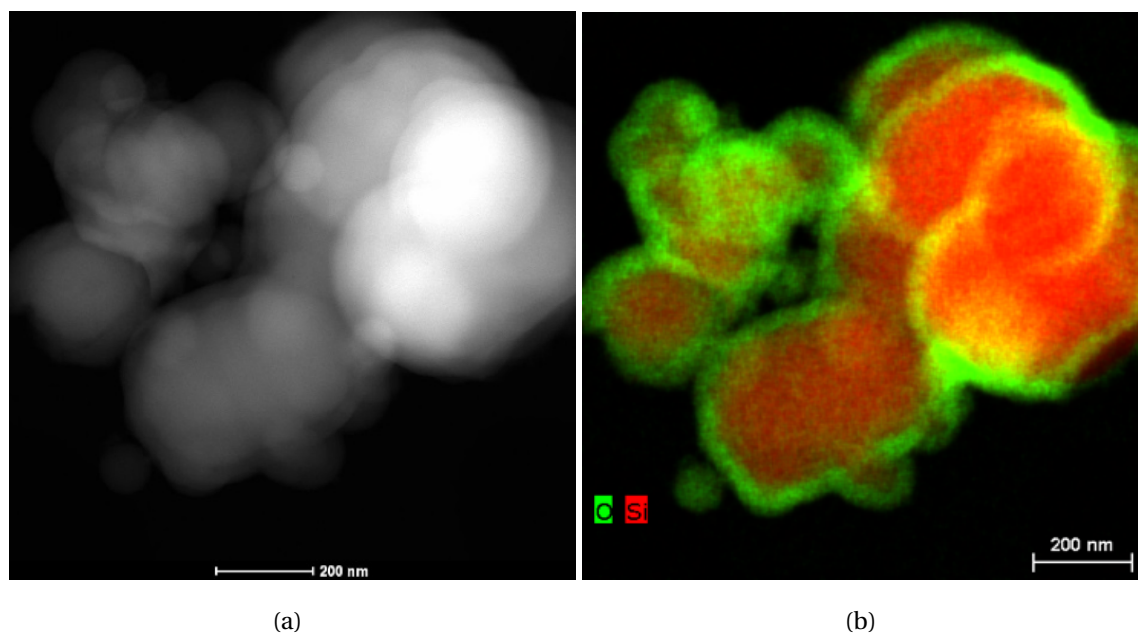


**Figure 4.21:** (a) TEM micrograph of Si@SiO<sub>2</sub>-aggregate and (b) EDS mapping. TEM performed by Patricia Almeida Carvalho at Sintef with an accelerating voltage of 300 kV. The Si@SiO<sub>2</sub> batch analyzed here was produced with the same synthesis parameters as TEOS08 and TEOS09.

X-ray diffractograms of a-Si ref and the Si@SiO<sub>2</sub> can be seen in Figure 4.22. The crystallinity of the particles have not changed after coating, and it is still mostly amorphous except for the small crystalline peaks at  $2\theta = 28^\circ$ ,  $47^\circ$  and  $56^\circ$ .

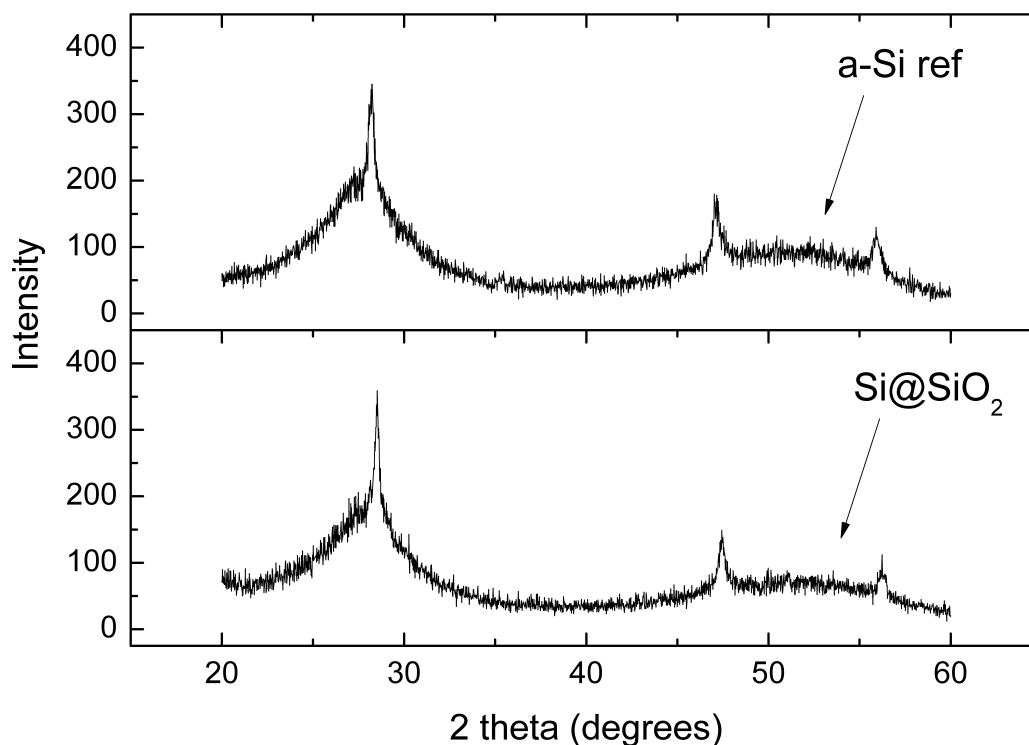


**Figure 4.22:** XRD diffractograms of a-Si ref and Si@SiO<sub>2</sub>.

## 4.2.2 Electrochemical results

### 4.2.2.1 Galvanostatic charge-discharge

Half-cells containing anodes of Si@SiO<sub>2</sub>-particles were galvanostatically cycled, and the results can be seen in Figures 4.23 and 4.24 for unlimited and limited cycling at C/5, respectively. Capacities are based on total weight of Si@SiO<sub>2</sub> in electrode. It is clear that the results are similar for both unlimited and limited cycling, where an initial lithiation capacity of approximately 1,200 mAh/g was seen for all four cells cycled, but this capacity quickly decreased to ~100 mAh/g after only a few cycles, giving a capacity retention below 10%. The voltage curves corresponding to the first 10 cycles clearly show a gradual decrease in capacity, and can be seen in Figure 4.25. A summary of their electrochemical performance can be seen in Table 4.6.

Individual variations seen in the internal resistance can be attributed to cell fabrication.

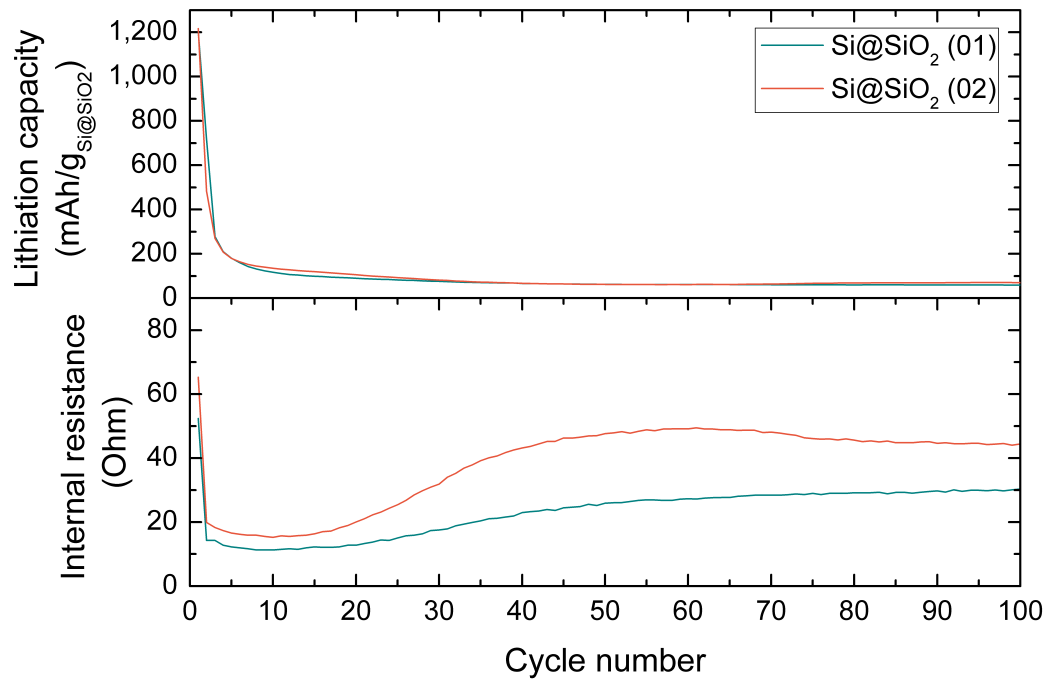


**Figure 4.23:** Galvanostatic charge-discharge of Si@SiO<sub>2</sub> to an unlimited capacity. Values plotted are (a) lithiation capacity and (b) internal resistance.

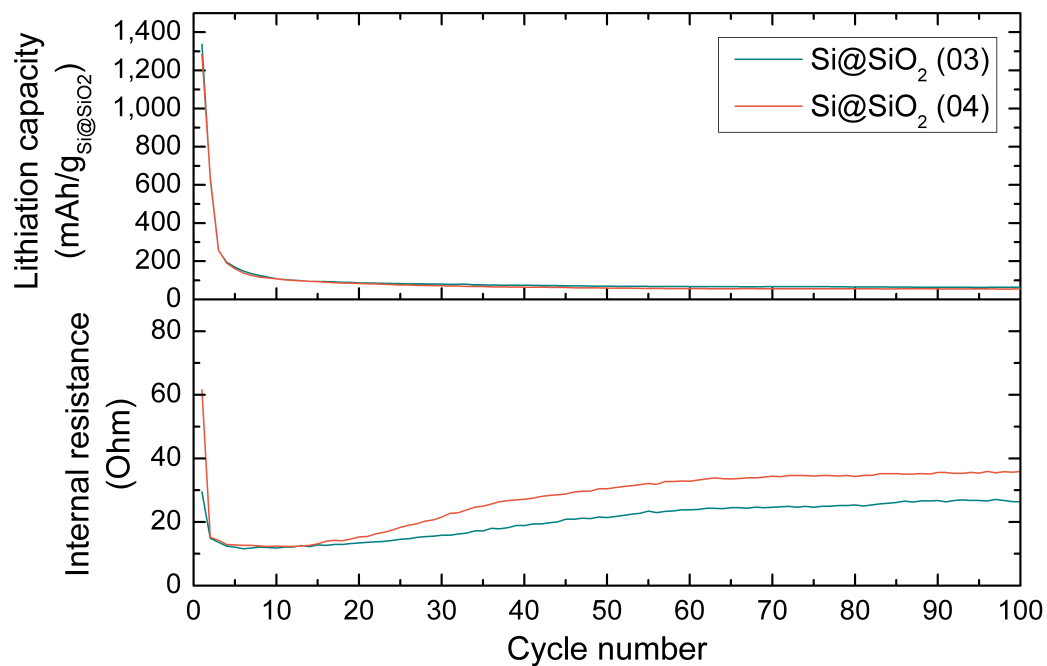


**Figure 4.24:** Galvanostatic charge-discharge of Si@SiO<sub>2</sub> at a limited capacity of 1,200 mAh/g. Values plotted are (a) lithiation capacity and (b) internal resistance.

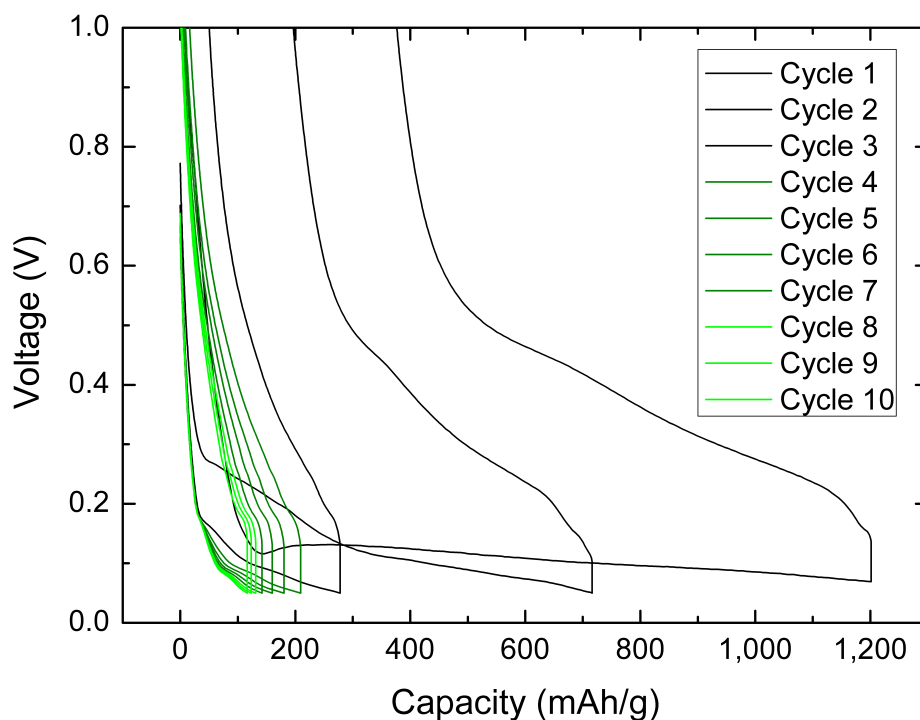


**Figure 4.25:** Voltage curves for the first 10 cycles of galvanostatic cycling of Si@SiO<sub>2</sub>.

**Table 4.6:** Summary of galvanostatic cycling of Si@SiO<sub>2</sub>.

Cell	Lith. capacity	De-lith. capacity		ICL	Capacity retention
Cycle	1.	1.	10.	1.	after 10 cycles
	[mAh/g]	[mAh/g]	[mAh/g]	[%]	[ %]
Si@SiO <sub>2</sub> (01)	1,337	921	108	31	8
Si@SiO <sub>2</sub> (02)	1,201	825	115	31	10
Si@SiO <sub>2</sub> (03)	1,251	901	102	28	8
Si@SiO <sub>2</sub> (04)	1,283	867	106	32	8

A differential capacity plot from cycling of Si@SiO<sub>2</sub>-anodes can be seen in Figure 4.26, as well as plotted against a-Si ref in Figure 4.27. It is clear that a much lower activity is seen in the Si@SiO<sub>2</sub>-anodes, but the overall shape is quite similar as for Si. Slight differences in the potentials of the first cycle lithiation (a split peak around 0.2-0.1 V) and de-lithiation peaks can be seen. The wider de-lithiation peaks may be attributed to SiO<sub>x</sub>.

#### 4.2.2.2 Electrochemical Impedance spectroscopy

In Figures 4.28 the Nyquist plots obtained from GEIS of Si@SiO<sub>2</sub> anodes are shown at 50% and 100% SOC. The data is also shown in Figure 4.29, where it is compared to a-Si

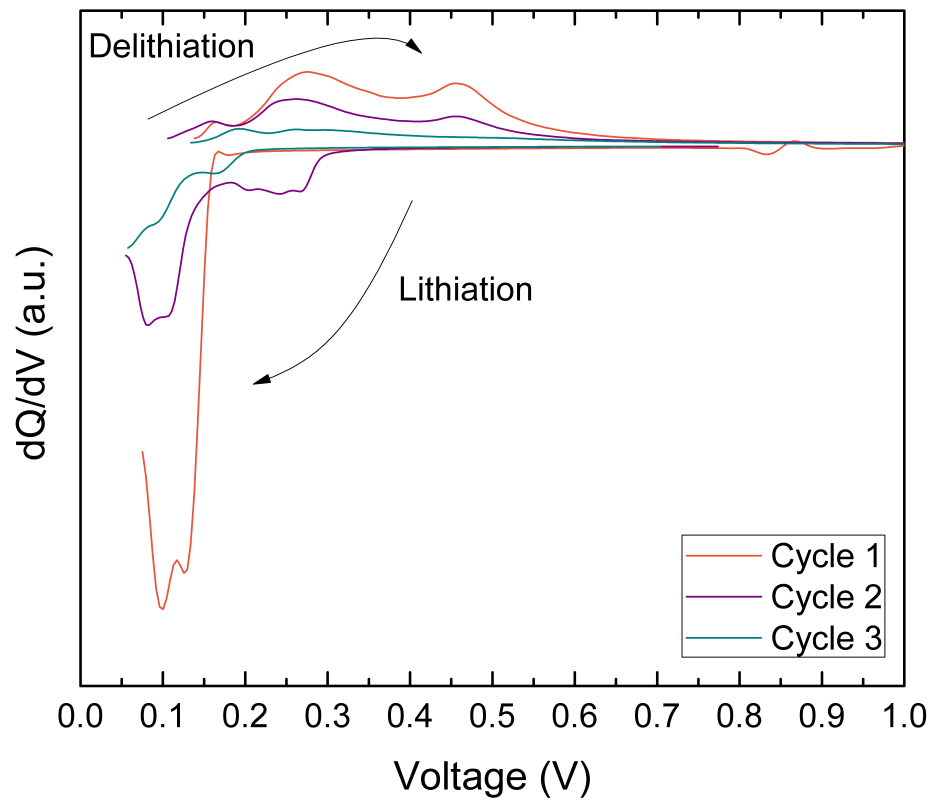


Figure 4.26:  $dQ/dV$  plots of  $\text{Si@SiO}_2$ .

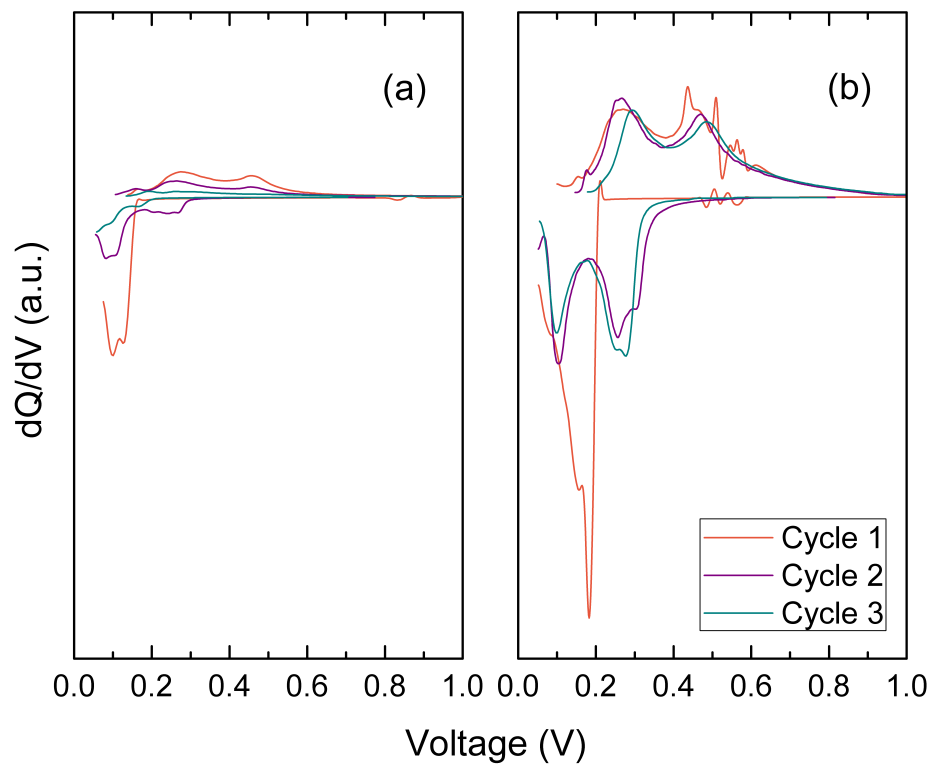
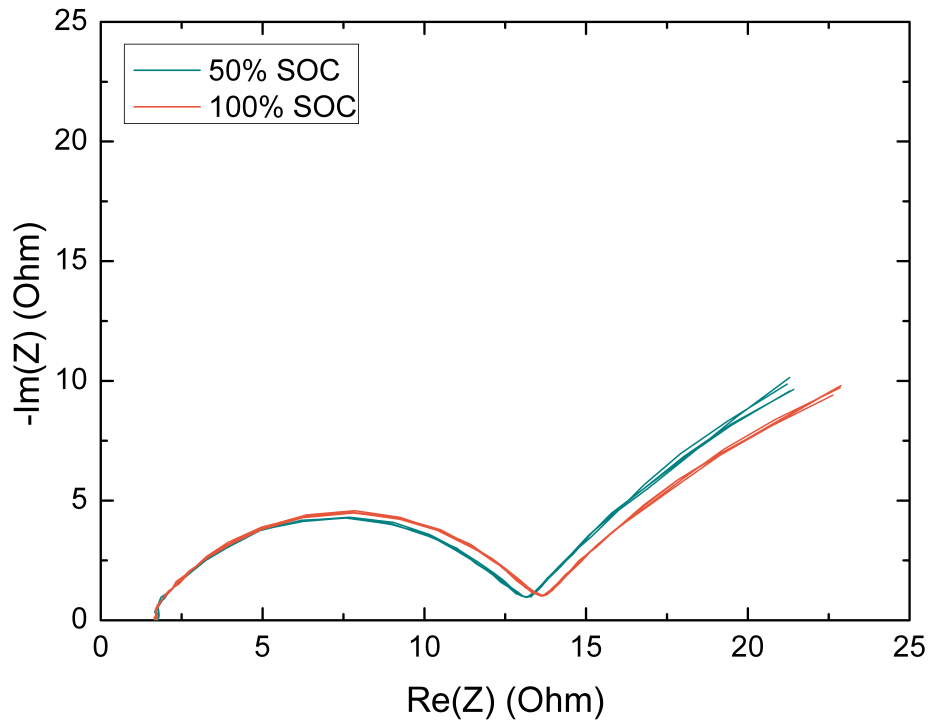


Figure 4.27:  $dQ/dV$  plots of (a)  $\text{Si@SiO}_2$  and (b) a-Si ref. The curves are normalized and have the same scale.

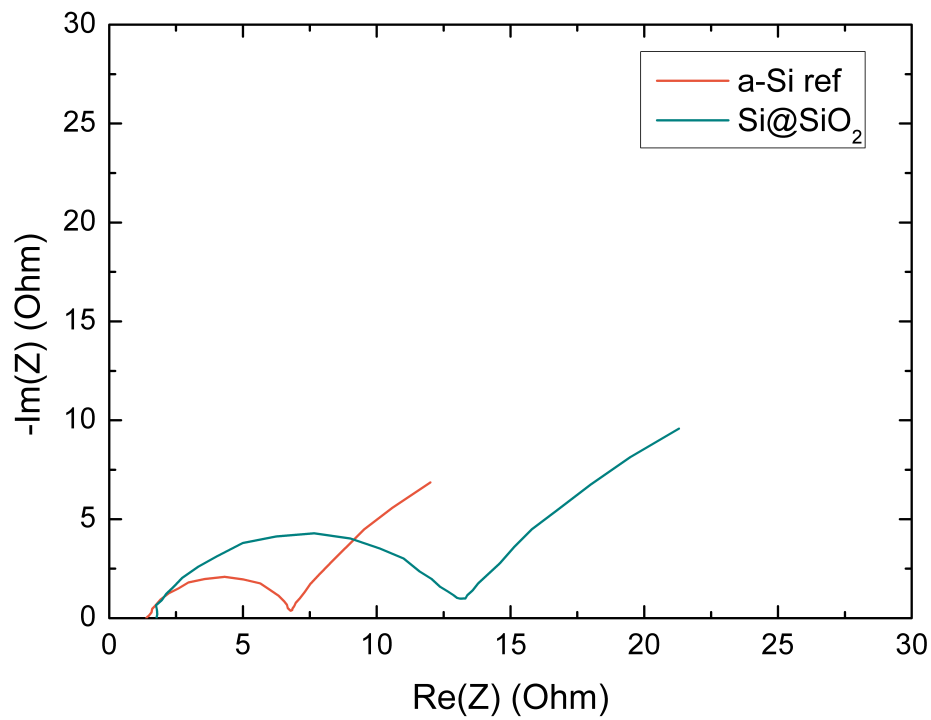
ref at each SOC. By fitting this data to a Randles equivalent circuit, the approximated resistances and capacitances for the electrode are summarized in Table 4.7.



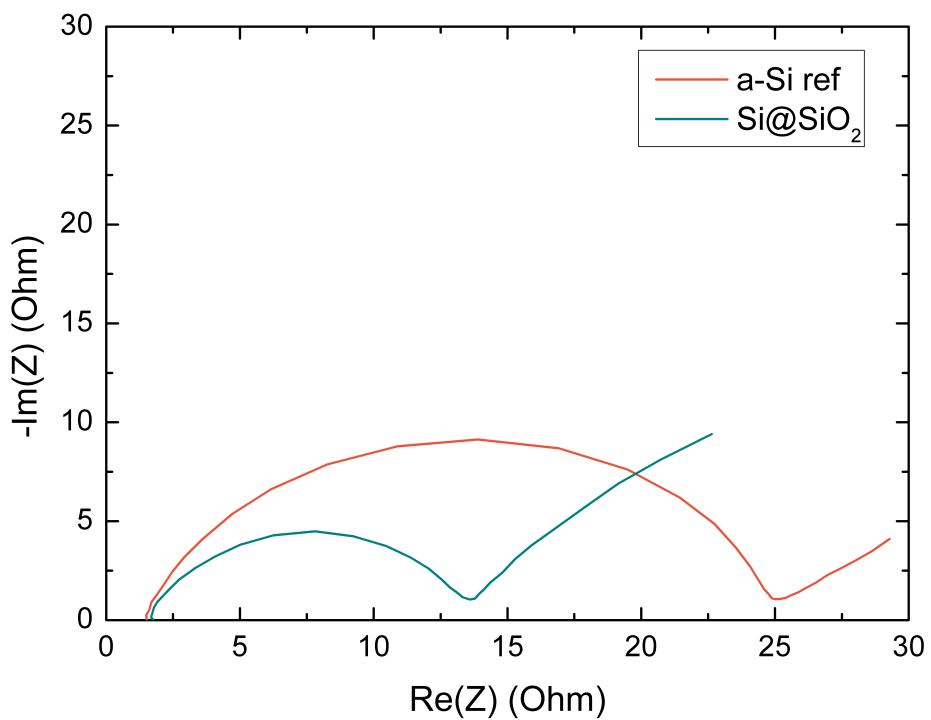
**Figure 4.28:** Nyquist plots of Si@SiO<sub>2</sub> at 50% SOC and 100% SOC. All four re-runs of the GEIS-measurement are plotted for each SOC.

**Table 4.7:** A summary of impedance results for Si@SiO<sub>2</sub>-anodes compared to a-Si ref, fitted to a Randles equivalent circuit.

	SOC	$R_{\Omega}$	$C_{dl}$	$R_{CT}$	$Z_w$
Cell	[%]	[Ohm]	[F]	[Ohm]	[ohm/ $\sqrt{s}$ ]
a-Si ref	50	1.5	55e-6±26e-6	4.7	4.0
	100	1.5	12e-6±1e-6	23.2	3.2
Si@SiO <sub>2</sub>	50	1.8	25e-6±6e-6	9.7	7.0
	100	1.8	25e-6±5e-6	10.1	7.5



(a)



(b)

**Figure 4.29:** Nyquist plots of Si@SiO<sub>2</sub> vs. a-Si ref at (a) 50% SOC and (b) 100% SOC.

### 4.3 Carbon coating by RF

To determine the appropriate molarity of added CTAB for complete coverage and a positive zeta potential, ELS was done and the results can be seen in Figure 4.30. By adding 500  $\mu\text{l}$  of 5 or 10 mM CTAB to 50 mg Si in 15 ml DI water, a positive zeta potential of  $\sim 30$  mV was found, and 10 mM was chosen to ensure sufficient coverage in the C-coating.

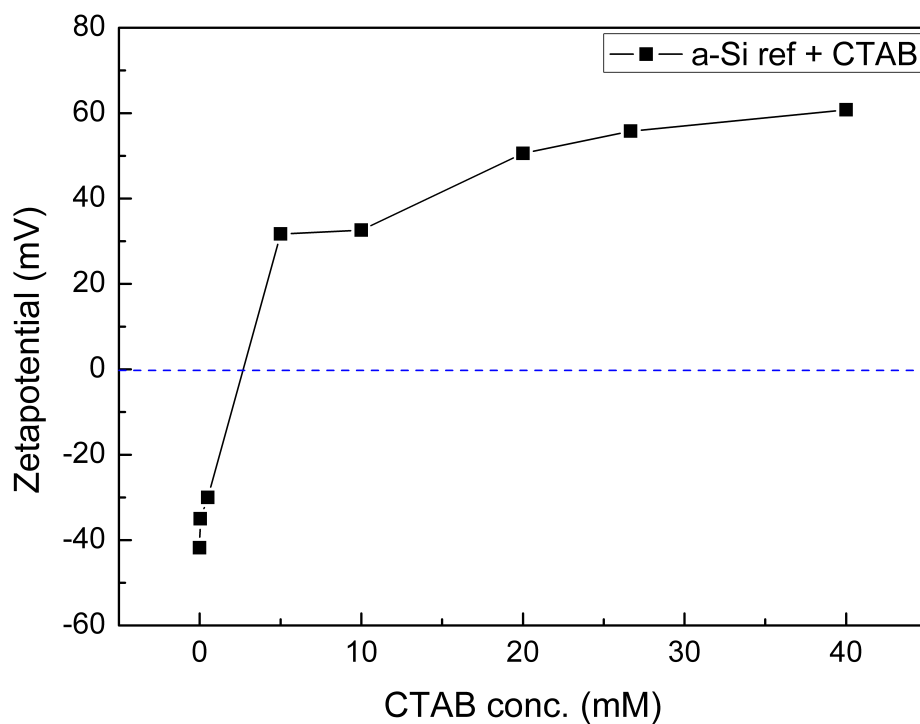


**Figure 4.30:** Zetapotential after covering surface of silicon with cationic surfactant, CTAB.

### 4.3.1 Structural characterization

SEM micrographs of the carbon coated batch RF03 can be seen in Figure 4.31. A clear change in morphology is seen, as the particles and agglomerates are interconnected with a web-like coating of carbon.

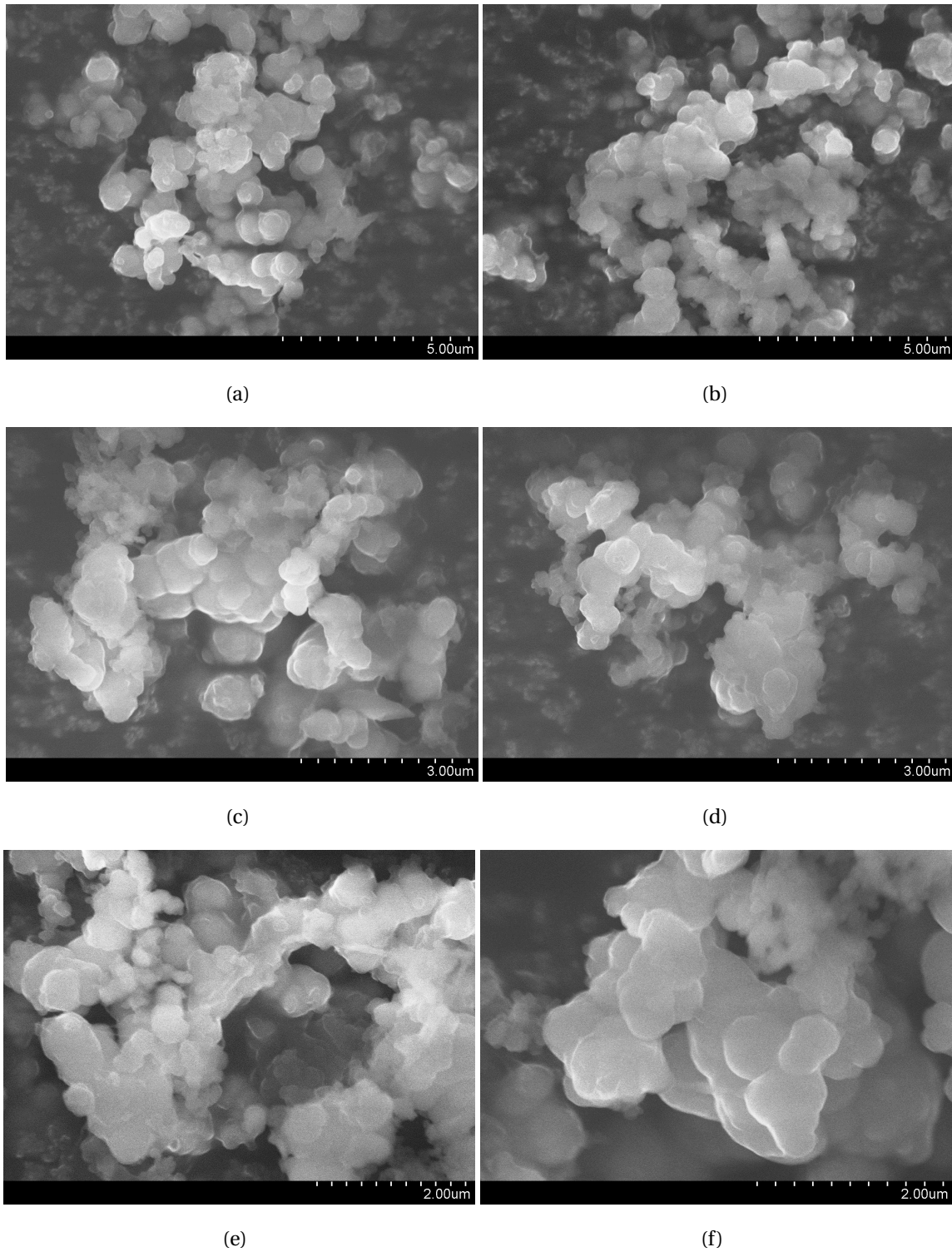


**Figure 4.31:** SEM micrographs of Si@SiO<sub>2</sub>@C. V<sub>acc</sub> = 15 kV, WD = (a)-(e) 8 mm (f) and 4 mm.

This batch was also investigated by the transmission mode of the SEM, and some micrographs, with low resolution due to vibrations, can be seen in Figures 4.32. The carbon coating thickness was determined by TEM-micrographs to be between 10 nm and 14 nm, which can be seen in Figure 4.33. The oxide layer on the imaged particle in 4.33 is found to be between 20 nm and 22 nm.

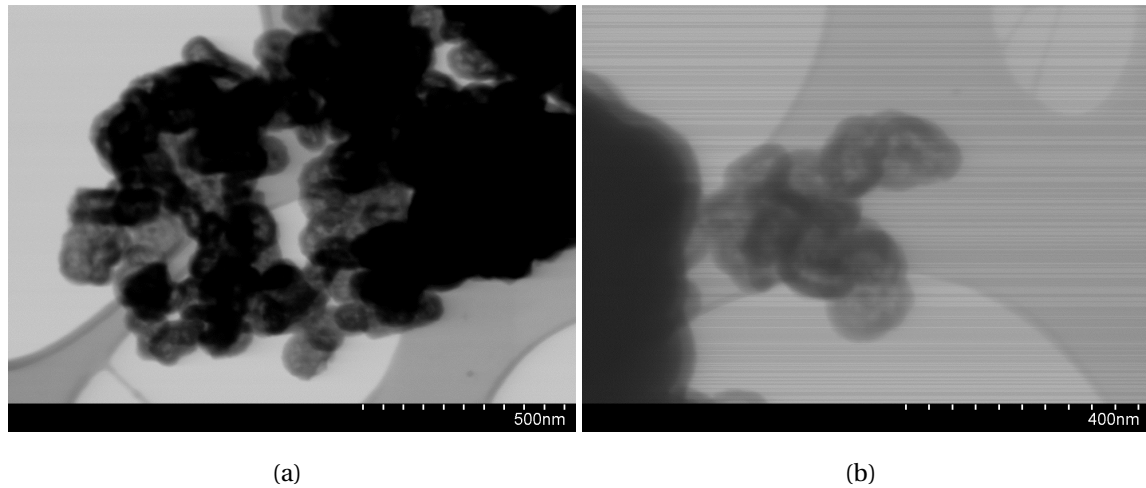


**Figure 4.32:** STEM micrographs of Si@SiO<sub>2</sub>@C. The SEM was operating at 30 kV with WD of 6 mm.

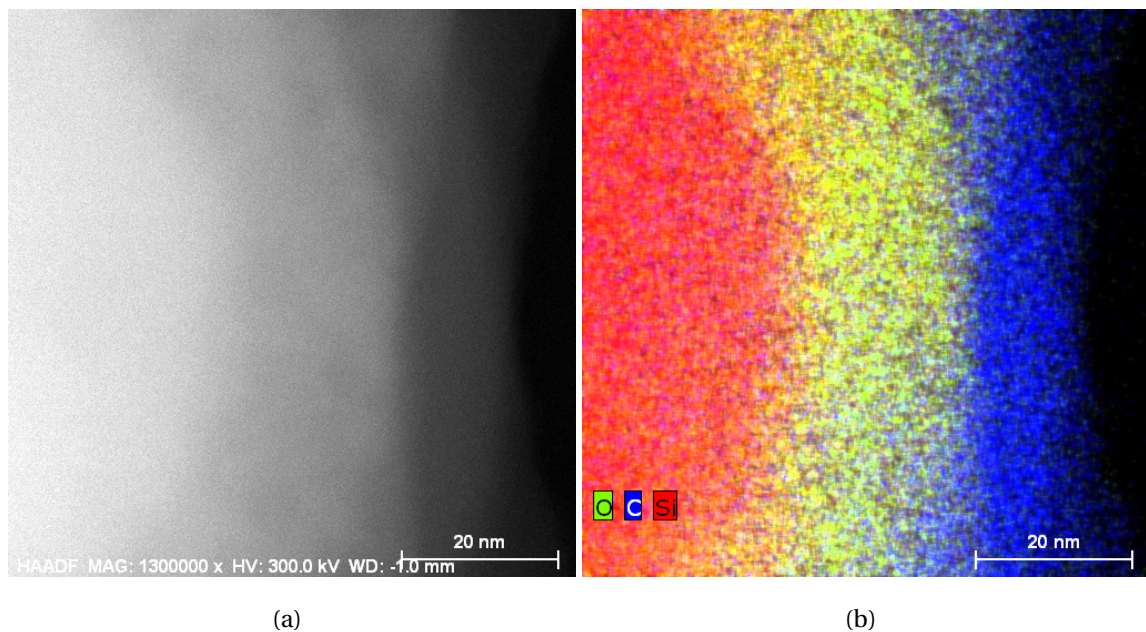


**Figure 4.33:** TEM micrograph of Si@SiO<sub>2</sub>@C with corresponding EDS-map. The TEM was operating by Asbjørn Ulvestad with an acceleration voltage of 300 kV.

## 4.4 Final characterization of multiple core-shell particles

The SEM micrographs show larger agglomerated oxide coated silicon particles, covered in web of carbon. The morphology of these structures do not look like the core-shell particles earlier discussed, and the secondary particle structure may be described as multiple core-shell particles, as one or more agglomerates are incorporated into the same carbon coated structure.

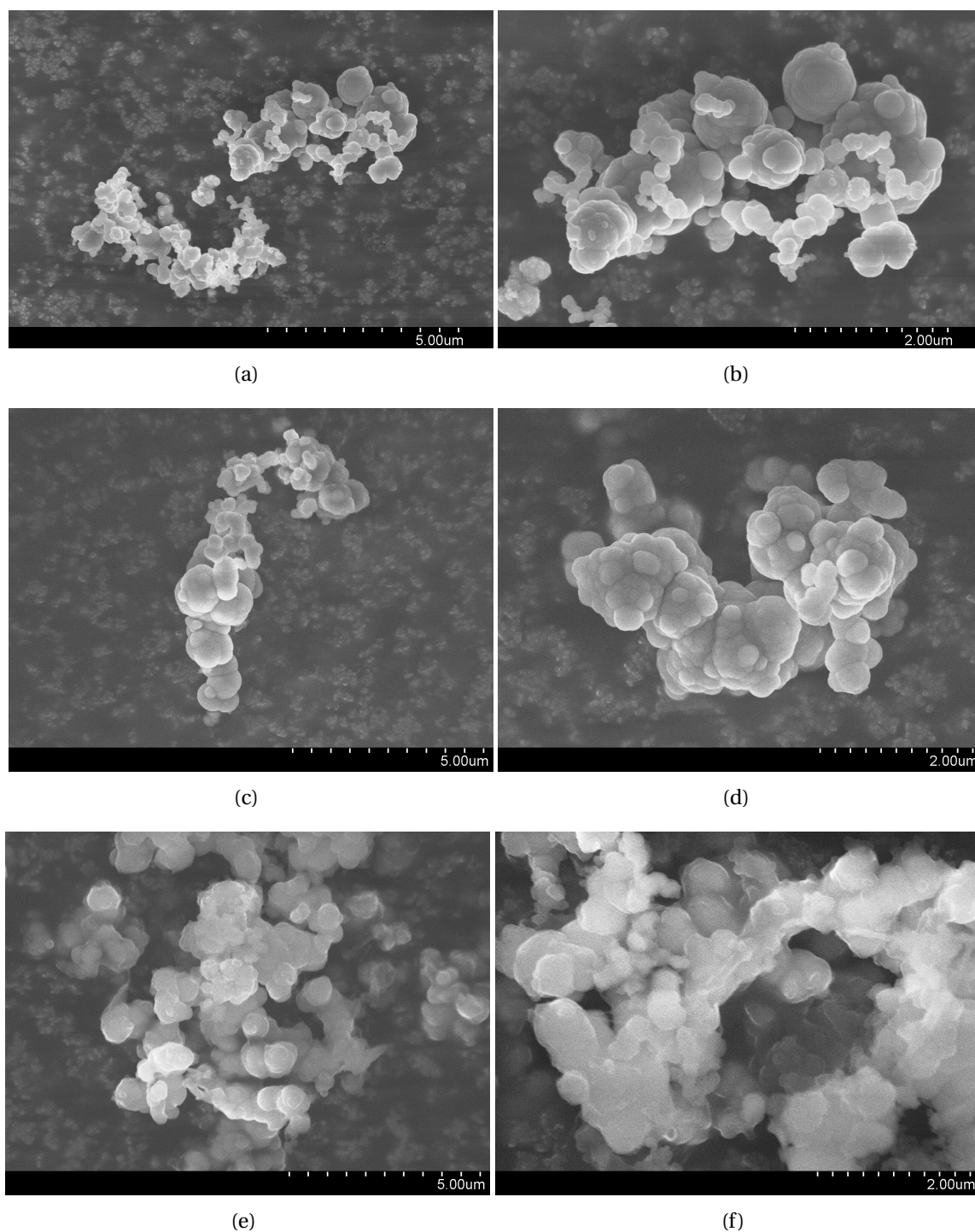
### 4.4.1 Material properties

SEM images of particles before and after both coating steps can be seen in Figure 4.34, and shows that the deposited oxide has interconnected some previously single particles or agglomerates, as well as a web-like carbon coating forming secondary particles.

EDS measurements were done in the SEM to qualitatively verify an increase in oxygen and carbon content following the respective coating procedures, as well as uncover possible impurities that may have appeared during coating. The resulting wt% and at% for the amorphous Si reference, core-shell Si@SiO<sub>2</sub> and multiple core-shell Si@SiO<sub>2</sub>@C can be seen in Table 4.8.

The oxygen content was not measurable in the reference, and therefore all oxygen seen in the core-shell or double core-shell particles are assumed to be due to oxide coating or independent silica spheres found in the mixture after coating by TEOS. An atomic percent of 14% was seen for core-shell Si@SiO<sub>2</sub> and 13% for multiple core-shell Si@SiO<sub>2</sub>@C (RF03). The oxygen content in RF02 is lower than RF03, which is probably due to a lower amount of ammonia used in its fabrication (see Table 3.1) and therefore a thinner oxide coating.

The carbon content seen in the Si reference can be attributed to the carbon tape used for adhesion to the SEM stub as well as carbon impurities found in the chamber. This carbon impurity will also be seen in the core-shell and double core-shell particles, and therefore the approximate C-content in RF02 and RF03 was found to be 3 at% and 67 at%, respectively.

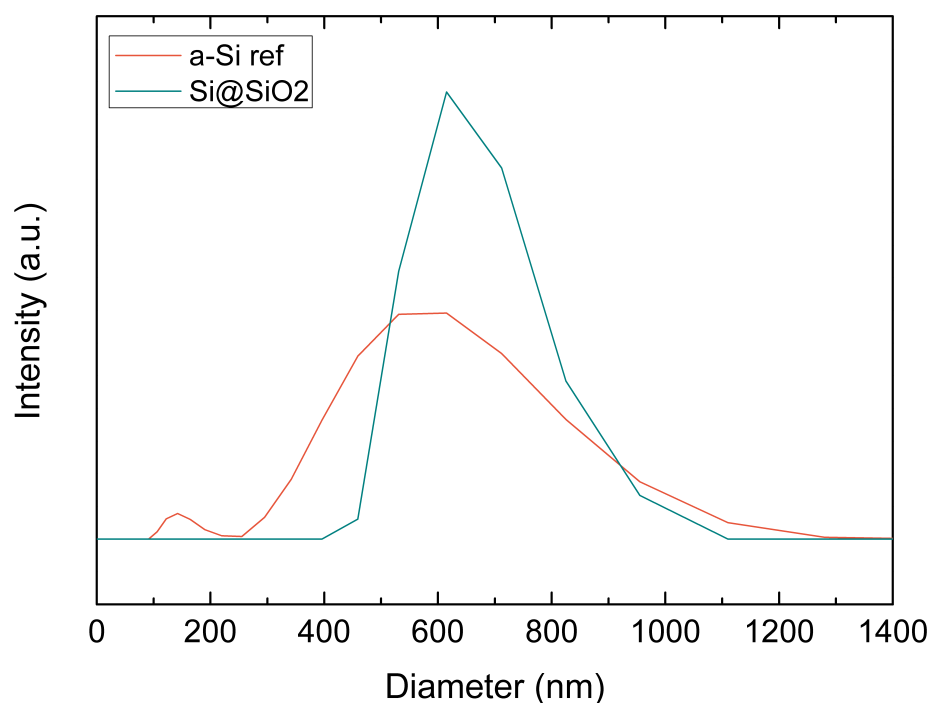


**Figure 4.34:** SEM micrographs of all powders: (a)-(b) Si, (c)-(d) core-shell  $\text{Si@SiO}_2$  and (e)-(f) multiple core-shell  $\text{Si@SiO}_2\text{@C}$ . The SEM was operating at (a)-(d) 6 kV with WD of 4 mm or (e)-(f) 15 kV with a WD of 5 mm.

**Table 4.8:** EDS measurements before and after oxide and carbon coating. Numbers are rounded to nearest whole number as they are used for qualitative verification of elements.

Element	Si		Si@SiO <sub>2</sub>		Si@SiO <sub>2</sub> @C			
	a-Si ref		TEOS08		RF02		RF03	
	wt%	at%	wt%	at%	wt%	at%	wt%	at%
Silicon	96	91	73	57	90	81	21	11
Oxygen	-	-	10	14	4	7	15	13
Carbon	4	9	17	29	6	12	64	76

DLS analysis uncovered that all of the powders were very polydisperse, with Pdi's of 0.57 for a-Si ref and 0.85 for Si@SiO<sub>2</sub>. The analysis of Si@SiO<sub>2</sub>@C-powder gave inconclusive and unrepresentative results (Pdi close to 1), and is therefore not plotted. The analysis gave hydrodynamic diameters of  $590 \pm 170$  nm for a-Si ref, and  $610 \pm 110$  nm for Si@SiO<sub>2</sub>.

**Figure 4.35:** DLS particle size distributions by intensity.

Surface area measurements from BET analysis of a-Si ref, core-shell Si@SiO<sub>2</sub> and multiple core-shell Si@SiO<sub>2</sub>@C are shown in Figure 4.36 and Table 4.9. The amorphous reference silicon did not contain any micropores ( $\leq 2$  nm in diameter), indicating that the entire BET surface area is external. There is a large increase in surface area for the oxide coated silicon, where almost 80% of this is attributed to micropores. An increase in external area and decrease of micropore area was seen for the carbon coated particles, and 30% of its total area was attributed to micropores.

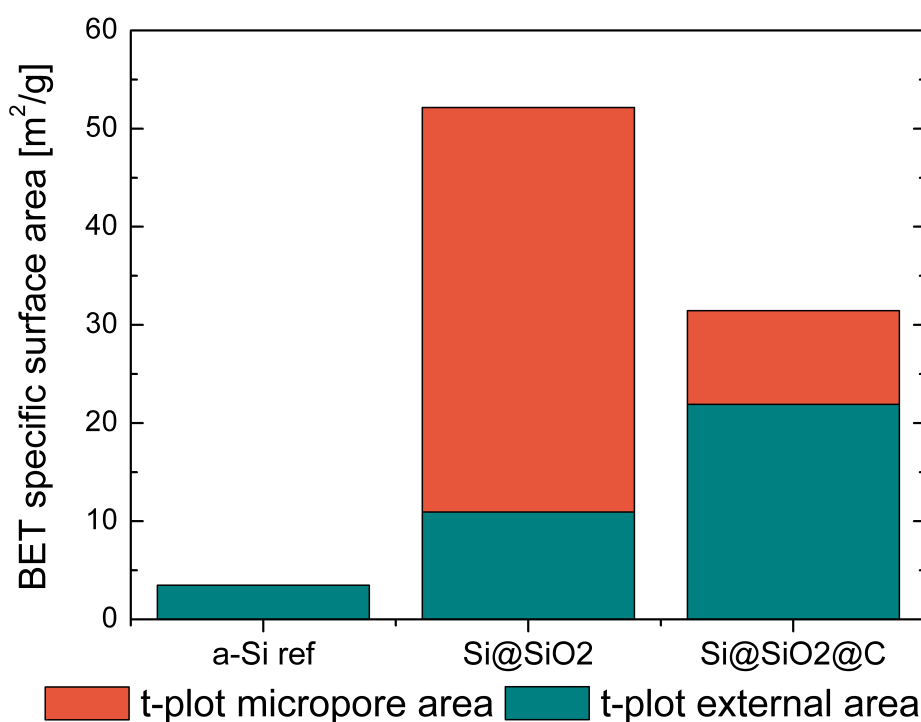


**Figure 4.36:** BET surface area with micropore and external area specification.

**Table 4.9:** BET surface area measurements of a-Si ref, Si@SiO<sub>2</sub> and Si@SiO<sub>2</sub>@C. Values are rounded to nearest hundredth and divided into micropore and external surface area.

Area [m <sup>2</sup> /g]	a-Si ref	Si@SiO <sub>2</sub>	Si@SiO <sub>2</sub> @C (RF03)
BET surface	3.10	52.16	31.45
t-plot micropore	-	41.23	9.55
t-plot external	3.48	10.93	21.90

### 4.4.2 Crystallinity

XRD diffractograms of all carbon coated batches (RF01-RF05) can be seen in Figure 4.37, and shows varying crystallinity for the different batches. Both RF01 and RF03 are amorphous after heat treatment, while RF02, RF04 and RF05 have all crystallized. Characteristic silicon peaks can still be seen in all samples at  $2\theta = 28^\circ$ ,  $47^\circ$  and  $56^\circ$ . The difference in intensities for the crystalline samples is mainly due to the amount of powder used.

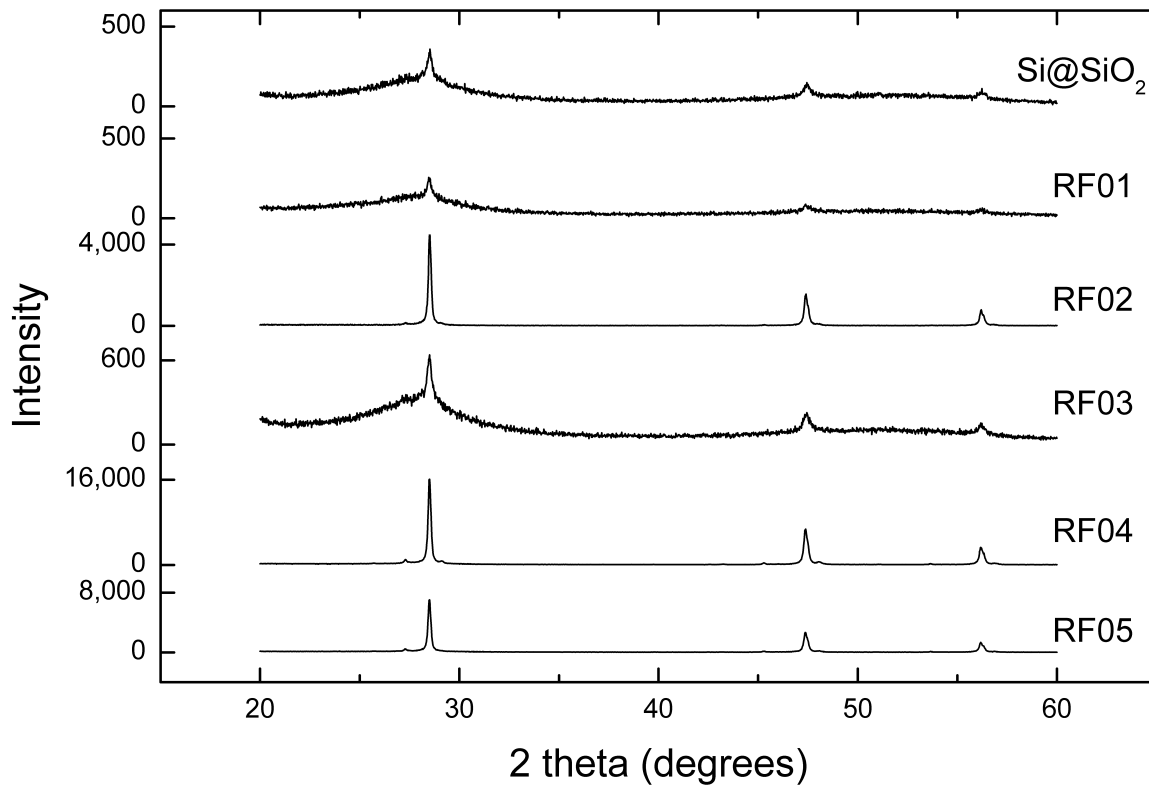


**Figure 4.37:** XRD diffractograms of Si@SiO<sub>2</sub>@C batches RF01-RF05.

### 4.4.3 Carbon content

Thermogravimetric analysis was done on all RF-samples, and the resulting mass loss curves can be seen in Figures 4.38 and 4.39, and the results summarized in Table 4.10. The amount of carbon in each sample is determined by calculating the mass loss between 250 and 600°C, as this loss is due to burn-off of carbon in a synthetic air mix. The carbon-content is found to be 6.7 wt% and 12.7 wt% for the two amorphous samples, RF01 and RF03 respectively. No characteristic drop in mass was found for the crystalline samples RF02, RF04 or RF05, which confirmed the suspicion from SEM and EDS analysis that the carbon coating had not been successful. At temperatures higher than 600°C a mass increase is seen, which is attributed to the oxidation of silicon.

**Table 4.10:** Carbon content of all Si@SiO<sub>2</sub>@C batches, and failed RF-batches. Mass loss measured between 250 and 600°C.

Active material	Carbon content [wt%]
RF01	6.7
RF02	-
RF03	12.7
RF04	-
RF05	-

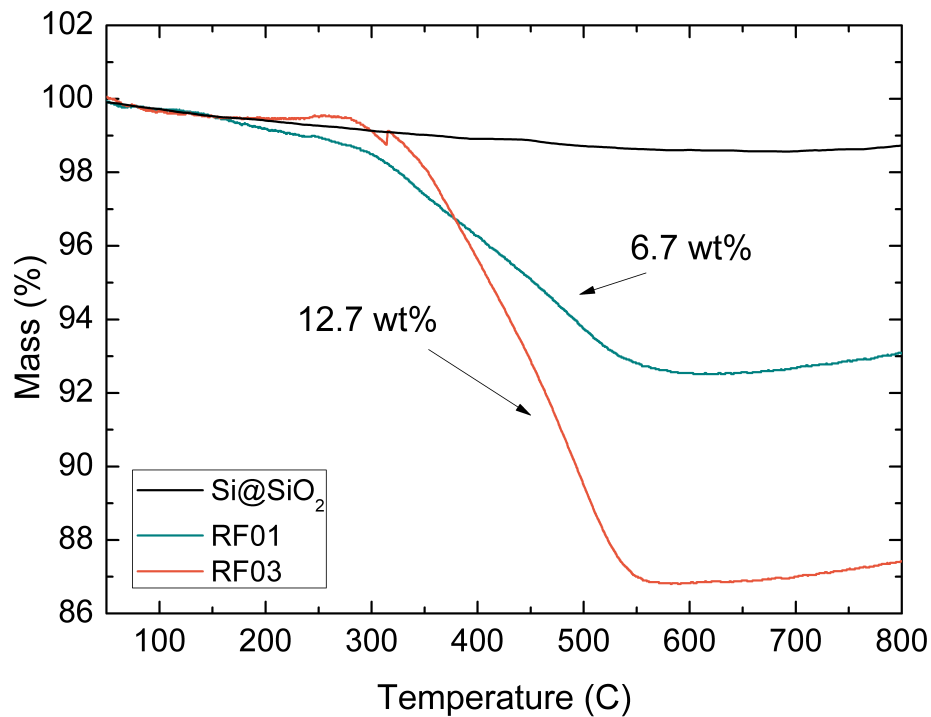


**Figure 4.38:** Thermogravimetric mass loss curves for the RF-batches RF01 and RF03. Also a curve from Si@SiO<sub>2</sub> is shown for reference.

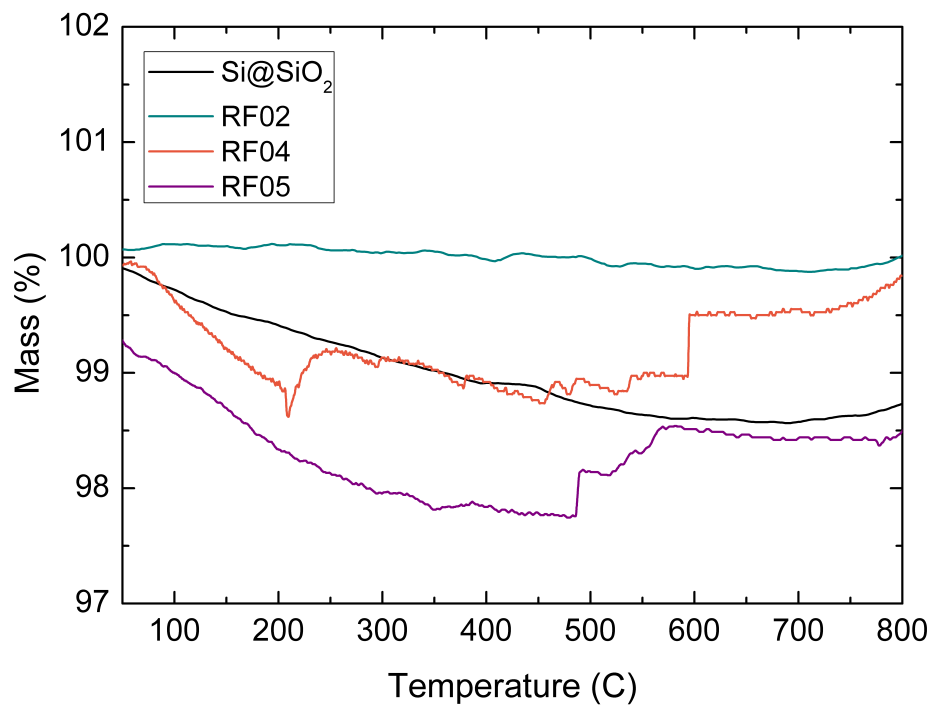


**Figure 4.39:** Thermogravimetric mass loss curves for the RF-batches RF02, RF04 and RF05. Also a curve from Si@SiO<sub>2</sub> is shown for reference.

# 5 Discussion

---

This section aims at discussing the results found in Section 4, and determining how these results can be used to verify the aims of this work. Amorphous and crystalline silicon was characterized and cycled to determine whether or not its initial crystallinity would have an effect on the final electrochemical performance of the particles, and no significant difference was found when cycled. Some minor variations were seen in their morphology, and electrochemical differences regarding loading and fabrication of the half-cells were also seen, and both will be discussed in the following sections.

The coating procedures used for oxide and carbon coating have been investigated and characterized at different steps in the synthesis procedure. The oxide coating was found highly reproducible and somewhat controllable, while issues regarding the pH of the solution and formation of silica spheres will be discussed. The carbon coating step was not found reproducible in the work done for this thesis. Different variables in the RF coating procedure have therefore been investigated in order to determine where the process has failed.

## 5.1 Pure silicon reference

### 5.1.1 Material properties

The as-fabricated particles were found to be amorphous, highly agglomerated and aged, between 50 nm and 1  $\mu\text{m}$  in diameter with the majority of primary particles within  $200 \pm 100$  nm, and a BET specific surface area of  $3 \text{ m}^2/\text{g}$  including no measurable micropore area. Most of these properties are found to be beneficial for silicon in Li-ion batteries, as nanoscale particles are believed to buffer some of the volume change of silicon by uniformly distributing stress throughout the particles, increasing volumetric energy density, and shortening lithium diffusion paths [81]. Nanoparticles below 150 nm have even been found to not crack at all during the first lithiation cycle [82]. Most studies of silicon revolve around monodisperse particles, although here the particles are highly polydisperse, and agglomerated.

### Surface area

A small BET surface area limits SEI formation and consumption of  $\text{Li}^+$  -ions, and thereby also irreversible capacity loss. The characteristic effect of nano-scaling is a large increase in surface to volume ratio, and if all the particles were perfect spheres with a diameter of 200 nm, a surface area of  $13 \text{ m}^2/\text{g}$  should have been measured. However, the small surface area seen here is most likely due to the extent of agglomeration, which was also observed in SEM. The primary particles are nanosized and show a spherical nature to some extent, but due to ageing and agglomeration (assumed to be from fabrication of the particles in the reactor), not all of the surface area is available for reactions. This agglomeration effect also limits the reliability of particle diameters measured by DLS, although the analysis gave particle diameters only slightly larger than measured in SEM. This is most likely due to DLS measuring the hydrodynamic diameter, but could also be due to agglomeration in solution. The conditions for producing monodisperse and non-agglomerated particles in the FSR is still an ongoing project at IFE.

After crystallization, no significant change in morphology is seen. The samples exhibit similar sizes and extents of agglomeration, while a small micropore area of  $0.19 \text{ m}^2/\text{g}$  was in fact seen in BET analysis of c-Si ref. As this only constitutes 5% of the total BET specific surface area, it may be disregarded due to insecurities in the method itself, but may also be due to the ethanol solvent used in the crystallization procedure. All ethanol is assumed to have evaporated before the decomposition temperature is reached, but this may not be true, and could lead to some amorphous, microporous carbon as ethanol is a carbon precursor.

### Possible carbon content

TGA results also varied slightly for the two powders, where a small mass loss of 0.3 wt% was seen for c-Si ref, while no stable mass loss was observed for a-Si ref.<sup>1</sup> The small mass loss in c-Si ref could be due to the amorphous carbon previously mentioned. However, these values are still small and may be attributed to insecurities in the method itself. In TGA an alumina crucible is used for holding the material, and if not completely clean, old material may be burnt off and contribute to the mass loss.

---

<sup>1</sup>All mass loss before  $250^\circ\text{C}$  is expected to be due to evaporation of moisture.

## Crystallinity

XRD however did show a large difference in the two powders, as one is clearly mostly amorphous and the other is highly crystalline. But, a-Si ref did show signs of slight crystallization in the form of small peaks at characteristic  $2\theta$ -angles for Si. This is thought to be due to larger Si chunks found in the powder mixtures, and these structures could be seen in Figure 4.6. These larger particles may be crystalline, and therefore influence the initial electrochemical cycling of a-Si ref, but is discussed more thoroughly in the following section.

In conclusion, the differences found between the two materials are very small, and none of the structural or chemical parameters observed for amorphous and crystalline Si is expected to influence the electrochemical results noticeably, except for possibly the crystallinity in itself.

### 5.1.2 Electrochemical analysis

The influence of crystallinity in initial electrochemical cycling is a highly investigated field, and it is well-known that during the first lithiation of crystalline Si there is a two-phase region due to the conversion of crystalline silicon to partially lithiated amorphous silicon. This two-phase region remains until about 50 mV, while below this the amorphous silicon suddenly crystallizes into  $\text{Li}_{15}\text{Si}_4$  [36]. The cut-off voltage of electrochemical cycling is therefore in this work chosen to be 50 mV to avoid this crystallization-phase. The amorphization of crystalline silicon during the first de-lithiation is often linked to entrapment of  $\text{Li}^+$ , thereby making them unavailable for continued cycling and the cells may show a higher irreversible capacity loss.

#### Initial lithiation

Some differences were observed during the initial cycling of both Si reference materials, and these will be explained with help from lithiation reactions proposed in [44]. Here, two different lithiation mechanisms were proposed for a-Si and c-Si material, where the amorphous lithiation proceeds gradually while crystalline material is amorphized and lithiated by several steps. As seen in Figure 4.12, this effect was present in limited cycling, where it was observed that the crystalline samples had a formation period of up to 30 cycles before stable cycling was seen at 1,200 mAh/g. This formation period was correlated with loading, as a higher loading resulted in a longer formation time. It was

also observed in the voltage plots, where 1,200 mAh/g was reached at a potential of 0.16 V for c-Si ref, 0.07 V lower than for a-Si ref (0.23 V). This lower potential was needed to be able to lithiate to the same capacity, as shown in Figure 5.1, a subset of the voltage plots for the first cycle (Figure 4.14).

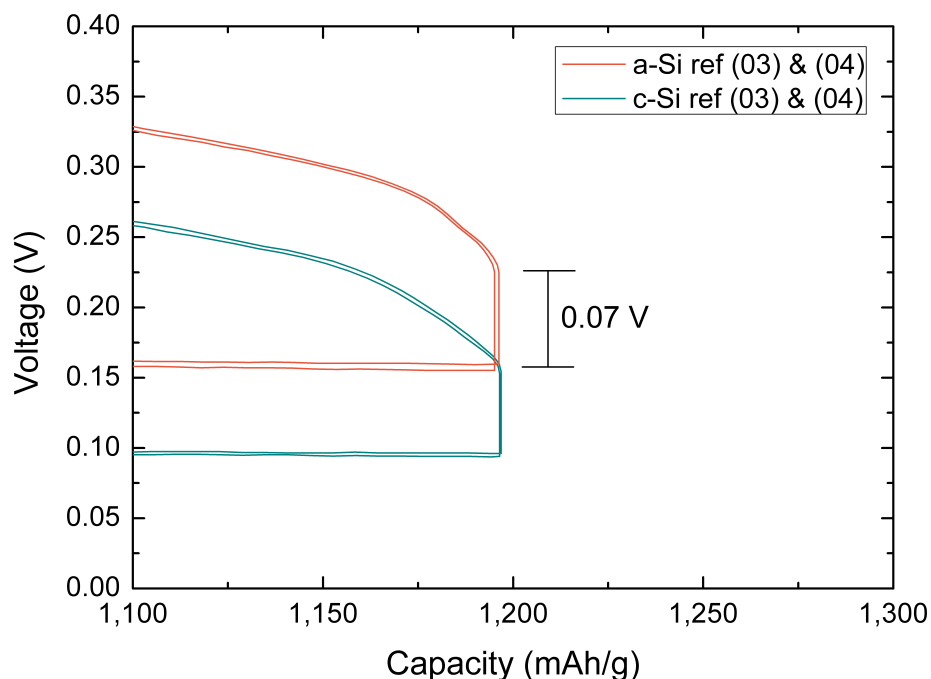


**Figure 5.1:** A subset of voltage plots from Figure 4.14, showing a polarization of the first lithiation reaction for c-Si ref.

The  $dQ/dV$  plots show the polarization as a shift of the first lithiation reaction, and a low potential of 0.09 V was needed to initiate the first lithiation in c-Si ref compared to 0.18 V needed for the amorphous Si. This polarization of 0.09 V can be seen in Figure 5.2, a subset of the  $dQ/dV$  plot for the entire first cycle (Figure 4.15). This polarization is also reflected in the impedance measurements, and a higher charge transfer resistance was actually observed for crystalline silicon ( $\Delta R_{CT}=0.9$  Ohm at 50% SOC and  $\Delta R_{CT}=1.8$  Ohm at 100% SOC).

However, differential capacity analysis also revealed that the materials seem to proceed along the same lithiation reactions after the initial cycle.

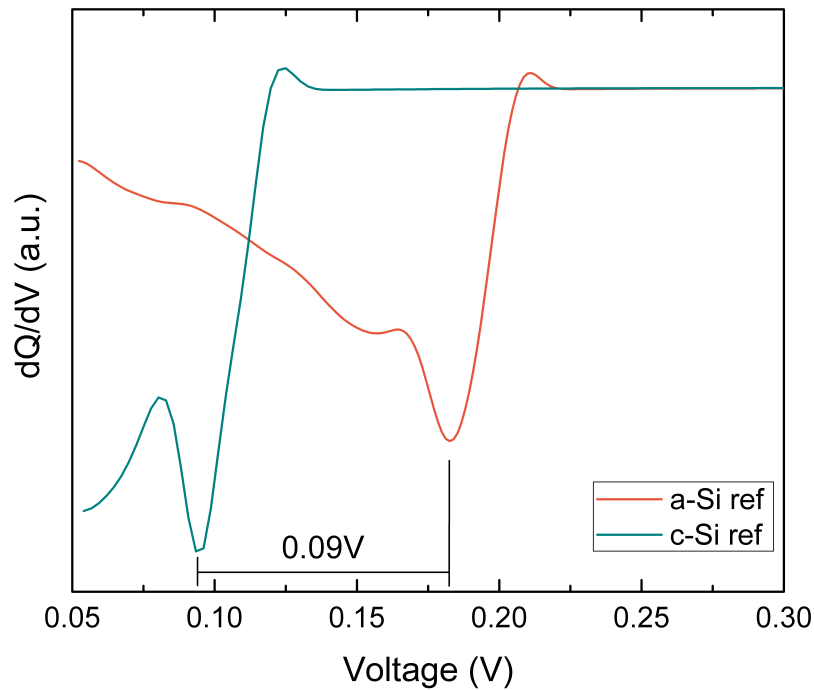


**Figure 5.2:** First lithiation peak of Si reference. Shows a polarization of c-Si ref by 0.09 V.

Further analysis of the Nyquist plots (that do not relate to the difference between amorphous and crystalline silicon), revealed an increase in charge transfer resistance,  $R_{CT}$ , from 50 to 100% SOC for both materials. This is natural, as a higher lithiated structure will provide a higher resistance to more lithium. The other observation was a lower  $C_{dl}$  with higher SOC, meaning that there was less active surface area available at 100% SOC than at 50% SOC. This can be explained by the volume expansion of silicon during lithiation, and the resulting higher packing density of the particles.

### Loading of active material

A high areal capacity loading is needed for anodes to be commercially viable and meet demands for high energy density based on total cell weight or volume. Anodes must meet a prerequisite of 2.0 mAh/cm<sup>2</sup> in areal loading to be commercially viable, but this high loading often causes the anode to suffer from severe capacity loss in the first cycles [59, 83]. The reason for this can be explained in the fact that a higher loading usually involves a thicker electrode, and the active particles are therefore increasingly distant from the current collector [84]. This effect will further enforce the concentration gradient observed during lithiation, and more uneven expansion of the electrode is seen when the loading is increased.

There is a small difference in mass loading of the cells cycled here, both amorphous and crystalline. All amorphous cells (01-04) and four crystalline cells (05-08) have a mass loading  $\sim 0.50$  mg/cm<sup>2</sup>, while the four remaining crystalline cells (01-04) have a lower mass loading of  $\sim 0.40$  mg/cm<sup>2</sup>. When multiplied by reversible capacity seen in cycles 20-50, the areal loading is found to be between 0.69 and 1.36 mAh/cm<sup>2</sup>, which is not commercially viable. An overview of their areal loading can be seen in Table 5.1. This loading seems to have a significant effect on the cycling of the cells, as differences in lifetime are seen for both unlimited and limited cycling.

**Table 5.1:** Areal loading of Si reference cells cycled to unlimited capacity. The average capacity is determined by an average over the lithiation capacities between cycles 20 and 50.

Cell	Reversible capacity mAh/g <sub>Si</sub>	Areal loading mAh/cm <sup>2</sup>
a-Si ref (01)	1,970	1.02
a-Si ref (02)	2,057	1.09
c-Si ref (01)	1,767	0.72
c-Si ref (02)	1,723	0.69
c-Si ref (05)	2,507	1.28
c-Si ref (06)	2,658	1.36

First, for the unlimited cycling: All cells with a higher loading showed higher capacities, both initially and reversibly, but shorter lifetimes. Normally a lower capacity is seen for high loadings due to overpotential throughout the electrode, as the entire electrode isn't electrochemically active [83]. The higher loading (more active material) leads to increasingly rapid failure of the cells, as all four cells with higher loading lead to shorter lifetimes than the lower loading. More active material in the electrode leads to more pulverization, and less buffering from the CA.

Second, for the limited cycling: The higher loading of two c-Si cells (05-06) gave a longer formation time than the lower loading cells (01-02) before able to cycle at 1,200 mAh/g. This is understandable, as more active material requires a longer time for complete formation/amorphization. The four cells with highest loading (both amorphous and crystalline) also died at an earlier stage than the lower loading, explained by the fact that a thicker electrode causes higher variations in lithiation concentration. This leads to a more rapid decay of the active material.

### Irreversible capacity loss

Insecurities in values used to obtain an ICL were presented in Section 3.5. In spite of the insecurities and different cycling conditions (before and after calibration) the irreversible capacity losses seemed to show a dependence on crystallinity.

A large difference in ICL for unlimited cycling was observed, larger than could be accounted for by insecurities, where an ICL of 8-9% was seen for the crystalline reference, compared to 1% for the amorphous reference (highly unrealistic value). Furthermore, the capacity retention is as low as ~60% after only 10 cycles for reference material with a loading of ~0.5 mg/cm<sup>2</sup> and slightly higher, ~65% for the lower loading of ~0.4 mg/cm<sup>2</sup>, with no dependence on crystallinity. For use in commercial cells, the capacity retention must be much higher than this. Higher ICL in the crystalline cells was also seen for the cells cycled to a limited capacity, where an ICL of 12% was seen for a-Si ref and 15% for c-Si ref. This difference can be explained by the same factors as over, but since the capacities in limited cycling are lower, the variations due to an instabilities in the battery cycler are also smaller.

#### 5.1.3 Effect of heat treatment on electrochemical cycling

In crystalline materials, this capacity loss can occur due to the formation of new intermetallic phases upon lithium insertion, leading to inhomogeneous volume expansions in the two-phase regions and subsequent pulverization of the material [30]. This cracking will eventually lead to loss of electrical contact with the electrode, and capacity fade is seen as a result of this. Amorphous materials have been found to alloy more easily with Li<sup>+</sup>, as the amorphous structure provides more paths for insertion and extraction of lithium. The expansion of an amorphous alloy has also been seen to be more homogeneous and isotropic, and for thin films the capacity loss was assumed to be due to delamination and not pulverization of the film.

However, in this study crystallization of the material due to the carbon-coating procedure did not seem to have a significant effect on the electrochemical performance of the material. Reactions occurring in the materials lead to irreversible capacity loss in both amorphous and crystalline Si. The ICL may be due to amorphization of highly crystalline Si, SEI-growth, or more likely a combination of both. The cell assembly and loading did however have an effect on the performance, but the effect of loading is not investigated in this work.

## 5.2 Core-shell particles, Si@SiO<sub>2</sub>

The core-shell particles will be discussed with respect to a-Si ref, as the oxide-coating method does not result in a crystallization of the core material. A-Si ref will therefore be referred to as Si ref for the remaining of the upcoming section.

### 5.2.1 Material properties

There was a larger change in morphology noted after oxide coating, as the oxide interconnect particles and agglomerates and thereby effectively increases the particle sizes. This was noted in the SEM images where the PSD was centered around 600 nm, as well as the (slightly inconclusive) DLS results giving particle diameters of  $610 \pm 110$  nm. The particles are found to be even more agglomerated than the Si reference, likely due to the oxide coating.

#### High microporous surface area

Silica grown by the Stöber method is known to have a complicated interior fractal-type structure, resulting in a porous structure [85]. When investigating the surface area by nitrogen adsorption, 80% of the BET surface area of Si@SiO<sub>2</sub> was in fact attributed to micropores. Li<sup>+</sup>-ions have a Van der Waals ionic radius of 0.18 nm, but when in an electrolyte solution the calculated complex diameters for Li(EC)<sub>2</sub><sup>+</sup> and Li(EC)<sub>3</sub><sup>+</sup> are 0.89 nm and 1.07 nm, respectively, shown in Figure 5.3 [86]. These complexes are too large for micropores ( $\leq 2$  nm), and leads to an inaccessible microporous surface area showing poor electrochemical performance. Micropores in the active material should therefore be limited.

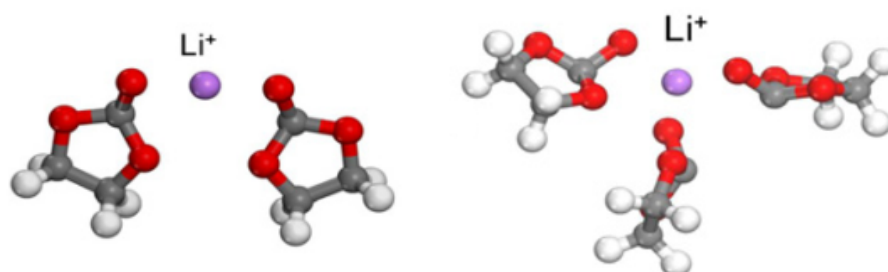


**Figure 5.3:** Lithium complexes in electrolyte solution. Original illustration appears in [86].

### Effect of pH on oxide coating

All of the observed micropore area is not expected to be from the oxide coating, as larger areas composed of homogeneously nucleated silica Stöber spheres (~50 nm) were found, as well as mixed within the SiNPs themselves, during the authors previous work [1]. These are assumed to be produced as a byproduct of the oxide-coating when the pH is high, and can be seen in Figure 5.4. As the oxide layer in the core-shell particles is a sacrificial layer which will be removed at a later stage, neither the micropores in the coating nor the silica particles are considered a problem. They might actually create a higher buffering void volume within the secondary particles, if evenly distributed amongst the Si@SiO<sub>2</sub>-particles themselves. As seen in a scheme in Figure 5.5, low pH promotes the formation of chains, while higher pH induces particle growth, or the formation of fractals.

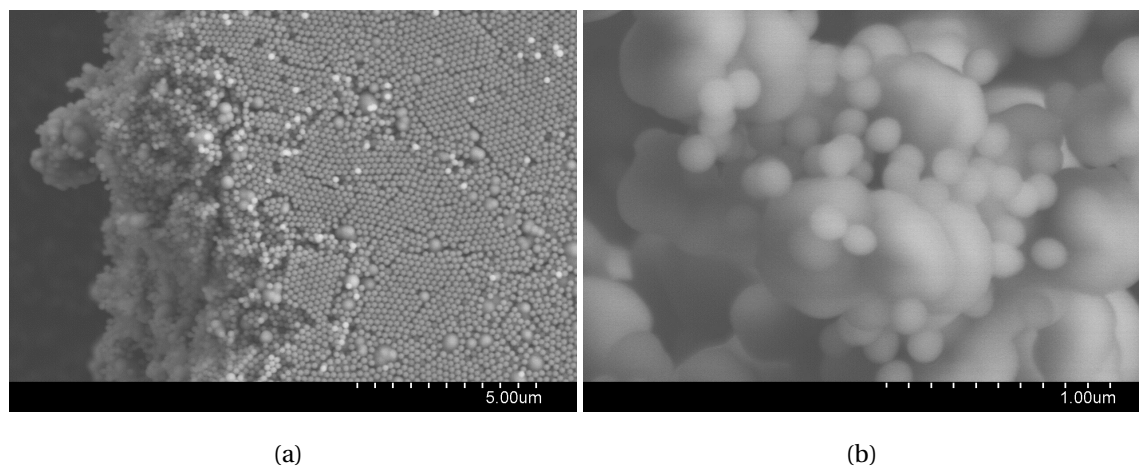


**Figure 5.4:** SEM micrographs from Skare [1], where an acceleration voltage of 5 kV and WDs of (a) 4 mm and (b) 16 mm were used.

A lower pH (less NH<sub>4</sub>OH in solvent) was tested to eliminate silica spheres during oxide-coating, while still induce coating in the form of a polymerized gel on the surface of SiNPs. This resulted in a lower oxygen content in EDS, and also a thinner oxide coating in TEM (seen in Figure 4.20 vs. Figure 4.21). It was therefore concluded that the silica spheres could be beneficial for the yolk-shell particles, and 1 ml of NH<sub>4</sub>OH was used per 100 mg Si under synthesis, giving an oxide coating thickness of 50-80 nm (Figure 4.21). The amount of catalyst (NH<sub>4</sub>OH) added for the particles observed in TEM is summarized per 100 mg Si in Table 5.2. TEOS04 and TEOS05 was seen in Figure 4.20 and particles from same synthesis parameters as TEOS08 was seen in Figure 4.21.

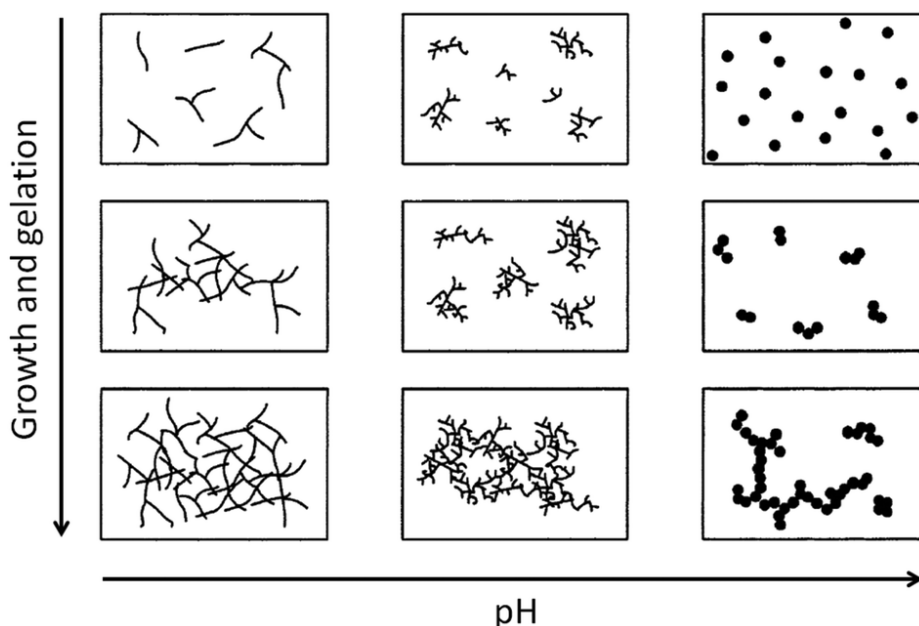


**Figure 5.5:** The effect of pH on silica-gel structure. Figure adapted from Cushing et al. [64].

**Table 5.2:** Oxide precursor and catalyst per 100 mg Si material.

Batch	SiNP [mg]	Ethanol [ml]	H <sub>2</sub> O [ml]	NH <sub>4</sub> OH [ml]	TEOS [ml]
TEOS04	100	80	20	0.5	0.4
TEOS05	100	80	20	0.5	0.4
TEOS08	100	80	20	1	0.4

### 5.2.2 Partial control of oxide coating

The oxide coating procedure was found to be controllable, while the silica spheres could not be removed while still inducing a thick enough oxide coating. However, after carbon coating and etching, these silica-spheres will be removed together with the oxide coating, and hopefully create more area for the Si to expand during cycling, so they are not considered a problem. The micropores may however lead to problems related to entrapment of Li<sup>+</sup> when electrochemically cycling the Si@SiO<sub>2</sub>-anodes.

### 5.2.3 Electrochemical analysis

As the oxide coating is a sacrificial coating, its electrochemical performance is not considered to be of high importance in this thesis. Its impedance results however may provide insight to the characteristics of the coating, and will be discussed (although not in

detail). Note: The active material in Si@SiO<sub>2</sub>-anodes is not compensated for the oxide coating, meaning that the loading is based on weight of Si@SiO<sub>2</sub>, not only Si.

### De-activation of active material

Cells cycled with Si@SiO<sub>2</sub>-anodes did, as expected, show exceptionally bad electrochemical performance, most likely due to the large micropore area and entrapment of Li<sup>+</sup> during the first cycle. The coating of Si with an oxide layer from TEOS has however been done by others [87] to improve battery performance (often followed by a carbon coating), but the thickness of these coatings was much thinner than the oxide coatings applied here.

Shown in Figures 4.24 and 4.23 a first cycle capacity of ~1,200 mAh/g was seen for all half-cells, showing that an initial lithiation of active material took place. This was also seen in dQ/dV plots of the same cycle (Figure 5.6, a subset of Figure 4.26), where the first lithiation peak of Si@SiO<sub>2</sub> was seen at 0.13-0.10 V. The first cycle lithiation peak for Si ref however, is seen at a higher potential of 0.18-0.16 V, and this shift in potential could be due to a polarization of the Si@SiO<sub>2</sub> anode, but may also be due to a conversion reaction converting Si@SiO<sub>x</sub> to a lithiated Si phase [88].

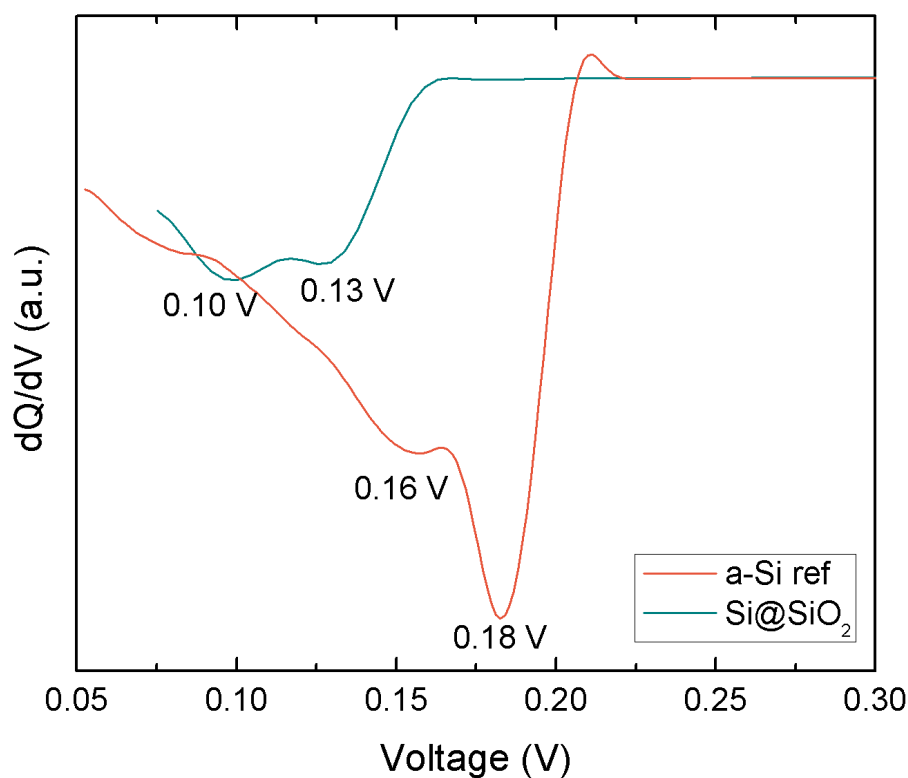


**Figure 5.6:** First lithiation peaks of Si@SiO<sub>2</sub> and Si ref, a subset of Figure 4.26.

Characteristic de-lithiation peaks were also seen at  $\sim 0.27$  V and  $\sim 0.47$  V, only these were wider than what is normally seen for Si, which could be a sign of de-lithiation of  $\text{SiO}_x$ . The second cycle also displayed characteristic lithiation and de-lithiation peaks at potentials close to what is seen for Si ref, and some capacity was still observed. However in the third cycle, a low activity was seen all over when comparing the differential capacity curves to Si ref. This rapid decay in capacity was also visible in voltage plots for the first 10 cycles seen in Figure 4.25.

High capacity degradation can also be seen in the Nyquist plots from GEIS. These cells were cycled twice for formation purposes before GEIS was measured at an expected 50% SOC and 100% SOC. This SOC is expected by lithiating the material for 2.5 h at C/5, but the current applied is determined by the assumed capacity of the cell based on amount of active material. The  $\text{Si@SiO}_2$  powder however, is not highly active any longer after two formations cycles, and are expected to reach maximum capacity within the first 2.5 h lithiation. 50% SOC is therefore actually being more likely 100% SOC. This is reflected in the Nyquist plots, as the impedance barely changes after lithiation for 2.5 more hours. The low electrochemically active area is reflected in the  $C_{dl}$  of  $25e-6$  F, about half of the value obtained for Si ref ( $55e-6$  F) at 50% SOC. This may be an effect of different loadings, as the loading of  $\text{Si@SiO}_2$ -anodes is based the weight of Si and oxide, not only Si. However, the total amount of  $\text{SiO}_2$  compared to Si in the system is not expected to be high enough for the increase to be solely due to the difference in loading.

The de-activation is likely due to entrapment of  $\text{Li}^+$  in the structure, and this theory is further supported by a higher resistance to diffusion into the particles (higher  $Z_W$ ) seen for  $\text{Si@SiO}_2$ .

### 5.3 Double core-shell particles, $\text{Si@SiO}_2@\text{C}$

Several batches of resorcinol-formaldehyde resins (RF) were tested for carbon-coating of  $\text{Si@SiO}_2$  core-shell particles, and the process has been noted as "convenient", "efficient" and "scalable" by Gan et al. [66]. However, using procedures based on work done by Liu et al. [15], carbon-content was only confirmed by TGA in two out of five samples. Even for these two samples fabricated with the same amount of precursor to  $\text{Si@SiO}_2$ -particles, the carbon-content varied from 6.7 wt% to 12.7 wt%. This large variation may be due to several factors, and will be discussed here.

### 5.3.1 Material properties

A SEM micrograph of Si@SiO<sub>2</sub>@C can be seen in Figure 5.7, together with an illustration of the final secondary particle morphology. It is clear that due to the agglomerated nature of the SiNPs, a double-core shell structure (as shown in Figure 1.2) was not obtained on single particles but rather around agglomerates. This encapsulation of agglomerates and silica spheres may leave some voids, which could be favorable to accommodate the volume expansion during cycling.

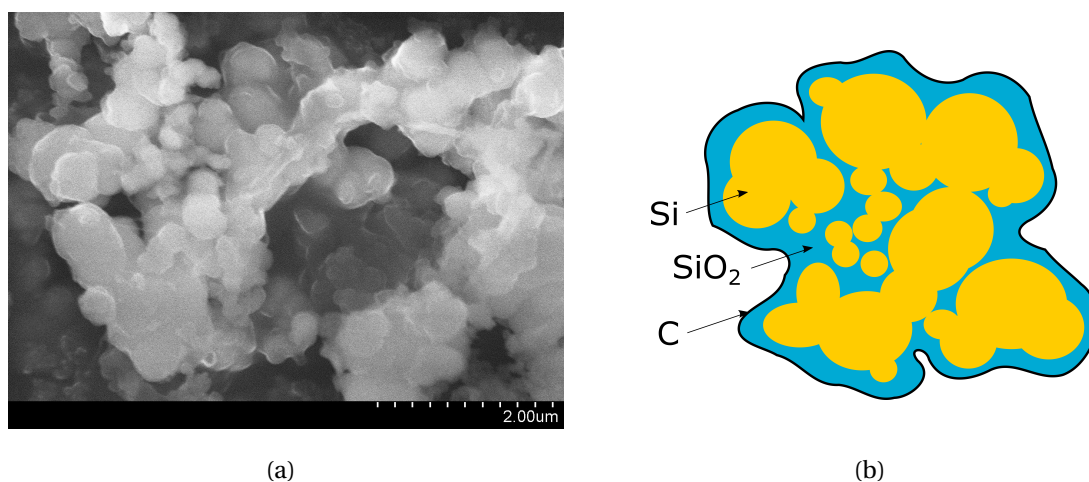


**Figure 5.7:** Multiple core-shell particles: (a) SEM micrograph and (b) illustration of the web-like nature of the secondary particles.

These secondary particles could actually be a feasible way to take advantage of agglomerated or chain-like Si, which is often seen in gas phase synthesis [89]. The secondary structure seen here may behave in the same way as the microbeads fabricated by Liu et al. [15], reducing the problems associated with high surface area nanostructures. The reasonably low surface area of 31 m<sup>2</sup>/g seen for Si@SiO<sub>2</sub>@C-particles will contribute to less side reactions with the electrolyte, and thereby also decreasing the ICL. On the other hand, around 30% of the specific surface area was attributed to micropores, which may be a combination of the microporous silica spheres, but also porous nature of the carbon coating. These micropores are however most likely not a problem, as the silica will be removed in further work.

### 5.3.2 Properties of carbon coating

The Si@SiO<sub>2</sub>@C secondary particles were investigated by TEM and EDS, see Figure 4.33, where the carbon coating thickness of RF03 was found to be 10-14 nm. This is similar

to the thickness observed by Hashem et al. [54], where  $\text{LiNi}_{0.5}\text{Mn}_{0.5}\text{O}_2$  was coated by dry mixing with sucrose and pyrolyzed. The coating was observed by TEM in several different areas, and exhibited good homogeneity, although this may not be the case for the entire batch. Thickness, homogeneity and conductivity of the carbon coating are important factors for improving the electrochemical performance of Si, and the coating should be thick enough for mechanical stability, as well as provide a diffusion pathway for both HF (for etching of the oxide) and  $\text{Li}^+$ -ions.

Too little carbon content will not provide sufficient conductivity and mechanical stability, while a too high content will lead to low electrode density [50]. Furthermore, thinner carbon will increase the specific capacity, while increasing irreversible capacity loss due to amorphous carbon having a certain percentage of dangling bonds, which will readily react irreversibly with  $\text{Li}^+$  at low potentials. The conductivity is highly dependent upon the thermal treatment temperature (T) as well as carbon sources, where a low T provides amorphous and low conductive carbon, but high T may reduce the substrate materials.

### **Precursor concentrations**

For the weight ratio of resorcinol/formaldehyde/Si@SiO<sub>2</sub> (2:1:5) used in coating RF01 and RF03, a carbon content of 6.7 wt% and 12.7 wt% was found by TGA in this work. Using the same coating procedure, Liu et al. [15] saw 23 wt% carbon. In spite of the difference in wt%, the carbon thickness was determined from TEM images to be 10-14 nm in this work, while the same amount of precursor gave a thickness of 6.5 nm in [15]. The reason for the differences in thickness may be due to the size and morphology of the particles that are coated, as Liu et al. carbon coated secondary particles (microbeads) with diameters between 1  $\mu\text{m}$  and 10  $\mu\text{m}$ . The carbon was however seen to infiltrate this secondary structure, and due to progressive polymerization and diffusion of RF through gaps in the structure, an RF resin coated both the inside and outside of the particles. Figure 5.8 illustrates the proposed carbon coating of the microbeads.

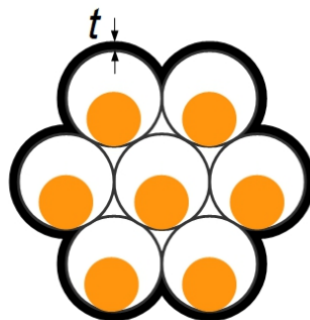


**Figure 5.8:** Schematic of carbon coating for microbeads/pomegranate structure. Original illustration appears in supplementary work from [15].

So, the same weight ratio between precursor and particles showed a lower carbon content in this work, while still showing a thicker carbon coating on the outer area of the secondary particles. Even though the microbeads had a larger average diameter than the multiple core-shell particles in this work, the available surface area for coating was still larger due to the primary particles being  $\sim 80$  nm in diameter, leading to a thinner coating with the same amount of carbon precursor. The lower carbon content found in TGA however, may be due to an insufficient polymerization time used in this work, leading to RF precursors left in solution during washing and therefore lost after centrifugation, and will be discussed further in "gelation and curing".

The large difference in C-content between RF01 and RF03 is however more unclear, but may have been influenced by general insecurities in the weighing of precursors and catalysts, as well as differences in polymerization time between the two batches.

### Cationic surfactant

The use of CTAB during the sol-gel process was found to be an important factor for the polymerization of RF resins, as both the surface and the RF precursors carry negative charges preventing its nucleation on these surfaces. Fang et al. [90] and Gan et al. [66] both saw that when CTAB was not present in the synthesis, no polymerization of RF was seen at all. CTAB plays two important roles, namely (i) promoting the polymerization of RF at low concentrations and (ii) inducing the spontaneous deposition of RF resin onto the surface of the Si@SiO<sub>2</sub>-particles. The effect of CTAB concentration was tested in this work, and by adding 10 mM of CTAB to 50 mg of Si@SiO<sub>2</sub>-particles a positive zeta-potential was seen, well in line with findings in [66].

### Gelation and curing

The main factor of the gelation step is the "catalyzed, endothermic, polycondensation polymerization reactions of the precursors under controlled conditions", to form the polymer coating by the crosslinking of polymer particles and chains [68]. The gelation time is very dependent upon pH and temperature, but as pH has not been recorded in this work it will only be mentioned here as a factor (The pH of  $\text{NH}_4\text{OH}$  used was 11.7). When using water as a solvent, which has been done here, the gelation is expected to occur after one day if the initial solution pH is higher than 7.0. The gelation can also occur more rapidly with high reactants densities, lower (or higher) pH or at higher temperatures. Figure 5.9 shows the gelation time as a function of pH. The temperature was in this work kept at RT for the entire gelation process, and the gel may therefore not have been stable enough when washed and carbonized.

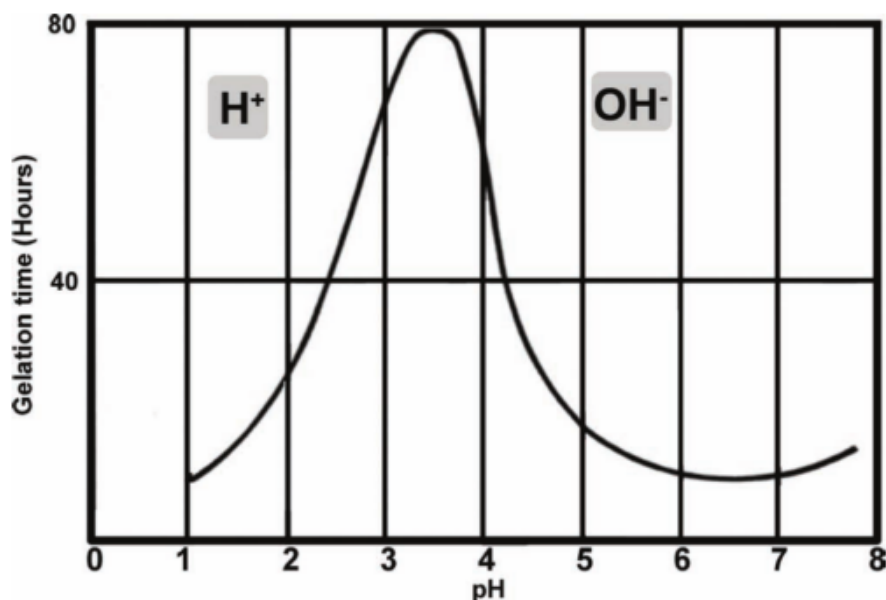


**Figure 5.9:** Resorcinol-formaldehyde gelation time versus pH. Original illustration appears in [91].

As the synthesis-route is very sensitive to polymerization time, this may have had a larger effect on the carbon-coating than initially expected. All batches have been left to polymerize over night, but the exact polymerization time may have varied between 16 and 20 hours. The polymerization time of three phenols was investigated by Liang and Dai [92] in 2006, where resorcinol was found to polymerize (by self-assembly in RT) in one week. RF resins were found to polymerize at RT in 20 hours by Fang et al. [90], but this time will vary for the solvents used, temperatures and other factors. It may however be an indication that the time used in this work was too short for complete polymerization.

### Carbonization treatment

Variations in the pyrolysis conditions can cause noteworthy changes in the properties of the carbon-coating, as the electrical conductivity of the sample increases significantly during this transformation [93]. Carbonization normally occurs within the range of 500 to 900°C, for 0.5 to 3 hours in an inert atmosphere [90]. An increase in temperature above 600°C can lead to a reduction in oxygen content, surface area and pore volumes and electrochemical double layer capacitance, as well as increasing macropores [94, 95]. RF gels may not even be electrically conductive unless carbonized above 800°C [96]. With these factors in mind, the program chosen for this work included one hour of Ar-flow at RT before the tube furnace was heated at 5°C/min up to 800°C where it was kept for two hours. These conditions should be ideal for carbonizing the RF resin in an inert atmosphere.

Nevertheless, varying crystallinity was found when investigating the RF-batches by XRD, which means that not all samples underwent the same transformation during the heat treatment. The heat treatment at 800°C was found to crystallize reference Si, while the Si core remained amorphous for the two successfully carbon-coated batches, RF01 and RF03. The remaining RF-batches that showed no sign of carbon were however crystallized. A simple possibility for the varying crystallinity is due to a failure in the oven itself. Some instances of the oven not heating up at all were observed by the fact that the ethanol used for washing was still present in the crucible after the program supposedly had run. This problem could easily be solved by using a more stable oven, but for this work that was not a possibility due to time constraints. For the batches where ethanol was still present, the program was run again.



## 6 Conclusion

---

The main goal of this work was to provide a method of controlled oxide and carbon coating of silicon particles from a Free Space Reactor, creating double-core shell particles, and this goal has been partially met. The oxide coating method was simple to perform by a wet chemical route in room temperature. TEOS successfully coated the silicon particles, creating an oxide layer with a thickness of 50-80 nm, as determined by EDS in TEM. This sacrificial oxide layer is thick enough to, when etched away, hold the volume expansion of the majority of silicon, with diameters between 180 and 300 nm, during electrochemical cycling.

The carbon coating was partially controlled, where the results from both TGA and XRD show varying amounts of carbon and crystallization even for samples which were fabricated with the same ratio of Si@SiO<sub>2</sub>-particles to carbon-precursor and underwent the same carbonization treatment. This shows how complex the carbon-coating procedure can become when using agglomerated and polydisperse silicon nanoparticles as the core material. A homogeneous carbon coating was not seen, even in the batches RF01 and RF03 which showed 6.7 and 12.7 wt% carbon by TGA, respectively. The coating appeared to be of a web-like morphology from SEM imaging, interconnecting the Si@SiO<sub>2</sub>-particles into larger secondary particles.

These multiple core-shell particles were not produced in such a quantity that electrochemical cycling was possible, but if the carbon coating is found scalable and controllable in future work, it would serve as an effective route to obtain yolk-shell secondary particles. These particles would then be possible to electrochemically test to see if the spacing between the silicon and carbon improves the lifetime of Li-ion batteries.

Half-cells with reference silicon were however electrochemically tested to serve as a baseline for testing the multiple yolk-shell particles at a later state, and no significant difference in the lifetimes of amorphous and crystalline silicon reference particles was found. The main differences seen in performance seem to be due to variations in the slurry used for electrodes, and possibly due to small differences in loading. The longest lifetime was seen for one half-cell of amorphous Si with a loading of 0.52 mg/cm<sup>2</sup> cycled to a limited capacity of 720 mAh/g at a C-rate of C/10, which achieved just short of 1,000 cycles before failing. Since no significant difference in electrochemical results was seen between amorphous and crystalline silicon, the crystallization of silicon during the pyrolysis is not expected to play a large role in the performance of the final secondary particles.



## 7 Further work

---

This work is a step along the road for producing yolk-shell particles, and in order to move closer to that goal more work should be done to control the coating processes.

- In order to assure a large enough void space for the polydisperse Si to expand during cycling, a thicker layer of oxide may need to be deposited. This will become clear once the etching has been done, and the Si@void@C yolk-shell particles are electrochemically cycled. As the spontaneous homogeneous nucleation of silica spheres occur at high ammonium hydroxide levels (high pH), the oxide coating may need to be done in two steps to produce the needed void space without depleting the TEOS content by producing silica spheres.
- The etching process will remove the Si@SiO<sub>2</sub> coating, and decrease the total weight of the product. For reproducibility in mixing of slurries for electrodes, a minimum amount of 400mg should be made with similar carbon contents. The C-coating process must therefore be found reproducible or upscalable, in order to match this demand.
- Investigate how the polymerization reactions can be sped up by increasing the reaction temperature. Both oxide and RF coating was done at room temperature for this study.
- Keep track of the pH of the solution during both coating steps, as this is an important factor in controlling the coatings.
- Look into the use of the tube furnace, and determine how stable the temperature ramping and holding is. Find a way to determine what the temperature was inside the furnace for the successful (and amorphous) batches were, in comparison to the unsuccessful (and crystalline) batches.



# Bibliography

---

- [1] M. O. Skare. *Coated Silicon Nanoparticles as Anode in Lithium Ion Batteries*. Specialization project, Norwegian University of Science and Technology, 2016.
- [2] B. Dunn, H. Kamath, and J.-M. Tarascon. Electrical Energy Storage for the Grid: A Battery of Choices. *Science*, 334(6058):928–935, 2011. ISSN 0036-8075. doi: 10.1126/science.1212741.
- [3] IEA. International Energy Agency Global EV Outlook, 2016. URL [https://www.iea.org/publications/freepublications/publication/Global\\_{\\_}EV\\_{\\_}Outlook\\_{\\_}2016.pdf](https://www.iea.org/publications/freepublications/publication/Global_{_}EV_{_}Outlook_{_}2016.pdf).
- [4] IEA. International Energy Agency Key World Energy Statistics, 2016. URL <https://www.iea.org/publications/freepublications/publication/keyworld2016.pdf>.
- [5] D. Larcher and J.-M. Tarascon. Towards greener and more sustainable batteries for electrical energy storage. *Nature chemistry*, 7(1):19–29, 2015.
- [6] U. N. DESA. World Population Prospects: 2015 Revision, Key Findings and Tables. Technical report, New York: United Nations Department of Economic and Social Affairs, Population Division, 2015.
- [7] M. Ashuri, Q. He, and L. L. Shaw. Silicon as a potential anode material for Li-ion batteries: where size, geometry and structure matter. *Nanoscale*, 8(1):74–103, 2016.
- [8] D. Wang, M. Gao, H. Pan, J. Wang, and Y. Liu. High performance amorphous-Si@SiO<sub>x</sub>/C composite anode materials for Li-ion batteries derived from ball-milling and in situ carbonization. *Journal of Power Sources*, 256:190–199, 2014.
- [9] N. Liu, H. Wu, M. T. McDowell, Y. Yao, C. Wang, and Y. Cui. A yolk-shell design for stabilized and scalable Li-ion battery alloy anodes. *Nano Letters*, 12(6):3315–3321, 2012. ISSN 15306984. doi: 10.1021/nl3014814.
- [10] H. Wu, L. Hu, M. W. Rowell, D. Kong, J. J. Cha, J. R. McDonough, J. Zhu, Y. Yang, M. D. McGehee, and Y. Cui. Engineering Empty Space between Si Nanoparticles for Lithium Ion Battery Anodes SI. *Nano Letters*, 12(2):904–909, 2012. ISSN 1530-6992. doi: 10.1021/nl102725k.

- [11] N. Liu, K. Huo, M. T. McDowell, J. Zhao, and Y. Cui. Rice husks as a sustainable source of nanostructured silicon for high performance Li-ion battery anodes. *Scientific reports*, 3, 2013.
- [12] C. K. Chan, H. Peng, G. Liu, K. McIlwrath, X. F. Zhang, R. A. Huggins, and Y. Cui. High-performance lithium battery anodes using silicon nanowires. *Nature nanotechnology*, 3(1):31–35, 2008.
- [13] M.-H. Park, M. G. Kim, J. Joo, K. Kim, J. Kim, S. Ahn, Y. Cui, and J. Cho. Silicon nanotube battery anodes. *Nano letters*, 9(11):3844–3847, 2009.
- [14] H. K. Han, C. Loka, Y. M. Yang, J. H. Kim, S. W. Moon, J. S. Cho, and K.-S. Lee. High capacity retention Si/silicide nanocomposite anode materials fabricated by high-energy mechanical milling for lithium-ion rechargeable batteries. *Journal of Power Sources*, 281:293–300, 2015.
- [15] N. Liu, Z. Lu, Ji. Zhao, M. T. McDowell, H.-W. Lee, W. Zhao, and Y. Cui. A pomegranate-inspired nanoscale design for large-volume-change lithium battery anodes. *Nature nanotechnology*, 9(3):187–92, 2014. ISSN 1748-3395. doi: 10.1038/nnano.2014.6.
- [16] C. Scullia. The Commercialization of Lithium Battery Technology. *Proceedings of Battcon*, 2007.
- [17] J.-M. Tarascon and M. Armand. Issues and challenges facing rechargeable lithium batteries. *Nature*, 414(6861):359–67, 2001. ISSN 0028-0836. doi: 10.1038/35104644.
- [18] B. Scrosati. Lithium rocking chair batteries: An old concept? *Journal of The Electrochemical Society*, 139(10):2776–2781, 1992.
- [19] D. Linden and T. B. Reddy. *Handbook of Batteries*. 3rd. McGraw-Hill, 2002.
- [20] V. Etacheri, R. Marom, R. Elazari, G. Salitra, and D. Aurbach. Challenges in the development of advanced Li-ion batteries: a review. *Energy & Environmental Science*, 4:3243–3262, 2011. ISSN 14523981. doi: 10.1039/c1ee01598b.
- [21] D. Aurbach. Review of selected electrode-solution interactions which determine the performance of Li and Li ion batteries. *Journal of Power Sources*, 89(2):206–218, 2000. ISSN 03787753. doi: 10.1016/S0378-7753(00)00431-6.
- [22] B. Scrosati and J. Garche. Lithium batteries: Status, prospects and future. *Journal of Power Sources*, 195:2419–2430, 2010. doi: 10.1016/j.jpowsour.2009.11.048.

- 
- [23] University of Liverpool, Hardwick group. URL <https://www.liverpool.ac.uk/chemistry/research/hardwick-group/research/>.
- [24] S. S. Zhang. A review on electrolyte additives for lithium - ion batteries. *Journal of Power Sources*, 162:1379–1394, 2006. doi: 10.1016/j.jpowsour.2006.07.074.
- [25] D. Aurbach, K. Gamolsky, B. Markovsky, Y. Gofer, M. Schmidt, and U. Heider. On the use of vinylene carbonate ( VC ) as an additive to electrolyte solutions for Li - ion batteries. *Electrochimica Acta*, 47:1423–1439, 2002. doi: 10.1016/S0013-4686(01)00858-1.
- [26] B. Simon and J.-P. Boeue. Rechargeable lithium electrochemical cell, 1997.
- [27] R. McMillan, H. Sleg, Z.X. Shu, and W. Wang. Fluoroethylene carbonate electrolyte and its use in lithium ion batteries with graphite anodes. *Journal of Power Sources*, 81:20–26, 1999. ISSN 03787753. doi: 10.1016/S0378-7753(98)00201-8.
- [28] E. Markevich, G. Salitra, and D. Aurbach. Fluoroethylene Carbonate as an Important Component for the Formation of an Effective Solid Electrolyte Interphase on Anodes and Cathodes for Advanced Li-Ion Batteries. *ACS Energy Letters*, pages 1337–1345, 2017. ISSN 2380-8195. doi: 10.1021/acseenergylett.7b00163.
- [29] W.-J. Zhang. A review of the electrochemical performance of alloy anodes for lithium-ion batteries. *Journal of Power Sources*, 196:13–24, 2010. doi: 10.1016/j.jpowsour.2010.07.020.
- [30] M. Winter and J. O. Besenhard. Electrochemical lithiation of tin and tin-based intermetallics and composites. *Electrochimica Acta*, 45(1):31–50, 1999. ISSN 00134686. doi: 10.1016/S0013-4686(99)00191-7.
- [31] U. Kasavajjula, C. Wang, and A. J. Appleby. Nano- and bulk-silicon-based insertion anodes for lithium-ion secondary cells. *Journal of Power Sources*, 163(2):1003–1039, 2007. ISSN 03787753. doi: 10.1016/j.jpowsour.2006.09.084.
- [32] L. Y. Beaulieu, K. W. Eberman, R. L. Turner, L. J. Krause, and J. R. Dahn. Colossal Reversible Volume Changes in Lithium Alloys. *Electrochemical and Solid-State Letters*, 4:A137–A140, 2001. ISSN 10990062. doi: 10.1149/1.1388178.
- [33] R. Benedek and M. M. Thackeray. Lithium reactions with intermetallic-compound electrodes. In *Journal of Power Sources*, volume 110, pages 406–411, 2002. ISBN 0378-7753. doi: 10.1016/S0378-7753(02)00204-5.

- [34] S.-C. Lai. Solid Lithium-Silicon Electrode. *Brief Communications*, 123(8):1196–1197, 1976.
- [35] C. J. Wen and R. A. Huggins. Chemical diffusion in intermediate phases in the lithium-silicon system. *Journal of Solid State Chemistry*, 37(3):271–278, 1981. ISSN 1095726X. doi: 10.1016/0022-4596(81)90487-4.
- [36] M. N. Obrovac and L. J. Krause. Reversible cycling of crystalline silicon powder. *Journal of The Electrochemical Society*, 154(2):A103—A108, 2007.
- [37] H. Wu and Y. Cui. Designing nanostructured Si anodes for high energy lithium ion batteries. *Nano Today*, 7(5):414–429, 2012.
- [38] J. W. Choi and D. Aurbach. Promise and Reality of Post-Lithium-Ion Batteries with High Energy Densities. *Nature Reviews*, 2016.
- [39] M. N. Obrovac and L. Christensen. Structural Changes in Silicon Anodes during Lithium Insertion/Extraction. *Electrochemical and Solid-State Letters*, 7(5):A93, 2004. ISSN 10990062. doi: 10.1149/1.1652421.
- [40] T. D. Hatchard and J. R. Dahn. In Situ XRD and Electrochemical Study of the Reaction of Lithium with Amorphous Silicon. *Journal of The Electrochemical Society*, 151(6):A838–A842, 2004. doi: 10.1149/1.1739217.
- [41] K. Ogata, E. Salager, C. J. Kerr, A. E. Fraser, C. Ducati, A. J. Morris, S. Hofmann, and C. P. Grey. Revealing lithium-silicide phase transformations in nano-structured silicon-based lithium ion batteries via in situ NMR spectroscopy. *Nature communications*, 5:3217, 2014. ISSN 2041-1723. doi: 10.1038/ncomms4217.
- [42] J. K. Lee. High Performance Li-Ion Battery Anodes Based on Silicon-Graphene Self-Assemblies. In *18th International Meeting on Lithium Batteries (June 19-24, 2016)*. Ecs, 2016.
- [43] F. R. Morral. No Title. *Ark. Kemi, Mineral. Geol.*, 11B(37), 1934.
- [44] M. T. McDowell, S. W. Lee, J. T. Harris, B. A. Korgel, C. Wang, W. D. Nix, and Y. Cui. In situ TEM of two-phase lithiation of amorphous silicon nanospheres. *Nano Letters*, 13(2):758–764, 2013. ISSN 15306984. doi: 10.1021/nl3044508.
- [45] J. H. Ryu, J. W. Kim, Y.-E. Sung, and S. M. Oh. Failure Modes of Silicon Powder Negative Electrode in Lithium Secondary Batteries. *Electrochemical and Solid-State Letters*, 7(10):306–309, 2004. doi: 10.1149/1.1792242.

- 
- [46] Z. Chen, Y. Qin, K. Amine, and Y.-K. Sun. Role of surface coating on cathode materials for lithium-ion batteries. *Journal of Materials Chemistry*, 20(36):7606, 2010. ISSN 0959-9428. doi: 10.1039/c0jm00154f.
- [47] C. Xu, F. Lindgren, B. Philippe, M. Gorgoi, F. Borefors, K. Edström, and T. Gustafsson. Improved performance of the silicon anode for li-ion batteries: Understanding the surface modification mechanism of fluoroethylene carbonate as an effective electrolyte additive. *Chemistry of Materials*, 27(7):2591–2599, 2015. ISSN 15205002. doi: 10.1021/acs.chemmater.5b00339.
- [48] Hi. Nakai, T. Kubota, A. Kita, and A. Kawashima. Investigation of the Solid Electrolyte Interphase Formed by Fluoroethylene Carbonate on Si Electrodes. *Journal of The Electrochemical Society*, 158(7):A798, 2011. ISSN 00134651. doi: 10.1149/1.3589300.
- [49] H. F. Andersen, W. O. Filtvedt, J. P. Mæhlen, T. Mongstad, M. Kirkengen, and A. Holt. Production of Silicon Particles for High-Capacity Anode Material, Yielding Outstanding Production Capacity. *ECS Transactions*, 62(1):97–105, 2014. ISSN 19386737. doi: 10.1149/06201.0097ecst.
- [50] H. Li and H. Zhou. Enhancing the performances of Li-ion batteries by carbon-coating: present and future. *Chem. Commun. Chem. Commun*, 48(48):1201–1217, 2012. doi: 10.1039/c1cc14764a.
- [51] S.-T. Myung, K. Amine, and Y.-K. Sun. Surface modification of cathode materials from nano- to microscale for rechargeable lithium-ion batteries. *Journal of Materials Chemistry*, 20(34):7074, 2010. ISSN 0959-9428. doi: 10.1039/c0jm00508h.
- [52] Z. Chen, Y. Qin, K. Amine, and Y.-K. Sun. Role of surface coating on cathode materials for lithium-ion batteries. *Journal of Materials Chemistry*, 20(36):7606, 2010. ISSN 0959-9428. doi: 10.1039/c0jm00154f.
- [53] N. Wagner, A. M. Svensson, and F. Vullum-Bruer. Effect of carbon content and annealing atmosphere on phase purity and morphology of  $\text{Li}_2\text{MnSiO}_4$  synthesized by a PVA assisted sol-gel method. *Solid State Ionics*, 276:26–32, 2015. ISSN 01672738. doi: 10.1016/j.ssi.2015.03.029.
- [54] A. M. Hashem, A. E. Abdel Ghany, K. Nikolowski, and H. Ehrenberg. Effect of carbon coating process on the structure and electrochemical performance of  $\text{LiNi}_{0.5}\text{Mn}_{0.5}\text{O}_2$  used as cathode in Li-ion batteries. *Ionics*, 16(4):305–310, 2009. ISSN 0947-7047. doi: 10.1007/s11581-009-0403-8.
-

- [55] H. L. Zhang, S. H. Liu, F. Li, S. Bai, C. Liu, J. Tan, and H. M. Cheng. Electrochemical performance of pyrolytic carbon-coated natural graphite spheres. *Carbon*, 44(11): 2212–2218, 2006. ISSN 00086223. doi: 10.1016/j.carbon.2006.02.037.
- [56] M. Yoshio, H. Wang, K. Fukuda, T. Umeno, N. Dimov, and Z. Ogumi. Carbon-Coated Si as a Lithium-Ion Battery Anode Material. *Journal of The Electrochemical Society*, 149(12):A1598, 2002. ISSN 00134651. doi: 10.1149/1.1518988.
- [57] N. Dimov, K. Fukuda, T. Umeno, S. Kuginno, and M. Yoshio. Characterization of carbon-coated silicon: Structural evolution and possible limitations. *Journal of Power Sources*, 114(1):88–95, 2003. ISSN 03787753. doi: 10.1016/S0378-7753(02)00533-5.
- [58] S. H. Ng, J. Wang, D. Wexler, S. Y. Chew, and H. K. Liu. Amorphous carbon-coated silicon nanocomposites: A low-temperature synthesis via spray pyrolysis and their application as high-capacity anodes for lithium-ion batteries. *Journal of Physical Chemistry C*, 111(29):11131–11138, 2007. ISSN 19327447. doi: 10.1021/jp072778d.
- [59] Y. Li, K. Yan, H.-W. Lee, Z. Lu, N. Liu, and Y. Cui. Growth of conformal graphene cages on micrometre-sized silicon particles as stable battery anodes. *Nature Energy*, 1(2):16017, 2016. ISSN 2058-7546. doi: 10.1038/nenergy.2016.17.
- [60] L.-F. Cui, R. Ruffo, C. K. Chan, H. Peng, and Y. Cui. Crystalline-Amorphous Core-Shell Silicon Nanowires for High Capacity and High Current Battery Electrodes. *Nano Letters*, 9(1):491–495, 2009. ISSN 1530-6984. doi: 10.1021/nl8036323.
- [61] N. Liu, K. Huo, M. T. McDowell, J. Zhao, and Y. Cui. Rice husks as a sustainable source of nanostructured silicon for high performance Li-ion battery anodes. *Scientific Reports*, 3(1):1919, dec 2013. ISSN 2045-2322. doi: 10.1038/srep01919. URL <http://www.nature.com/articles/srep01919>.
- [62] T. Hoshino and Y. Nishioka. Etching process of SiO<sub>2</sub> by HF molecules. *The Journal of Chemical Physics*, 111(10), 1999. doi: 10.1063/1.479480.
- [63] L. Pan, H. Wang, D. Gao, S. Chen, L. Tan, and L. Li. Facile synthesis of yolk-shell structured Si-C nanocomposites as anodes for lithium-ion batteries. *Chemical Communications*, 50(44):5878, 2014. ISSN 1359-7345. doi: 10.1039/c4cc01728e.
- [64] B. L. Cushing, V. L. Kolesnichenko, and C. J. O'Connor. Recent advances in the liquid-phase syntheses of inorganic nanoparticles. *Chemical Reviews*, 104(9):3893–3946, 2004. ISSN 00092665. doi: 10.1021/cr030027b.

- 
- [65] W. Stöber, A. Fink, and E. Bohn. Controlled growth of monodisperse silica spheres in the micron size range. *Journal of colloid and interface science*, 26(1):62–69, 1968.
- [66] Y. Gan, Y. Yin, N. Li, Q. Zhang, J. Liu, J. Joo, and A. Lee. Sol–gel coating of inorganic nanostructures with resorcinol–formaldehyde resin. *Chem. Commun. Chem. Commun*, 49(49):5093–5238, 2013. ISSN 1359-7345.
- [67] J. Liu, S. Z. Qiao, H. Liu, J. Chen, A. Orpe, D. Zhao, and G. Q. (Max) Lu. Extension of The Stöber Method to the Preparation of Monodisperse Resorcinol–Formaldehyde Resin Polymer and Carbon Spheres. *Angewandte Chemie International Edition*, 50(26):5947–5951, 2011. ISSN 1521-3773. doi: 10.1002/anie.201102011.
- [68] S. A. Al-Muhtaseb and J. A. Ritter. Preparation and properties of resorcinol-formaldehyde organic and carbon gels. *Advanced Materials*, 15(2):101–114, 2003. ISSN 09359648. doi: 10.1002/adma.200390020.
- [69] A. M. Elkhatat and S. A. Al-Muhtaseb. Advances in tailoring resorcinol-formaldehyde organic and carbon gels, 2011. ISSN 09359648.
- [70] M. Kosmulski. Chemical Properties of Material Surfaces. *Chemical Properties of Material Surfaces*, pages Marcel Dekker Inc., New York, NY, 2001. ISSN 09552219. doi: 10.1201/9780585418049.
- [71] Organic and Carbon Aerogels. URL [www.aerogel.org/?p=71](http://www.aerogel.org/?p=71).
- [72] I. Chorkendorff and J. W. Niemantsverdriet. *Concepts of Modern Catalysis and Kinetics*. Wiley-VCH, 2 edition, 2007.
- [73] K. Nogi, M. Naito, and T. Yokoyama. *Nanoparticle Technology Handbook*. Elsevier, 2012.
- [74] R. Shaw. Dynamic Light Scattering Training: Achieving Reliable Nano Particle Sizing. Technical report, 2014. URL <http://149.171.168.221/partcat/wp-content/uploads/Malvern-Zetasizer-LS.pdf>.
- [75] A. J. Bard, G. Inzelt, and F. Scholz. *Electrochemical dictionary*. Springer Verlag, 2012. ISBN 978-3-642-29550-8. doi: 10.1007/978-3-642-29551-5.
- [76] Y. X. Lin, Z. Liu, K. Leung, L. Q. Chen, P. Lu, and Y. Qi. Connecting the irreversible capacity loss in Li-ion batteries with the electronic insulating properties of solid electrolyte interphase (SEI) components. *Journal of Power Sources*, 309:221–230, 2016. ISSN 03787753. doi: 10.1016/j.jpowsour.2016.01.078.

- [77] F. A. Soto, Y. Ma, J. M. Martinez De La Hoz, J. M. Seminario, and P. B. Balbuena. Formation and Growth Mechanisms of Solid-Electrolyte Interphase Layers in Rechargeable Batteries. *Chemistry of Materials*, 27(23):7990–8000, 2015. ISSN 15205002. doi: 10.1021/acs.chemmater.5b03358.
- [78] J. B. Goodenough and K. S. Park. The Li-ion rechargeable battery: A perspective, 2013. ISSN 00027863. URL <http://pubs.acs.org/doi/pdf/10.1021/ja3091438>.
- [79] J. E. B. Randles. Kinetics of rapid electrode reactions. *Discussions of the Faraday Society*, 1(0):11, 1947. ISSN 0366-9033. doi: 10.1039/df9470100011.
- [80] M. S. Wang, L. Z. Fan, M. Huang, J. Li, and X. Qu. Conversion of diatomite to porous Si/C composites as promising anode materials for lithium-ion batteries. *Journal of Power Sources*, 219:29–35, 2012. ISSN 03787753. doi: 10.1016/j.jpowsour.2012.06.102.
- [81] D. Wang, M. Gao, H. Pan, J. Wang, and Y. Liu. High performance amorphous-Si@SiOx/C composite anode materials for Li-ion batteries derived from ball-milling and in situ carbonization. *Journal of Power Sources*, 256:190–199, 2014. ISSN 03787753. doi: 10.1016/j.jpowsour.2013.12.128.
- [82] X. H. Liu, L. Zhong, S. Huang, S. X. Mao, T. Zhu, and J. Y. Huang. Size-dependent fracture of silicon nanoparticles during lithiation. *ACS Nano*, 6(2):1522–1531, 2012. ISSN 19360851. doi: 10.1021/nn204476h.
- [83] F. Farmakis, C. Elmasides, P. Fanz, M. Hagen, and N. Georgoulas. High energy density amorphous silicon anodes for lithium ion batteries deposited by DC sputtering. *Journal of Power Sources*, 293:301–305, 2015. ISSN 03787753. doi: 10.1016/j.jpowsour.2015.05.083.
- [84] Y. Li, K. Yan, H.-W. Lee, Z. Lu, N. Liu, and Y. Cui. Supplementary info - Growth of conformal graphene cages on micrometre-sized silicon particles as stable battery anodes. *Nature Energy*, 1(2), 2016. doi: 10.1038/NENERGY.2015.29.
- [85] V. M. Masalov, N. S. Sukhinina, E. A. Kudrenko, and G. A. Emelchenko. Mechanism of formation and nanostructure of Stöber silica particles. *Nanotechnology*, 22(27):275718, 2011. ISSN 0957-4484. doi: 10.1088/0957-4484/22/27/275718.
- [86] H. Zhou, M. A. Einarsrud, and F. Vullum-Bruer. High capacity nanostructured Li<sub>2</sub>FexSiO<sub>4</sub>/C with Fe hyperstoichiometry for Li-ion batteries. *Journal of Power Sources*, 235:234–242, 2013. ISSN 03787753. doi: 10.1016/j.jpowsour.2013.02.023.

- 
- [87] L. Su, Z. Zhou, and M. Ren. Core double-shell Si@SiO<sub>2</sub>@C nanocomposites as anode materials for Li-ion batteries. *Chemical Communications*, 46(15):2590, 2010. ISSN 1359-7345. doi: 10.1039/b925696b.
- [88] W.-S. Chang, C.-M. Park, J.-H. Kim, Y.-U. Kim, G. Jeong, and H.-J. Sohn. Quartz (SiO<sub>2</sub>): a new energy storage anode material for Li-ion batteries. *Energy & Environmental Science*, 5(5):6895, 2012. ISSN 1754-5692. doi: 10.1039/c2ee00003b.
- [89] J. Sourice, A. Bordes, A. Boulineau, J. P. Alper, S. Franger, A. Quinsac, A. Habert, Y. Leconte, E. De Vito, W. Porcher, C. Reynaud, N. Herlin-Boime, and C. Haon. Core-shell amorphous silicon-carbon nanoparticles for high performance anodes in lithium ion batteries. *Journal of Power Sources*, 328(October):527–535, 2016. ISSN 03787753. doi: 10.1016/j.jpowsour.2016.08.057.
- [90] X. Fang, S. Liu, J. Zang, C. Xu, M.-S. Zheng, Q.-F. Dong, D. Sun, and N. Zheng. Precisely controlled resorcinol–formaldehyde resin coating for fabricating core–shell, hollow, and yolk–shell carbon nanostructures. *Nanoscale*, 5(15):6908, 2013. ISSN 2040-3364. doi: 10.1039/c3nr01723k.
- [91] Raj B. Durairaj. *Resorcinol : chemistry, technology, and applications*. Springer, 2005. ISBN 3540280901.
- [92] C. Liang and S. Dai. Synthesis of mesoporous carbon materials via enhanced hydrogen-bonding interaction. *Journal of the American Chemical Society*, 128(16): 5316–5317, 2006. ISSN 00027863. doi: 10.1021/ja060242k.
- [93] J. Kuhn, R. Brandt, H. Mehling, R. Petričević, and J. Fricke. In situ infrared observation of the pyrolysis process of carbon aerogels. *Journal of Non-Crystalline Solids*, 225:58–63, 1998. ISSN 00223093. doi: 10.1016/S0022-3093(98)00009-X.
- [94] E. J. Zanto, S. Al-muhtaseb, and J. A. Ritter. Sol - Gel-Derived Carbon aerogels and xerogels: Design of experiments approach to materials synthesis. *Ing. Eng. Chem. Res.*, 41:3151–3162, 2002. ISSN 0888-5885. doi: 10.1021/ie020048g.
- [95] S. Q. Zhang, J. Wang, J. Shen, Z. S. Deng, Z. Q. Lai, B. Zhou, S. M. Attia, and L. Y. Chen. Investigation of the adsorption character of carbon aerogels. *Nanostructured Materials*, 11(3):375–381, 1999. ISSN 09659773. doi: 10.1016/S0965-9773(99)00054-9.
- [96] C. Lin. Development of Carbon-Metal Oxide Supercapacitors from Sol-Gel Derived Carbon-Ruthenium Xerogels. *Journal of The Electrochemical Society*, 146(9):3155, 1999. ISSN 00134651. doi: 10.1149/1.1392448.



# A Oxide and carbon coating process

---

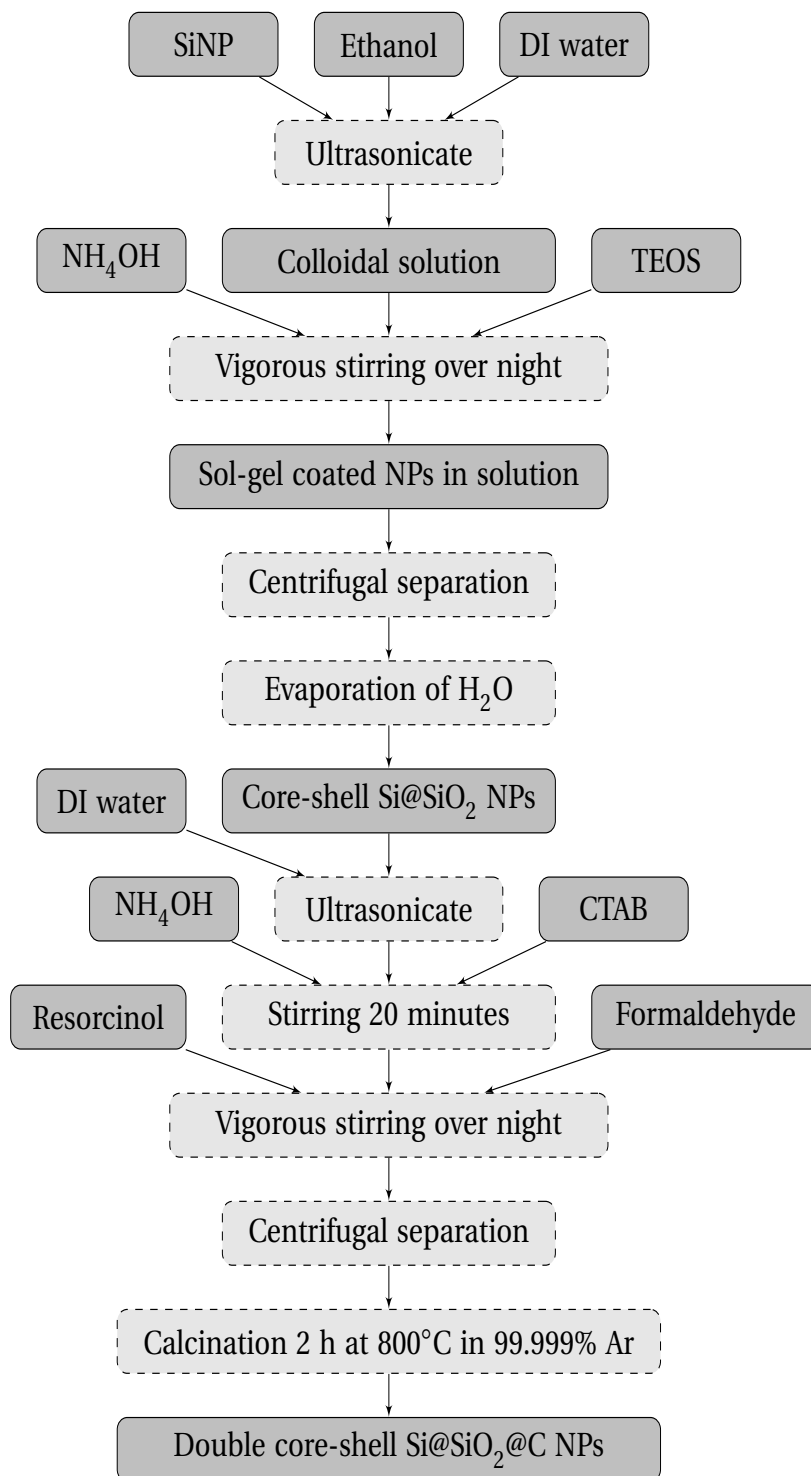


**Figure A.1:** Flow chart of coating process



# B Slurry preparation and tape casting of electrode

---

The slurry should be composed of 60% active material, 15% binder, 15% carbon black and 10% graphite. Slurries with values as close to this composition as possible were made.

**Table B.1:** Recipe for slurry

Material	Slurry Ideal Composition [%]	1	2a	2b	3
		a-Si ref	c-Si ref	c-Si ref	Si@SiO <sub>2</sub>
		Actual composition [%]			
Active material	60	52.2	52.2	52.1	51.8
C, graphite	10	9.1	9.1	8.6	8.7
C, black	15	13.0	13.2	13.0	13.1
Binder, CMC	15	12.9	13.0	13.4	13.4
Solvent	4:1 dry weight	12.8	12.5	12.9	13.0

## Procedure:

1. The buffer and CMC binder were weighed and transferred to a container for mixing in a planetary mixer.
2. When completely mixed, the other dry components (Si or Si@SiO<sub>2</sub>, graphite and carbon black) were weighed and placed in the container.
3. This slurry was placed in the planetary mixer for creation of a viscous slurry.
4. The slurry was spread onto a dendritic copper foil sheet, and evenly distributed as a one half-inch or one inch thick electrode following the tape casting process.
5. The electrode sheet was dried at room temperature over night.
6. The electrode was dried in a vacuum oven at 120°C for three hours.
7. Electrode disks of Ø15 were cut using a Hohsen electrode punch, and the loading was recorded as grams of active material per cm<sup>2</sup>.



# C Electrochemical cycling programs

---

## C.1 Galvanostatic charge-discharge at unlimited capacity

1. Open circuit voltage (OCV) 6 h rest
2. IR measurement 1
3. Two formation cycles:
  - (a) Charge at C/20 with cut-off at 50 mV
  - (b) IR measurement 2
  - (c) OCV and rest
  - (d) Discharge at C/20 with cut-off at 1 V
  - (e) IR measurement 3
  - (f) OCV and rest
4. Loop at C/5 for 200 charge/discharge cycles
  - (a) Charge at C/5 with cut-off at 50 mV
  - (b) IR measurement 4
  - (c) OCV and rest
  - (d) Discharge at C/5 with cut-off at 1 V
  - (e) IR measurement 5
  - (f) OCV and rest

## C.2 Galvanostatic charge-discharge at limited capacity

1. OCV 6h rest
2. IR measurement 1
3. Two formation cycles:
  - (a) Charge at C/20 with cut-off at 1,200 mAh/g
  - (b) IR measurement 2
  - (c) OCV and rest
  - (d) Discharge at C/20 with cut-off at 1 V
  - (e) IR measurement 3

- (f) OCV and rest
- 4. Loop at C/5 for 1,000 charge/discharge cycles
  - (a) Charge at C/5 with cut-off at 1,200 mAh/g
  - (b) IR measurement 4
  - (c) OCV and rest
  - (d) Discharge at C/5 with cut-off at 1 V
  - (e) IR measurement 5
  - (f) OCV and rest

### **C.3 Electrochemical Impedance Spectroscopy**

- 1. OCV 6 h rest
- 2. Two formation cycles:
  - (a) Charge at C/20 with cut-off at 48 h or 50 mV
  - (b) OCV 1h rest
  - (c) Discharge at C/20 with cut-off at 48 h or 1 V
  - (d) OCV 1h rest
- 3. Charge at C/5 for 2.5 h, obtaining an expected 50% SOC
- 4. OCV 1 h rest
- 5. GEIS measurement at 50% SOC
  - (a) Loop four times. Frequency range of 10 mHz - 100 kHz and at 100  $\mu$ A. 1 m rest in between each loop.
- 6. Charge at C/5 for 2.5 hours, obtaining an expected 100% SOC
- 7. OCV 1h rest
- 8. GEIS measurement at 100% SOC
  - (a) Loop four times. Frequency range of 10 mHz - 100 kHz and at 100  $\mu$ A. 1 m rest in between each loop.